

ABSTRACT

SORRELL, EMMA Pattern Detection and Mechanical Modeling of Cylindrical Packing as Applied to the Notochord (under the direction of Dr. Sharon R. Lubkin).

The notochord, which is a biological structure that develops into the nucleus pulposus of intervertebral discs and is the defining feature of chordates, has inner vacuolated cells surrounded by a thin layer of epithelial cells that form a constraining sheath. These inner cells form configurations reminiscent of the phyllotactic patterns found in cylindrical foams, and the patterns are influenced by the physical properties of the sheath. We have created a novel algorithm to quantify the often irregular patterns formed by these vacuolated cells as they arrange in the notochord during morphogenesis, and the application of this algorithm to zebrafish notochords reveals commonalities between notochord packing and the packing in an inert analog system, which provides justification for a mechanical model of the notochord. We present three new mechanical models of foams in tubes of previously unstudied varying cross sections and varying physical properties, including a model for a flexible tube, and these models are united by two key ratios that interact with cross-sectional tube eccentricity. We analyze the lowest-order regular patterns in these models and identify a bifurcation to a previously unidentified packing pattern.

© Copyright 2019 by Emma Sorrell

All Rights Reserved

Mechanical Modeling of Cylindrical Packing and Pattern Detection as Applied to the Notochord

by
Emma L. Sorrell

A dissertation submitted to the Graduate Faculty of
North Carolina State University
in partial fulfillment of the
requirements for the degree of
Doctor of Philosophy

Applied Mathematics

Raleigh, North Carolina
2019

APPROVED BY:

Sharon R. Lubkin
Committee Chair

Ralph Smith

Radmila Sazdanovic

Nanette Nascone-Yoder

DEDICATION

To Dr. Dominic Klyve, whom I hold completely responsible for getting me into this entire mess in the first place.

BIOGRAPHY

Emma was born in Wisconsin just in time to be a 90's baby. She grew up swimming, reading, and riding bikes with her dad, and painting and drawing with her mom. She loved school far more than was reasonable, which explains a lot. Emma enjoyed singing and dancing in musicals, but she hated being in the spotlight. This combination proved to be the end of her chances for a Broadway career, and she turned to mathematics for solace. When Emma got stuck outdoors in the great Snowpocalypse of 2011 while applying to graduate schools, she decided she was done with living up north, thank you very much, and fled south to North Carolina State University. Emma now lives with her three cats, two dogs, and one wonderful fiancé in a house with a totally sick arcade.

ACKNOWLEDGMENTS

I would like to express my deepest appreciation for my advisor, Dr. Sharon R. Lubkin, for her wisdom and infinite patience. I would not be the mathematician, writer, or scientist (or gardener, or cook) that I am today without her guidance. I would also like to thank the rest of my committee, Dr. Ralph Smith, Dr. Radmila Sazdanovic, and Dr. Nanette Nascone-Yoder for their time and invaluable expertise.

I would also like to extend my deepest gratitude to Dr. Michel Bagnat at Duke for the fantastic interdisciplinary research opportunity, and for support from the HHMI Faculty Scholar Award. I am exceedingly grateful for the opportunity to collaborate on an excellent paper.

The completion of my dissertation would also not have been possible without the aid of the Doctoral Dissertation Completion Grant. The support of this group, especially Scott Lindauer, kept me moving forward where I would otherwise have stalled.

I cannot begin to express my thanks to Ariel Nikas, without whom I would never have survived the research and writing process. I would also like to thank Meredith Harris, Mary Lewis, Jamie Nosbisch, Marcella Noorman, and Anne Pioppo for their outpouring of encouragement and cute puppy pictures.

I'm deeply indebted to my fiancé, Anthony Thomas, for his unyielding love and support through what I'm sure was an incredibly difficult process for him as well as me. Thank you also to my parents, Diane and Bert Sorrell - I couldn't have gotten here without their cheerleading and unwavering belief in my abilities.

Special thanks to my sweet tripod cat Benedictine Cucumberpatch. I just want to be able to give her the life she deserves.

TABLE OF CONTENTS

LIST OF TABLES	vii
LIST OF FIGURES	viii
Chapter 1: Introduction	1
1.1 Brief Review of Recent Progress in the Study of Contained Foams	2
1.2 Foam Modeling as a Basis for Notochord Pattern Identification	5
Chapter 2: Two Algorithms for Biological Pattern Identification in Cylinders	9
2.1 Ordered Patterns in Foams	9
2.2 Packing of Irregular Bodies	12
2.3 Hopscotch Patterns	15
2.4 Two Algorithms for Pattern Identification	16
2.4.1 Radial Algorithm	17
2.4.1 Projection Algorithm	18
2.5 Periodicity Sorting and Pattern Classification	20
2.6 Algorithm Comparison	20
Chapter 3: Packing in Elliptical Cylinders	23
3.1 Continuous Models	24
3.1.1 Rigid Sheath Model	26
3.1.2 Semi-Flexible Sheath Model	30
3.1.3 Flexible Sheath Model	32
3.2 Discretization	33
3.2.1 Rigid Sheath Model	34
3.2.2 Semi-Flexible Sheath and Flexible Sheath Models	39
3.3 Test Problems	40
3.3.1 Two-Dimensional Analogue Problem	40
3.3.2 Two Bubbles	44
3.4 Model Implementation in Surface Evolver	49
3.4.1 Initial Geometry	50
3.4.2 Boundary Conditions	51
3.4.3 Iteration	52
3.4.4 Convergence	53
3.5 Results	53
3.5.1 Rigid Sheath	53
3.5.2 Semi-flexible Sheath	57
3.5.3 Fully Flexible Sheath	59
Chapter 4: Conclusion	65
4.1 Discussion	65
4.2 Future Work	67
References	69

APPENDICES	74
Appendix A: Example Surface Evolver File.....	75
Appendix B: Fit Analysis.....	77
Appendix C: Table of Symbols.....	78
Appendix D: MATLAB Orthogonality Algorithm	79
Appendix E: Tissue self-organization underlies morphogenesis of the notochord.....	81

LIST OF TABLES

Table 5.1	Summary of fit analysis for each quadratic $p_e\lambda$	69
Table 5.2	Common parameters and variables used in the three foam models.	72

LIST OF FIGURES

Figure 1.1	A) Depiction of a zebrafish notochord. The inner cells are largely vacuole, and are much larger than the outer sheath cells [9]. B) Dorsal (top), lateral (bottom) and transverse (right) views of a section of wild type (WT) zebrafish notochord with inner cells. The cells are arranged in a pattern typical for the WT strain. Confocal microscopy in B courtesy of Dr. Michel Bagnat, Duke University.....	1
Figure 1.2	A) Section of notochord from a WT zebrafish. Confocal microscopy courtesy of Dr. Michel Bagnat, Duke University. B) Section of soap foam in a tube from [25]. The patterns formed by the cells in A and foam in B are visually similar, although the notochord's cells are polydisperse.	2
Figure 1.3	Patterns bamboo, staircase, chiral, and hopscotch as they appear in foams [12] (left) and sketched to show structure (right). The vector notation is defined in Chapter 2.....	4
Figure 1.4	Tube containing a foam in transition from wet to dry. Note that wet foam appears to have space between the bubbles because wet foams possess a significant amount of liquid volume. Foam image from [12].....	5
Figure 1.5:	A) Eccentricity of flexible tubes containing gel beads in the staircase pattern compared to tubes containing the first chiral pattern. Tubes containing the staircase pattern consistently presented with higher eccentricity than those with first chiral ($n = 6$ tubes, $*p < 0.0001$, Welch's t-test) [22]. B) Rigid tubes with eccentricity containing gel beads. The occurrence of staircase pattern varies with λ , but it never occupies more than half the tube. C) Rigid tube of eccentricity containing gel beads. The staircase dominates the existence of other patterns for all λ tested.....	7
Figure 2.1:	Example of a structure of two-dimensional hexagonal cells, the result of “unwrapping” the surface of a cylinder with this pattern. The surface of the cylinder is separated at the green cells, so they are included on either side to facilitate the observation of neighbors. Examining the 7 th cell, for example, we see its neighbors have indices 8, 10, and 11. Then $k = 11 - 7 = 4$, $l = 10 - 7 = 3$, and $m = 8 - 7 = 1$, so this structure is in the (4, 3, 1) pattern; note that $k = l + m$ as expected.	10
Figure 2.2:	Dorsal and lateral view from a three dimensional rendering of a WT zebrafish notochord [23] carried out with ImarisCell [5]. The existence of nonzero curvature of the notochord is particularly clear in the lateral view.....	12

Figure 2.3:	Heat maps of notochord cell centroid positions in transverse view using four fish from each strain; NICD is a mutant strain with the lowest density of cells per unit length, and SuHDN is a mutant strain with the highest density of cells per unit length. All cross sections are oriented with the dorsal (D) side on the top and ventral (V) side on the bottom, which are aligned with our \hat{Z} axis; the right (R) and left (L) are relative to the orientation of fish and are aligned with the \hat{Y} axis [22].	14
Figure 2.4:	Sketch of several cells in the A) regular and B) irregular hopscotch patterns. In foams, regular hopscotch alternates between horizontal pairs of bubbles and a single bubble that spans the entire diameter of the tube. Irregular hopscotch is characterized by having either one or two bubbles stacked irregularly between the horizontal pairs of bubbles.	16
Figure 2.5:	The four types of cell periodicities used for the projection algorithm.	18
Figure 2.6	Sorting algorithm used for categorizing cells into a pattern array P_n based on periodicity. The order in which the element T_j is checked for periodicity is required to correctly identify all patterns. Connections between cells are flagged to mark potential transitions between patterns.	21
Figure 3.1	Example of ellipses with different eccentricities; A) has eccentricity $e = 0.9$ and B) has eccentricity $e = 0$.	23
Figure 3.2:	Variations in λ cause changes in pattern in foam experiments. The solid line represents pattern transitions as λ is increased, and the dashed line represents pattern changes as λ is decreased. Patterns above the grey line have not been observed in the zebrafish notochord. The difference in pattern transition points indicates a range of λ for which a pattern is stable. The variable $ V $ is a numerical characterization of different patterns, and the computation of this value for different λ values is discussed in Section 2.1. Original figure from [12], annotations added.	25
Figure 3.3:	Sketch of the cross section of the configuration used for the rigid model. Two cells are shown, one in red and one in blue, with the sheath drawn in black. The surface being minimized is the one formed by cells in contact with each other, not the cell surface in contact with the sheath. The sheath is rigid and therefore is ignored in energy minimization.	27
Figure 3.4:	Sketch of the cross section of the configuration used for the semi-flexible model. Two cells are shown, one in red and one in blue, with the sheath	

	represented in black. We are minimizing the surfaces that are formed by cell-cell contact combined with the surfaces formed by cell contact with the sheath.	30
Figure 3.5:	Sketch of the cross section used for the fully flexible model. Both sheath-cell and cell-cell surfaces contribute to energy and are being jointly minimized, but they are no longer constrained to have a surface on a bounding ellipse.....	32
Figure 3.6:	A) An arbitrary cell, B) arbitrary face F_1 , C) F_1 discretized into facets, D) discretization into individual facets, and E) facet f_1 with vertices v_0 , v_1 , and v_2 , connected by edges s_0 , s_1 , and s_2	33
Figure 3.7:	Difference in visible curvature and curvature ratio with A) eccentricity = 0.9 and B) eccentricity = 0.....	35
Figure 3.8:	An ellipse is initially represented as six vertices connected by edges. The area between the approximation and actual ellipse is in blue. A) The mesh is refined, doubling the number of vertices used, but no position adjustments are made. B) The vertices are shifted by increasing k , but no new vertices are added. C) The mesh is refined and the vertices are shifted.	37
Figure 3.9:	The curved volume, in red, is discretized into the black surface. The vector \vec{s} , in black, is projected onto the blue plane, which is tangent to the red surface at the tail of \vec{s} , creating the blue vector \vec{q}_i	38
Figure 3.10:	Two-dimensional potential fundamental regions in A) bamboo and B) staircase, which are each composed of two cells. The green edges are the ones that contribute to interfacial tension. The bottom edges are intentionally excluded to prevent counting edges twice when the pattern is repeated.	40
Figure 3.11:	Initial fundamental region that is repeated infinitely in either direction. The red and blue each represent one cell.	43
Figure 3.12:	Nondimensional energy per unit volume in the bamboo configuration is shown in red, and the nondimensional energy per unit volume in the staircase configuration is shown in blue. The λ value where the computed staircase energy becomes lower than the projected bamboo configuration energy is approximately 1.17.	44
Figure 3.13:	Surface Evolver initial geometry used to simulate the mechanics of two bubbles of equal volume.	45

Figure 3.14:	A) Two bubbles of equal volume and surface tension, B) arbitrary intersection of the surfaces of two bubbles and the plane perpendicular to all bubble surfaces.	46
Figure 3.15:	Simulated nondimensional energy, shown in black, is measured as a function of mesh fineness, as determined by number of facets used in the mesh; the cell volume is set to $v = 1$. After approximately 10,000 facets, the energy has converged to within 0.1 % of the analytical solution to this problem, which is $\sqrt[3]{27\pi v^2}$ and is indicated by the grey dashed line.	48
Figure 3.16:	A) Initial fundamental region in three dimensions, B) Two full cells represented by the fundamental region, C) the fundamental region cross section; the shared edge of the triangles is also the minor axis of the bounding ellipse.	50
Figure 3.17:	Simulated energy of a cell in bamboo pattern for the rigid sheath model. The simulated energy agreed with the analytical solution for the system. Like the analytical solution, the simulated nondimensional energy is independent of eccentricity and varies solely with λ	55
Figure 3.18:	Minimized energy for staircase simulations (dashed lines), by λ and e , compared with analytical energy for bamboo (grey solid line). The simulations with eccentricity of relevance to the notochord are colored in teal. There is overlap between where staircase pattern is observed and where bamboo pattern is optimal. Nondimensional energy for cells in the staircase pattern decreases for fixed λ when eccentricity is increased, and this relationship between eccentricity and energy is nonlinear as particularly evidenced by the spacing between $e = 0.6$ through $e = 0.9$	56
Figure 3.19:	Circles represent λ_{BS} values for varying eccentricity. There is a strong relationship between tube eccentricity and the λ value at which the minimal energy pattern changes from bamboo to staircase.	57
Figure 3.20:	Example of simulated bamboo pattern (top) and staircase pattern (bottom). The Γ values are the same for both, but the different λ values result in different patterns..	58
Figure 3.21:	A) Effect of λ on eccentricity $e(\lambda, \Gamma)$ for different Γ values in the semi-flexible sheath model. For all values Γ values tested, higher eccentricity is associated with higher λ and lower eccentricity is associated with lower λ . B) Effect of Γ on eccentricity $e(\lambda, \Gamma)$ for different λ values in the semi-flexible sheath model.	

	For higher λ , decreasing Γ decreases the difference between high and low eccentricity. For $\lambda = 1$, varying Γ causes eccentricity to jump from high to low (as a result of pattern change).	58
Figure 3.22:	Optimal packing in the fundamental region for different Γ with $\lambda = 1.12$. Increasing Γ causes the curvature of the cells to decrease.....	59
Figure 3.23:	Generalization of 3.14, with surface tensions allowed to be unequal. The solution is an extension of Plateau's laws, the Young-Dupré equation [7].....	60
Figure 3.24:	A) Relationship between λ and eccentricity \tilde{e} for different Γ values. Increasing λ generally causes an increase in \tilde{e} , but this is especially noticeable once $\tilde{e} > 0.1$. B) The relationship between Γ and eccentricity \tilde{e} for different λ values. Compared to the results of the semi-flexible sheath, there are more values of λ that exhibit high \tilde{e} for low Γ , and they do not follow the curve formed by the simulations of the lowest λ values.....	61
Figure 3.25:	Optimal packing in the fundamental region for combinations of λ and Γ . Increasing Γ causes the curvature of the cells to decrease, while varying λ causes the pattern of the cells to change.	62
Figure 3.26:	Relationship between eccentricity, pattern, λ , and Γ . Bamboo consistently has eccentricity near zero, and both serpentine and staircase present with high eccentricity. There is an additional bifurcation in patterns associated with $\Gamma < 0.6$ and $1.17 < \lambda < 1.33$ that does not appear for the rigid or semi-flexible models, which do not exhibit the serpentine pattern.	63

Chapter 1

Introduction

The notochord is a tube of soft tissue that helps elongate the chordate embryo and in most chordates, it is a precursor to the spine. The notochord provides the developing embryo with a structural framework, and in vertebrates controls the signaling that influences left-right differentiation and arterial/venous sorting of blood vessels. In most chordates, the cells in the notochord are precursors of the center (nucleus pulposus) of the intervertebral disks in the spine [32]. Incorrect formation of the notochord is associated with the development of scoliosis [9].

In the context of this dissertation, when we refer to morphogenesis of the notochord, we specifically mean the effect that the packing of the interior cells constrained by a sheath during early embryonic development has on the overall geometric properties of the notochord. As illustrated in Figure 1.1, the sheath of the notochord is composed of a layer of squamous epithelial cells, while the interior cells are larger and vacuolated [10]. The specific formation into which the interior cells arrange themselves directly contributes to the strength and flexibility of the notochord, and thus the correct formation of the spine [10, 23].

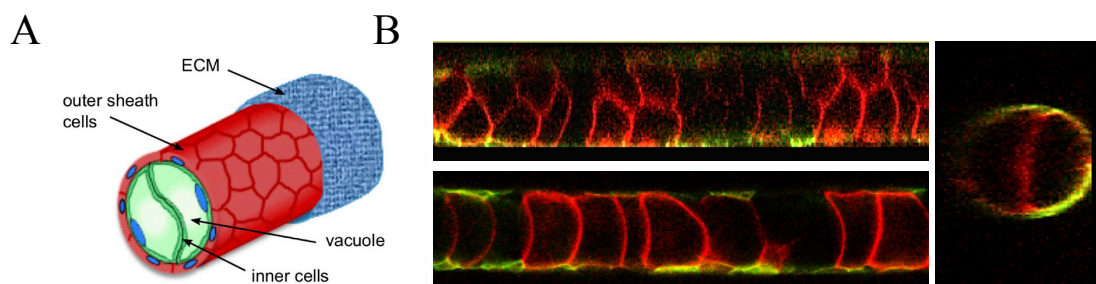


Figure 1.1: A) Depiction of a zebrafish notochord. The inner cells are largely vacuole, and are much larger than the outer sheath cells. From [9]. B) Dorsal (top), lateral (bottom) and transverse (right) views of a section of wild type (WT) zebrafish notochord with inner cells. The cells are arranged in a pattern typical for the WT strain. Confocal microscopy in B courtesy of Dr. Michel Bagnat, Duke University.

The notochord has proven extremely important throughout vertebrate and chordate evolutionary history and has been present in the fossil record as far back as the Early Cambrian [31], and its mechanical properties have been well-studied [15, 22]. However, little is known about the mechanical properties of the notochord cells themselves. Because the interior cells of the notochord are largely vacuole, the notochord has been speculated to have mechanics like that of a soap foam contained in a tube [23]. Figure 1.2 illustrates the similarity between internal notochord cell geometry (Figure 1.2A) and foam geometry (Figure 1.2B).

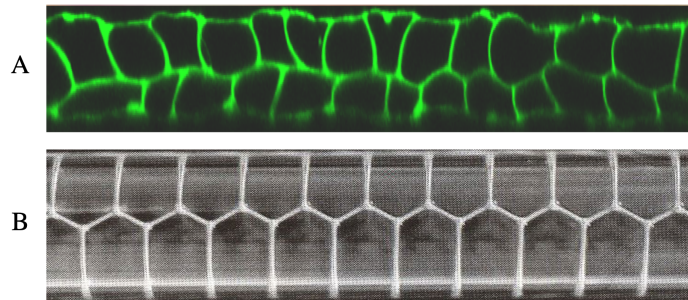


Figure 1.2: A) Section of notochord from a WT zebrafish. Confocal microscopy courtesy of Dr. Michel Bagnat, Duke University. B) Section of soap foam in a tube from [25]. The patterns formed by the cells in A and foam in B are visually similar, although the notochord's cells are polydisperse.

1.1. Brief Review of Recent Progress in the Study of Contained Foams

The basic physics of contained, monodisperse foams, meaning those composed of bubbles of equal size, has been well-established [36]. Monodisperse foams packed in a tube can form ordered patterns, where bubbles group together to create a pattern that is repeated throughout the entire container. This ordered packing allows a small number of bubbles, enough to form the repeated pattern, to be studied in lieu of the entire container.

There are many experiments on foams packed in a regular circular cylinder [12, 13, 25, 26, 29, 38]. The results from these experiments indicate that there is a strong relationship between the ratio of cylinder diameter D to the diameter d of a sphere with the same volume as a

bubble, defined as $\lambda = D/d$, and the pattern that is formed. Furthermore, as λ is varied experimentally, there are sharp transitions between patterns, indicating bifurcations. This makes the role of λ both interesting and valuable, as it is nondimensional and can easily be used to compare experimental results with simulations and controls greatly, if not entirely, the equilibrium pattern of a confined foam. The phenomenon of sharp transitions has been examined in detail for regular cylinders, as in [13, 25, 26, 29], and we will briefly review that work here.

The modern study of foams began in 1992 with the letter and subsequent 1995 paper by Hutzler, Pittet, and Weaire in *Forma* [26, 38]. These works laid the foundation for the current phyllotactic approach to foam packing in tubes by making the observation that soap foams in cylinders form patterns very like phyllotactic patterns common in plant growth [33]. The lowest order patterns are shown in Figure 1.3. In particular, Hutzler, Pittet, and Weaire introduced the use of the ratio of tube diameter to bubble diameter, denoted λ , and they related this dimensionless parameter to traditional phyllotactic notation and showed that λ drives the formation and transitions of structures [26]. They further gave the two least complex patterns names - bamboo and staircase - in addition to their numeric phyllotactic designations - (1, 1, 0) and (2, 1, 1), respectively - and these names are still in common use. The name “hopscotch” given to the the pattern numerically designated (2, 2, 0) was coined in [23].

In a later paper, Pittet et al. [25] analyzed the transitions between patterns and concluded that there were rules for which patterns could transition to which others, based on elementary topological transformations. Hutzler et al. [13] expanded on these conclusions and experimented with moving foam transitions, and they discovered the so-called twist boundary in the staircase

foam pattern, in which a seemingly stable configuration spontaneously rotates 180° without changing topology.

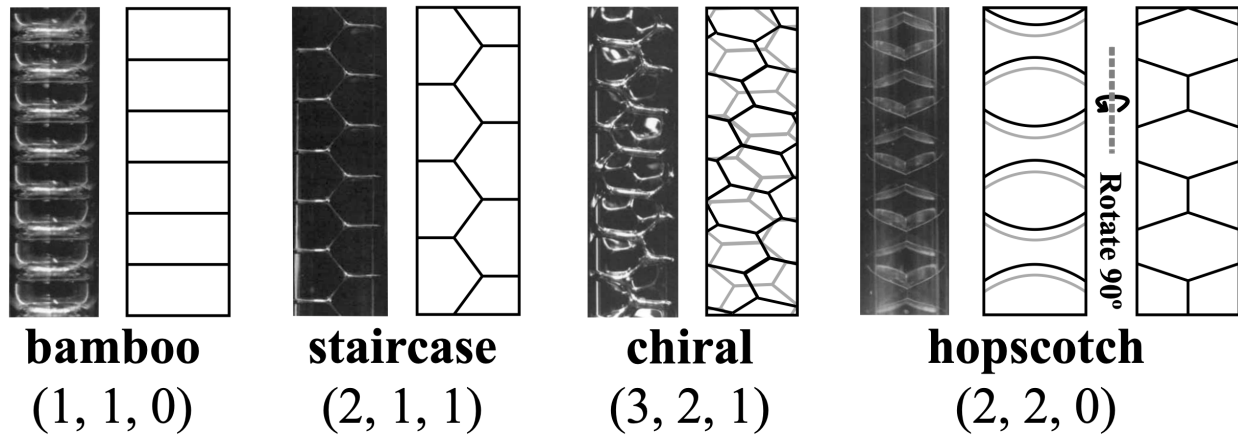


Figure 1.3: Patterns bamboo, staircase, chiral, and hopscotch as they appear in foams [12] (left) and sketched to show structure (right). The vector notation is defined in Chapter 2.

The transition between the bamboo and staircase patterns, which are illustrated in Figure 1.3, was studied analytically, experimentally, and numerically by Reinelt et al. for dry foams, which are foams with negligible liquid volume and thus are completely space-filling. The difference between wet and dry foams is illustrated in Figure 1.4. It has been shown that the transition from staircase to bamboo pattern that is forced by stretching a dry foam occurs because the equilibrium staircase pattern becomes unstable due to a saddle node bifurcation in the system energy; it was previously assumed to happen because an edge of a bubble moved continuously toward zero length [29].

Dry foams with internal bubbles that have no surface on the tube wall have been observed experimentally to behave similarly to less complex foams on the tube wall, but the interior bubbles form a variety of interesting structures. These structures have also been

successfully simulated with the Surface Evolver [30], a finite elements program designed to minimize surface energy. Surface Evolver is discussed in detail in Section 4 of Chapter 3.

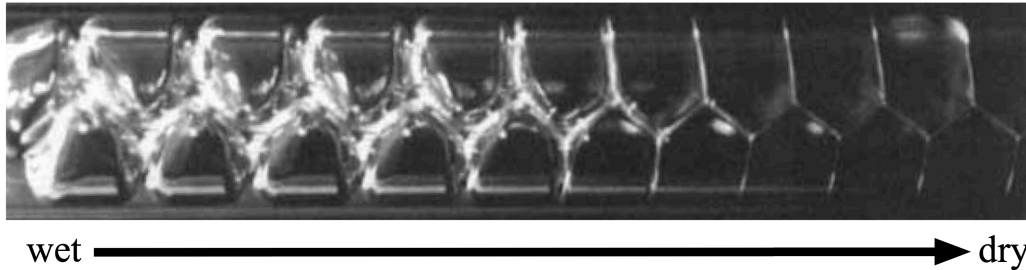


Figure 1.4 Tube containing a foam in transition from wet to dry. Note that wet foam appears to have space between the bubbles because wet foams possess a significant amount of liquid volume. Foam image from [12].

In addition to foams contained in circular cylinders, foams in tubes with some non-circular cross sections have been studied. This includes those with triangular or square cross sections, and these tubes have been shown to form not only patterns similar to those formed in circular tubes, but also patterns unique to their specific cross section shape [12, 35].

1.2. Foam Modeling as a Basis for Notochord Pattern Identification

To examine the process of notochord morphogenesis and cellular patterning, Dr. Michel Bagnat's research group at Duke University studied the effects on packing of genetic manipulation of the number of cells in the zebrafish notochord [23]. Pattern classification thus far has existed only for identical bodies in rigid cylinders, like foam in a hard tube [13, 23, 26, 35]. Further complicating the creation of a notochord model, unlike in foams, multiple patterns can appear in different portions of the same fish's notochord. To identify the different patterns and how they vary between various mutant fish, we have developed an algorithm to classify patterns formed by weakly polydisperse disordered bodies packed in a weakly bent tube of variable cross section using foam patterning notation; see Chapter 2. The results of analysis

with this algorithm show that mutants with lower density of cells per unit length, mutants with a higher density of cells, and wild type (unmodified, abbreviated WT) zebrafish each form the same patterns - commonly called bamboo, staircase, and chiral - but these patterns appear with different frequency for each type of fish, and that frequency is governed by the ratio λ of cells per unit length.

Dr. Bagnat's group also created a physical bead model of the notochord using flexible silicone tubing and gel beads that swell when placed in water [23]. The patterns of the beads in this physical model resemble the patterns of cells in the notochord as λ is varied, including the coexistence of multiple patterns in one tube; see Figure 1.5. One of the key results of this nonliving model is that the cross sections of the tubes were observed to be elliptical, rather than circular, in areas where beads form the typical notochord staircase pattern. A second experiment was performed with the beads using a tube that was rigid and had an elliptical cross section, and they noted an extreme bias for the staircase pattern over all others [23]. The results of the gel bead experiments are presented in Figure 1.5.

Although the gel beads are mechanically different from bubbles, their patterns formed are remarkably similar. In both the physical model and the zebrafish notochord, we observed a correlation between cross-sectional shape and observed pattern. A tube or notochord with an elliptical cross section presents with staircase pattern more frequently than one with a circular cross section, and cells arranging in the staircase pattern pushes the cross section toward elliptical.

The behavior of the physical model suggests that the notochord behaves like a packing problem, where bodies with set properties are packed into a constrained space. The key

differences between the notochord and a standard packing problem are twofold: not only can the notochord cells vary in size and shape, but the sheath of the notochord is flexible rather than rigid.

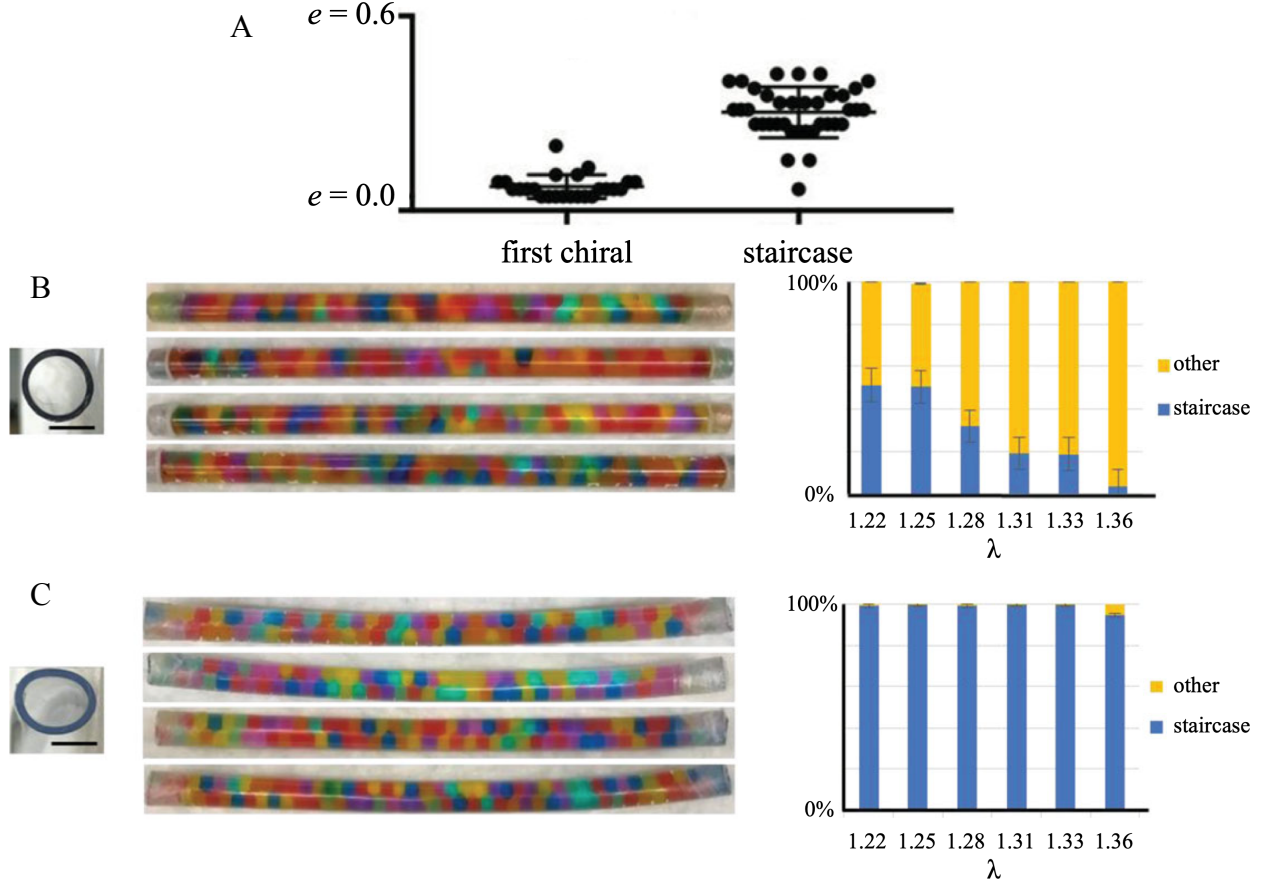


Figure 1.5: A) Eccentricity of flexible tubes containing gel beads in the staircase pattern compared to tubes containing the first chiral pattern. Tubes containing the staircase pattern consistently presented with higher eccentricity than those with first chiral ($n = 6$ tubes, $*p < 0.0001$, Welch's t -test). From [22]. B) Rigid tubes with eccentricity $e = 0$ containing gel beads. The occurrence of staircase pattern varies with λ , but it never occupies more than half the tube. C) Rigid tube of eccentricity $e = 0.6$ containing gel beads. The staircase pattern is dominant for all λ tested.

In Chapter 2 we present the new sorting algorithm used in the data analysis for [23] and explain in detail its utility for notochord analysis. In Chapter 3, we also elucidate the packing problem of soap foams in tubes and expand the results of the earlier foam packing studies to three previously unexamined general cases. We believe these foam models will have useful and

unique biological applications, since notochord cells have been observed to form patterns similar to those of foams [10], and the resulting model analysis has direct implications for the mechanical properties of the notochord.

Chapter 2

Two Algorithms for Biological Pattern Identification in Cylinders

2.1. Ordered Patterns in Foams

To provide context for a discussion of pattern formation in cylinders, we first need to describe the variety of ordered patterns found in foams that are relevant to our biological system. We will use the phyllotactic notation adopted by [26] to describe patterns in their study of foams. Phyllotaxis, also sometimes called “generalized crystallography,” is the symmetry and asymmetry of the arrangement of the lateral organs of plants, like seeds on a sunflower or leaves on a stem [28]. These lateral organs arrange themselves into spirals, and the spirals form families based on their relative orientation. The number of spirals n in a direction required to complete the spiral pattern categorizes those spirals as an n -parastich [37]. In a grouping of hexagonal-faced cells, such as those formed by monodisperse, ordered foams, this leads to three n -parastiches with $n = k, l$, and m . These integers are listed in non-increasing order, with k representing the steepest spiral, and we call the corresponding structure a (k, l, m) pattern.

For a bounded structure of hexagonal-faced cells, there is an alternative method to determine (k, l, m) . With the structure oriented so the spirals are around the z -axis, cells are numbered from bottom to top starting at 1. For each cell with index i , we note that its three neighbors have indices $i + k$, $i + l$, and $i + m$. The pattern at cell i is thus denoted (k, l, m) , where $k = l + m$, is a proven relationship in phyllotaxy; see [28], for example. If a cell has fewer than three distinct neighbors, a neighbor is counted for each of its contacts with the cell in question. We provide an example of this pattern-finding process in Figure 2.1.

For a basic cylindrically-bounded foam model, it is assumed that cells are monodisperse, and that any pattern they form is ordered and consistent through the entire bounding cylinder.

Therefore, finding the pattern at one body is equivalent to finding the pattern globally. We refer to such patterns as regular patterns.

The notation for patterns has not been chosen arbitrarily; it contains information about

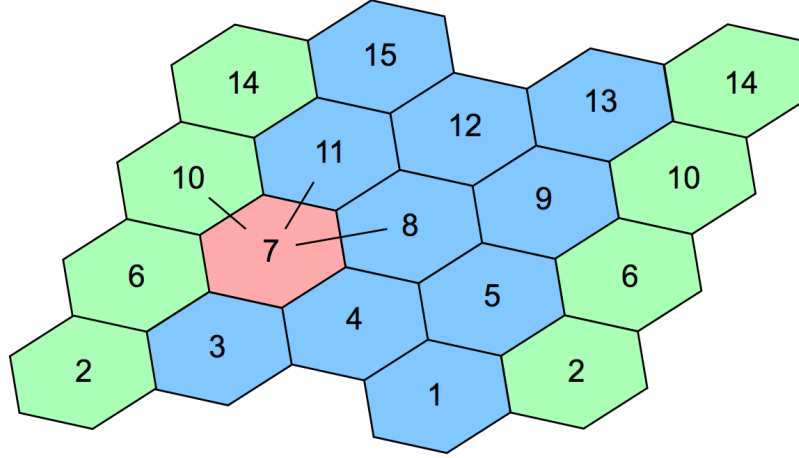


Figure 2.1: Example of a structure of two-dimensional hexagonal cells, which result from the “unwrapping” the surface of a cylinder with this surface pattern. The surface of the cylinder is separated at the lighter, green cells, so they are included on either side to facilitate the observation of neighbors. Examining the 7th cell, for example, we see its neighbors have indices 8, 10, and 11. Then $k = 11 - 7 = 4$, $l = 10 - 7 = 3$, and $m = 8 - 7 = 1$, so this structure is in the $(4, 3, 1)$ pattern; note that $k = l + m$ as expected.

the relationship between the bounding cylinder and the cells contained within it. Let V_i be the smallest vector which takes body i to an equivalent body; note that this is not the same as the previously defined pattern vector $\langle k, l, m \rangle$. Let D denote the diameter of the cylinder, and let d be the diameter of a circle with area equal to that of the hexagon formed by the contact of a cell with the cylinder wall. It follows that

$$\begin{aligned} \|V_i\|^2 &= \left(k - \frac{m}{2}\right)^2 + \frac{3}{4}m^2 \\ &= l^2 + lm + m^2 \\ &\approx (\pi\lambda)^2 \end{aligned} \tag{1}$$

where λ is the dimensionless ratio D/d . This approximation results because $\|V_i\|$ is the smallest vector that can be wrapped around the tube from one cell, back to that same cell. Because $\|V_i\|$ is defined from pattern rather than cell and cylinder dimensions, it measures the circumference of the tube in terms of cell length. Therefore, $\|V_i\| \approx \pi D/d = \pi \lambda$. We note here that this definition of λ is slightly different from the definition that will be used throughout the rest of the paper in that here λ is used in a two-dimensional setting as diameters of circles. The usual definition of λ is for measurement in three-dimensions and uses diameters of spheres instead.

As previously stated, we assume that any pattern within a bounding cylinder is repeated throughout the entire cylinder, so computing $\|V_i\|$ for one cell is equivalent to finding it for all cells in the same relative position within the pattern. It will become apparent that the definition of V_i in Equation (1) is crucial to the further comparison of patterns between systems. It provides a way to relate pattern notation to the parameters measured in the system being examined. Furthermore, it associates a dimensionless parameter λ with each pattern, allowing us to compare patterns in systems with drastically different sizes.

Based on the maximum observed value for λ in the WT notochord, we can assume that there will be no patterns relevant to the notochord with $k \geq 4$. This means there are only four regular patterns of potential interest to us: (1, 1, 0), (2, 1, 1), (2, 2, 0), and (3, 2, 1), which have $\|V_i\| = 1, \sqrt{3}, 2$, and $\sqrt{7}$. We will refer to these patterns as bamboo (b), staircase (S), regular hopscotch (H), and first chiral (c), respectively; we provided examples of these patterns in foams in Figure 1.3.

These same patterns appear in packing of hard spheres in cylinders, although these hard sphere patterns are determined by contact points between the hard sphere and the cylinder wall,

whereas foam patterns are determined by the configuration of edges in contact with the wall. For hard spheres, the wall is “unwrapped” to a plane, forming a two-dimensional lattice. A similar technique can be applied to foams; the point used for each bubble is the center of the surface of the bubble that is in contact with the wall. Significant work has been performed examining transformations of this lattice and the resulting patterns, especially of hard spheres [19, 20]. It has been noted that hard spheres will exhibit shears and line-slips, creating modified versions of standard patterns [19, 20]. However, although these modifications can be seen in moving foams, they do not occur in foams in equilibrium and are therefore not considered here.

2.2. Packing of Irregular Bodies

Our analysis of patterns in irregular bodies was motivated by the data Dr. Bagnat’s group acquired on three-dimensional cell position and volume from zebrafish notochord confocal microscopy. The imaging process was as described in [23], and segmentation was carried out using ImarisCell, a well-known imaging software widely used in biological applications; see Figure 2.2 for an example. It uses a unique segmentation algorithm, presented in [6], which automates the segmentation process and removes the majority of visual confirmation required from the user.

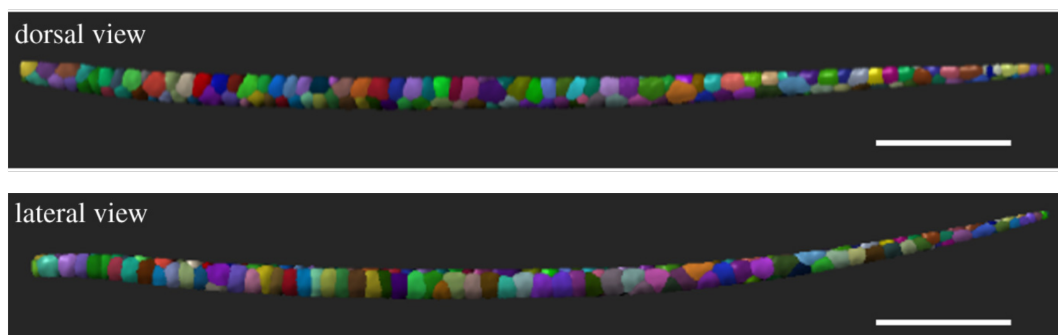


Figure 2.2: Dorsal and lateral view from a three dimensional rendering of a WT zebrafish notochord [22] carried out with ImarisCell [5]. The existence of nonzero curvature of the notochord is particularly clear in the lateral view.

The first hurdle in working with notochord cell data is that the notochord itself is curved and tapered, as seen in Figure 2.2. The fish was manually, but imperfectly, aligned in the x, y, z coordinate system along the x axis; because of this rough alignment, we were able to assess the existence of twists in the notochord. We observed that the curvature of the notochord was largely in the xy plane with no twisting. Thus, to straighten the notochord stack we created a new coordinate system, denoted (X, Y, Z) . We found the midline of the notochord by using cubic spline interpolation, performed in JMP using their built-in package, to create a best fit curve to the centroid positions in the xy and xz planes. The new coordinate system was then defined as

$$(X, Y, Z) = (x - x_{min}, y - y_{spline}, z - z_{spline}) \quad (2)$$

where x_{min} is the lowest x value in the dataset. This gives us a straight notochord that begins at $X = 0$.

While this addresses the straightening of the notochord effectively, the tapering still needs to be addressed. Dr. Bagnat's team at Duke was able to provide us with some measurements of the notochord cross-sectional dimensions, but we found the potential error margin on these to be too high because they were found using the notochord sheath cells rather than the interior notochord cells. While theoretically these should yield the same measurements, we found that the sheath cross section images had too much noise for distances to be measured consistently. Instead, we computed the cross-sectional area as $A = dV/dX$, which is equivalent to finding the cross-sectional area at centroid i as c , where v_i is the volume of the i^{th} cell, and ΔX_i is the distance in the X direction between ordered cells i and $i - 1$. We found the diameter D_i of a circle with area A_i at each X position as $D_i = 2\sqrt{A_i/\pi}$. We then used the same spline

smoothing method in JMP on the diameters to find \hat{D}_i , which we used to calculate the radius r_i at each X position, giving us the new radially normalized YZ coordinates as $(\hat{Y}, \hat{Z}) = (Y/r, Z/r)$. We then normalized X by scaling Δx by the local volume, yielding the final normalized coordinates of $(\hat{X}, \hat{Y}, \hat{Z})$. We denote the sequence of centroid positions in the new coordinate system, ordered by \hat{X} position, as K_n .

Scaling centroid positions radially in the (\hat{Y}, \hat{Z}) plane provides us with another metric to compare patterns, both between individual zebrafish and between entire zebrafish strains; we can create a cross-sectional heat map of the centroid positions for each strain of fish, as shown in Figure 2.3. The utility of these heat maps in pattern analysis is illustrated in Section 2.3 of this chapter.

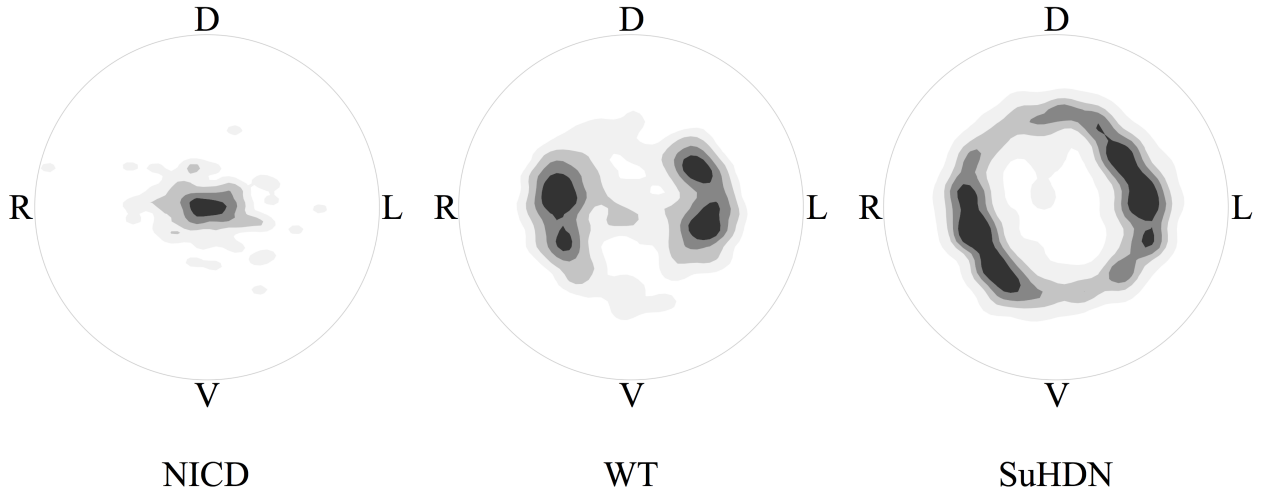


Figure 2.3: Heat maps of notochord cell centroid positions in transverse view using four fish from each strain; NICD is a mutant strain with the lowest density of cells per unit length, and SuHDN is a mutant strain with the highest density of cells per unit length. All cross sections are oriented with the dorsal (D) side on the top and ventral (V) side on the bottom, which are aligned with our \hat{Z} axis; the right (R) and left (L) are relative to the orientation of fish and are aligned with the \hat{Y} axis. From [22].

Previously discussed foam and hard sphere pattern analysis results rely on the “unwrapping” process to analyze the patterns formed on the surface of the bounding cylinder. In

our case, however, due to the limitations of segmentation the only position data we have are the centroids of cells, and these are not all equidistant from the midline. Therefore, even if we were to project the centroids to the bounding surface, the results would be meaningless, especially for cells with centroids particularly close to the midline. Instead, we created two new pattern identification methods, both stemming from one key observation: centroid positions are nearly periodic as we move along the X axis. That is, for the first centroid in any pattern, there is a centroid with approximately the same \hat{Y} and \hat{Z} values after a fixed number of centroids. This value is unique to each pattern. For bamboo, each sequential centroid has approximately the same \hat{Y} and \hat{Z} position; for staircase, this happens every other centroid, and for first chiral every third. In carefully controlled foam experiments, we would expect this centroid positioning for each periodicity to be more precise than in notochords.

2.3. Hopscotch Patterns

One of the unexpected results of packing cells in the physical gel bead model and in the notochord, compared to packing soap foam or hard spheres in a tube, is the relatively frequent appearance of the pattern we have named the regular hopscotch pattern, (2, 2, 0). In foam experiments, this pattern appears rarely and only under highly specific conditions [26]. For the notochord, however, the range of parameters for which regular hopscotch appears seems to be much larger. Additionally, the notochord presents a unique pattern, which we have named irregular hopscotch. Regular and irregular hopscotch are illustrated in Figure 2.4.

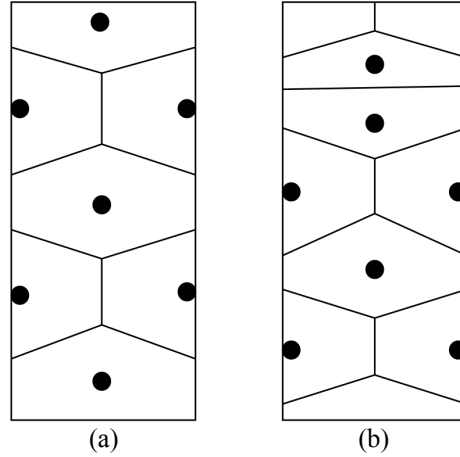


Figure 2.4: Sketch of several cells in the (a) regular and (b) irregular hopscotch patterns. In foams, regular hopscotch alternates between horizontal pairs of bubbles and a single bubble that spans the entire diameter of the tube. Irregular hopscotch is characterized by having either one or two bubbles stacked irregularly between the horizontal pairs of bubbles.

2.4. Two Algorithms for Pattern Identification

While working with notochord data, we need a way to numerically distinguish patterns, especially ones that are visually ambiguous. We developed two related pattern identification methods, which we call the *radial algorithm* and the *projection algorithm*. These methods were both motivated by the centroid heat map figures, like those in Figure 2.3. We noticed that areas of the notochords dominated by patterns that we could visually identify as bamboo had centroids largely clustered close to the midline, whereas areas that were visually determined to be staircase formed two distinct clusters of centroids and first chiral presented a more evenly distributed ring of centroids. This led to the previously mentioned definition of cell periodicity: for the lowest index centroid K_j in any pattern, there is a centroid with approximately the same \hat{Y} and \hat{Z} values after a fixed number of subsequent centroids.

This definition of periodicity is insufficient to categorize every cell in the notochord because aside from the straightforward case when adjacent cells are in the same pattern, there are

also cells that form a transition from one pattern to the next. These transitions are denoted BS for bamboo-staircase, BC for bamboo-chiral, BH for bamboo-hopscotch, SC for staircase-chiral, SH for staircase-hopscotch, and CH for chiral-hopscotch. The order of patterns - e.g. transitioning from bamboo to staircase versus staircase to bamboo - is irrelevant. Notably, not all of these possible transitions were observed in the zebrafish notochord.

After periodicities of each centroid are assigned a connection type using one of the algorithms described subsequently in Sections 3.1 and 3.2, individual cells are then assigned to a pattern based on the periodicities of adjacent cells. Both algorithms share the notation T_n for the sequence of cell periodicities and K_n for the sequence of cell centroids, and both ordered by

$$D_k = \sqrt{\left(\hat{Y}_j - \hat{Y}_{j+k}\right)^2 + \left(\hat{Z}_j - \hat{Z}_{j+k}\right)^2} \quad (3)$$

ascending cell X position. Computationally, T_n is implemented as a cell array in Matlab, allowing it to store both integer and character data.

2.4.1. Radial Algorithm

We designed the radial algorithm to identify three different periodicities, denoted period one (P1), period two (P2), and period three (P3). For each centroid $K_j = (\hat{X}_j, \hat{Y}_j, \hat{Z}_j)$ in the sequence of centroids, we calculate the distance of the centroid from the midline as for $k = 1, 2$, and 3 . Periodicity for cell K_j is the lowest value k for which $D_k < R_{tol}$, and $T_j = k$. If $D_k > R_{tol}$ for all tested values of k the periodicity of K_j is undetermined and $T_j = U$. After the algorithm completes its sorting, cells flagged as undetermined must be manually assessed for periodicity.

2.4.2. Projection Algorithm

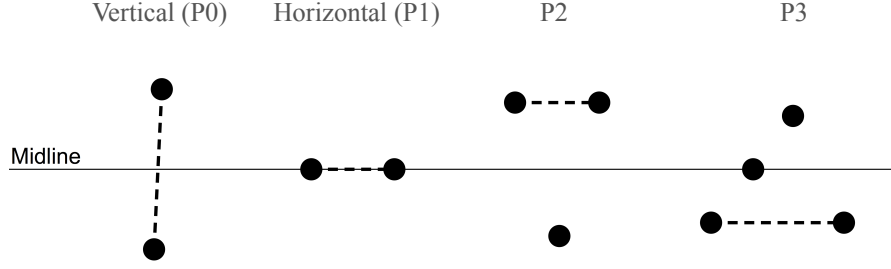


Figure 2.5: The four types of cell periodicities used for the projection algorithm.

For the projection algorithm, we define the periodicities as vertical (P0), horizontal (P1), period two (P2) and period three (P3), illustrated in Figure 2.5. At the pattern assignment step, following the periodicity algorithm, we also flag potential areas where cells transition between patterns by tagging cells adjacent to two different patterns. This is not strictly necessary for pattern identification, but helps automate the process of displaying and analyzing data.

For each element K_j in the sequence of centroids, we find the vector $v_{k,j}$ defined as by the vector connecting centroids K_j and K_{j+k} for $k = 1, 2$, and 3 , and determined simply from $K_{j+k} - K_j$. For each value of k , we compute

$$V_k = v_{k,j} \cdot \langle 1, 0, 0 \rangle \quad (4)$$

to project the vector $v_{k,j}$ onto the midline. We then compute the cosine of the angle between vectors $v_{k,j}$ and $v_{k+1,j}$ as

$$\cos(\theta) = \frac{V_j}{\|v_{k,j}\|} \quad (5)$$

because $\langle 1, 0, 0 \rangle$ is a unit vector and therefore has unit norm.

The value $k = 1$ is a special case. We first check the cosine of the angle between $v_{1,j}$ and $\langle 1, 0, 0 \rangle$ to see if $\cos \theta > 0.9$, indicating that the vector $v_{1,j}$ is approximately parallel to the notochord midline. Although this means that the angle between vectors can range up to 25° , we determined that this was a sufficient categorization for a period one pattern using angles measured in notochords with visually clear bamboo pattern. If the midline and vector are sufficiently close to parallel, the periodicity of centroid K_j and K_{j+1} is then labeled as P1. We then check to determine if the cosine of the angle between $v_{1,j}$ and $\langle 1, 0, 0 \rangle$ is lower than 0.1, indicating that the vector $v_{1,j}$ is within approximately 5° of perpendicular to the midline. This identifies the connection as P0, and centroids K_j and K_{j+1} are then labeled as P1.

We then check the vectors $v_{2,j}$ and $v_{3,j}$ in that order to see if the angle between either vector and the midline are sufficiently close to zero using the same thresholds as with the P0 and P1 periodicities. The periodicity associated with K_j is defined as the lowest value k for which the above conditions hold. Any centroids between K_j and K_{j+k} are also defined as having this periodicity, due to the definition of periodicity as illustrated by Figure 2.5. The additional conditions on $k = 1$ are necessary to accurately identify hopscotch pattern cells. The MATLAB code for this algorithm, which includes specific tolerance values, can be found in Appendix E.

This method is sufficient to categorize all centroids in our notochord data sets. However, for other sets with larger λ , there will be blank elements in the sequence T_n . These correspond to more complicated patterns resulting from larger λ and have not been observed during this phase of zebrafish notochord formation. Simply allowing for k to be larger does not include all of the

higher order patterns, and significant further work would be required to create an algorithm that works for all k . These patterns, however, are of no biological interest with respect to notochords.

2.5. Periodicity Sorting and Pattern Classification

Once the sequence of periodicities T_n has been found, we use it to determine the actual patterns occurring within the notochord. It is necessary to use the periodicities of neighboring connections to determine if the cells are transitioning from one pattern to another. We provide a visualization of the following sorting algorithm in Figure 2.6. For each element T_j , we examine the elements T_{j-3} through T_{j+3} . First, we check T_j for periodicities in the order P1, P0, P2, P3 to avoid any conflicts arising from the inherent overlap of the hopscotch and bamboo patterns, since both patterns include cells with centroids very close to the midline. The key to distinguishing between the two is to check the periodicity of the connections to and from the cell in question.

2.6. Algorithm Comparison

The radial and projection algorithms are closely related, but we found that the projection algorithm agreed more closely with our visual identifications of patterns. Furthermore, the projection algorithm can identify hopscotch patterning where the radial algorithm cannot, due to the radial algorithm's independence from the x position of centroids. Identifying patterns from only the centroid positioning in the yz plane will miscategorize the near horizontal portion of the hopscotch pattern as staircase.

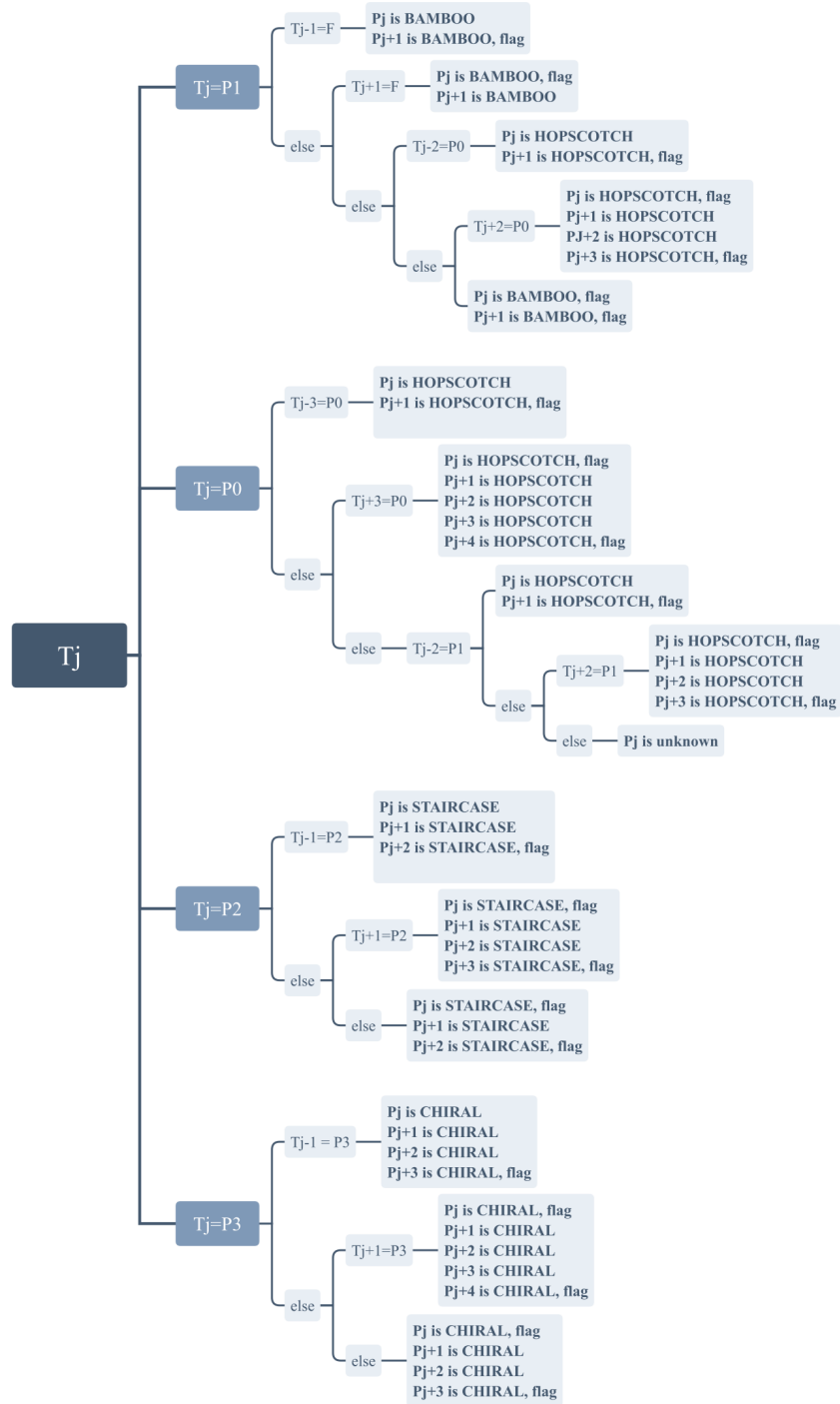


Figure 2.6: Sorting algorithm used for categorizing cells into a pattern array P_n based on periodicity. The order in which the element T_j is checked for periodicity is required to correctly identify all patterns. Connections between cells are flagged to mark potential transitions between patterns.

Since hopscotch has been identified as a stable and common pattern for the notochord, even though it exists only under highly specific conditions for foams, this makes it a novel pattern, and our ability to detect it is therefore particularly important in the notochord context. Because of its inability to detect the hopscotch pattern, the radial algorithm was deemed to be too prone to error for identification of irregular patterns, and therefore the projection algorithm was used for the data sorting reported in [23]. The published paper that resulted from this work can be found in Appendix F.

Chapter 3

Packing in Elliptical Cylinders

From the results of the genetic manipulation experiments performed for Chapter 2, we were able to analyze the dimensions of notochords of zebrafish through manual measurements of cross-sectional slices of confocal microscopy stacks. We studied the cross-sectional eccentricity e , which is effectively a measurement of the aspect ratio of an ellipse, with $0 \leq e \leq 1$; see Figure 3.1. We determined that wild type zebrafish is in the range of $e = 0.3$ to $e = 0.4$. This is significantly ($p < 0.0001$) different from zero, making a perfectly circular cylindrical tube a suboptimal model for notochords.

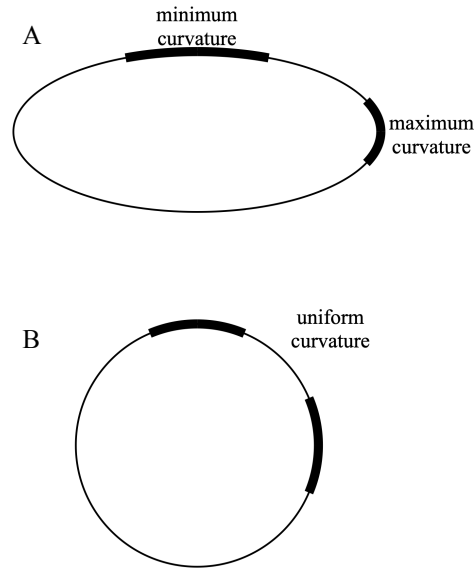


Figure 3.1: Example of ellipses with different eccentricities, with A) $e = 0.9$ and B) $e = 0$.

As foams in elliptical tubes have yet to be studied and have a stronger relationship to the zebrafish notochord behavior than foams in circular tubes, we present three novel models of tubes containing foams. These models are a rigid elliptical tube of fixed eccentricity; a semi-flexible elliptical tube, with eccentricity treated as a dependent variable and part of the energy

minimization; and a fully flexible sheath that is not constrained by any fixed geometry and is fully dependent on surface tension ratios.

3.1. Continuous Models

Our primary goal for the creation of these models was to be able to compare the results of energy minimization for tubes of different eccentricities under different constraints without changing cross-sectional area. This allows us to easily compare our results with those of physical foam experiments [13, 25, 26, 38]. In these experiments, the tube is a fixed size, and the monodisperse bubbles packed in the tube are varied in volume for each trial to yield different λ values. The changes in pattern as λ is varied in foam experiments are illustrated in Figure 3.2. There has been extensive analysis of foams in rigid tubes of circular [13, 25, 26, 29, 38] and other [35] cross sections, but there are no published studies of elliptical cross sections. Using an elliptical tube for our models with geometric boundary conditions allows us to specify the cell volume v in terms of λ and the cross-sectional area; because the relationship between λ and cell patterns is well-studied for the problem of a perfectly circular tube, this allows us to directly analyze the additional effect that varying eccentricity has on pattern formation. As mentioned in Chapter 1, the λ -pattern relationship has also been studied for other cross sections, including square and triangular [11, 34], but these are of no interest biologically and are not considered here.

Our first assumption for all three models is that the bounding tube or sheath is infinitely long; this eliminates any effects from the ends of the tube on pattern behavior. This aligns conceptually with foam experiments, since those experiments are performed in long open-ended

tubes, meaning the pattern observed in the center of the tube is at equilibrium and assumed to be unaffected by the boundary conditions from the far away open top and bottom [13, 25, 37].

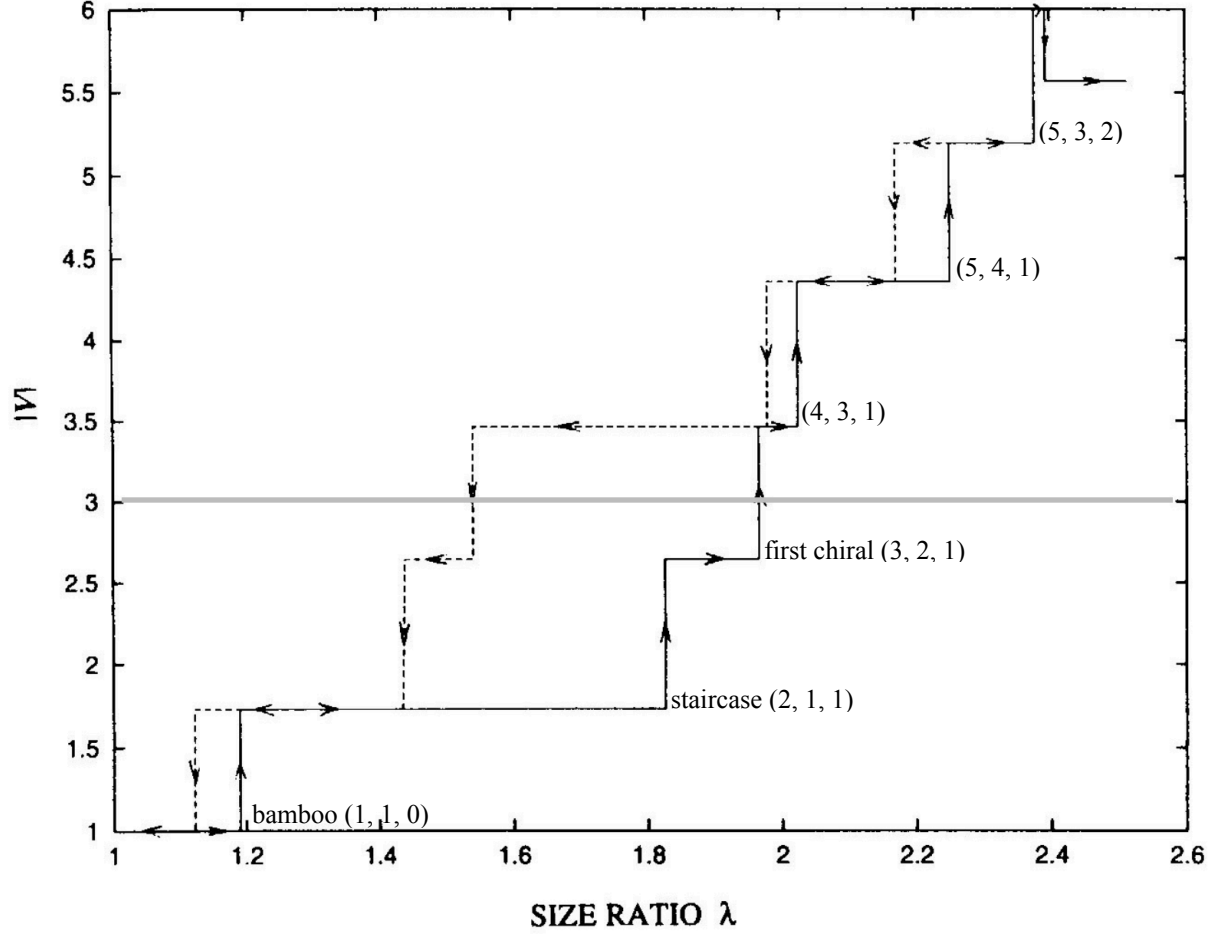


Figure 3.2: Variations in λ cause changes in pattern in foam experiments. The solid line represents pattern transitions as λ is increased, and the dashed line represents pattern changes as λ is decreased. Patterns above the grey line have not been observed in the zebrafish notochord. The difference in pattern transition points indicates a range of λ for which a pattern is stable. The variable $|V|$ is a numerical characterization of different patterns, and the computation of this value for different λ values is discussed in Section 2.1. Original figure from [12], annotations added.

Under the infinite tube assumption, we can simplify our models further to a representative length of tube and assume that the pattern in this length is tessellated above and below the representative section, which we will refer to as the *fundamental region*. Because our primary interest is the transition between bamboo and staircase patterns, both of which can be

considered period 2, the fundamental region of our models contains two cells. We denote the dimensional height of the fundamental region as h .

We are modeling notochord cells as a dry foam; see Figure 1.4 in Chapter 1. One of the properties of dry foam is that the foam is completely space-filling, so we may assume this property of our cells as well. We are further assuming that all cells are of equal volume and pressure, so each cell must occupy precisely half of the fundamental region within the tube. This means that any patterns that do appear can be assumed to be regular as defined in the first section of Chapter 2. Therefore, we can compute the total energy of the fundamental region and halve it to find the energy per individual cell in the infinite tube.

The purpose for all three models is straightforward: minimizing average surface energy per cell, denoted $\hat{\Omega}$, constrained by a periodic boundary condition $(x, y, 0) = (x, y, h)$ and by conservation of volume. However, the mechanics of the sheath are treated differently in each of our three models and may provide additional constraints. The three different sheath models are presented here ordered from maximally to minimally constrained.

3.1.1. Rigid Sheath Model

To mirror some of the experiments with the gel beads discussed in Chapter 1, and to provide an analysis of a system which has not yet been explored in foams literature, we begin with a model for a rigid elliptical tube of eccentricity e and cross-sectional area S , filled with cells (or bubbles) of equal volume v ; the combination of prescribing cross-sectional area and cell volume results in a fixed height for the fundamental region, which yields

$$h = \frac{2v}{S} \tag{6}$$

The cross section depicting the employed geometry is shown in Figure 3.3. Since the tube in this scenario is inflexible, it forms a bounding surface for the internal foam cells. This means that we only need to minimize average internal cell-cell surface area, since the surface area per fundamental region of the rigid tube is fixed.

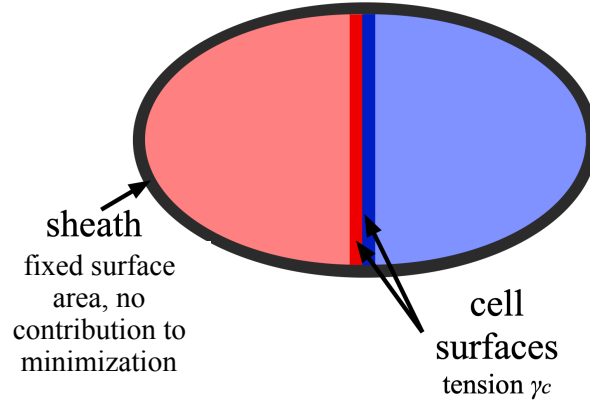


Figure 3.3: Sketch of the cross section of the configuration used for the rigid model. Two cells are shown, one in red and one in blue, with the sheath drawn in black. The surface being minimized is the one formed by cells in contact with each other, not the cell surface in contact with the sheath. The sheath is rigid and therefore is ignored in energy minimization.

Aligning the cylinder so its base is perpendicular to the z axis, we can assign the direction of the major axis of the elliptical cross section without loss of generality, so we choose to have the major axis on the x axis. Because of this, our semi-major and semi-minor axes are denoted r_x and r_y , respectively, so the equation for the bounding ellipse is

$$\left(\frac{x}{r_x}\right)^2 + \left(\frac{y}{r_y}\right)^2 = 1 \quad (7)$$

Therefore, eccentricity is thus defined as

$$e = \sqrt{1 - (r_y/r_x)^2} \quad (8)$$

with $0 \leq e < 1$.

We can derive expressions for the geometric properties of the tube with respect to the cross-sectional area S and ellipse eccentricity e , which are the parameters dealing with the boundary. Thus, we derive expressions for r_x and r_y as

$$\begin{aligned} r_x &= \sqrt{\frac{S}{\pi\sqrt{1-e^2}}} \\ r_y &= r_x\sqrt{1-e^2} \end{aligned} \tag{9}$$

and note that these are functions of fixed parameters e and S . Our problem is then minimizing the surface energy $\sum_i \Omega_i$ of the cells in the fundamental region, constrained cross-sectionally by an ellipse with the axes described above. Generally, we define surface energy as the energy from tension over the surface in question. This surface energy minimization is therefore equivalent to minimizing $\sum_i \sum_j A_{i,j} \gamma_{i,j}$ where $A_{i,j}$ is the area of the j^{th} internal face of the i^{th} cell and $\gamma_{i,j}$ is the interfacial tension affecting the j^{th} internal face of the i^{th} cell. Since we are using a fundamental region of cells to represent the entire system, the minimization is over the two cells in a fundamental region. We can now determine our dimensional objective function Ω , and we will then nondimensionalize to yield $\hat{\Omega}$.

Since the interfacial tension γ_c is fixed, our objective function, which represents the minimizable energy per cell in the fundamental region, is

$$\Omega(\gamma_c, e, S, \lambda) = \sum_j A_j(e, S, \lambda) \gamma_c \tag{10}$$

Here A_j is the surface area of the j^{th} interior face of an interior cell. Since Ω is a function of v , S , γ_c , e , and λ , this means that, since λ and e are dimensionless and S can be computed from v and λ , we can express the units of Ω as

$$[\Omega] = [\gamma_c]^a [v]^b \tag{11}$$

However, since Ω is defined to be an energy, and therefore $[\Omega] = L^2 M T^{-2}$, and as a tension term we have $[\gamma] = M T^{-2}$, this means $a = 1$ and $b = 2/3$, so

$$[\Omega] = [\gamma_c] [v]^{2/3} \quad (12)$$

and we therefore define our nondimensional objective function for the rigid tube model as

$$\hat{\Omega} = \frac{\Omega}{\gamma_c v^{2/3}} \quad (13)$$

Our problem thus consists of finding surfaces that minimize $\hat{\Omega}(\lambda, e)$ under three constraints. The first two are the conservation of volume and periodic boundary condition common to all three models. Let E be the region within the cylinder contained in the fundamental region whose base is the ellipse described by $\frac{x^2}{r_x^2} + \frac{y^2}{r_y^2} = 1$, where r_x and r_y are as given above. Then our last constraint is that all cell-sheath surfaces are in ∂E and that all cell-cell surfaces lie in the interior of E .

To find analytical solutions to this problem, we consider specific cases. First, we consider the energy of a cell in bamboo pattern. Since the only energy contributed to minimization comes from the product of interfacial tension and surface area, the only surfaces we need to consider are the top and bottom of the cell. However, we have constrained this problem to have constant cross-sectional area S , so the energy per cell in bamboo pattern is $\Omega_B = 2S\gamma_c$ giving nondimensional energy per cell $\hat{\Omega}_B = 2$, independent of eccentricity and λ . The transition from the bamboo pattern to staircase should occur when the energy in the staircase configuration, denoted $\hat{\Omega}_S$, is lower than $\hat{\Omega}_B$, so the theoretical transition point between patterns should occur once $\hat{\Omega}_S \leq 2$. There is no analytical geometric expression in three dimensions for the interior surfaces of a cell in the staircase configuration, and, as previously noted, foam

contained in circular cylinders has been shown experimentally to have stable patterns across λ ranges, some of which overlap, so further examination of this transition point requires numerical simulations.

3.1.2. Semi-Flexible Sheath Model

While little is known about most of the physical properties of the notochord, we do know that its sheath is not rigid. As an intermediate model between a rigid tube and a completely flexible one, we consider a uniform elliptical tube with unfixed eccentricity, where r_x and r_y are free to vary as a consequence of system parameters and cell arrangement. Rather than providing a purely geometric boundary, as in the rigid tube problem, this semi-flexible sheath has an additional tension parameter γ_s which interacts with the surface of the inner notochord cells that are in contact with the sheath, as shown in Figure 3.4.

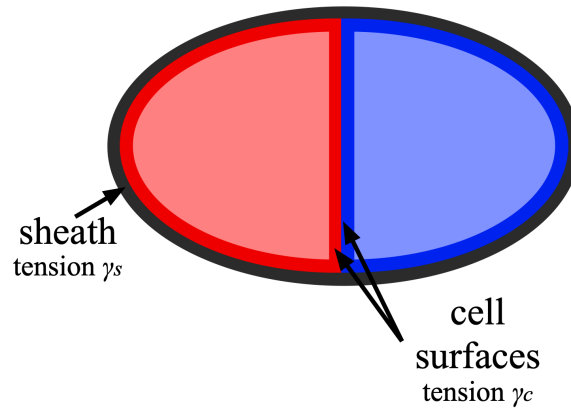


Figure 3.4: Sketch of the cross section of the configuration used for the semi-flexible model. Two cells are shown, one in red and one in blue, with the sheath represented in black. We are minimizing the surfaces that are formed by cell-cell contact combined with the surfaces formed by cell contact with the sheath.

This configuration necessitates a change in the objective function, since rather than just γ_c , we are now also considering the tension γ_s from the sheath, and because the geometric boundary constraint is a function of the free variables r_x and r_y rather than only system

parameters. From Figure 3.4 we see that the total tension on an exterior surface is $\gamma_s + \gamma_c$ since there are contributions from both cell tension and sheath tension. Thus the objective function for energy per cell must then become

$$\Omega(\lambda, S, \gamma_s, \gamma_c, r_x, r_y) = (\gamma_s + \gamma_c) A_{ext}(\lambda, S, \gamma_s, \gamma_c, r_x, r_y) + 2\gamma_c A_{int}(\lambda, S, \gamma_s, \gamma_c, r_x, r_y) \quad (14)$$

constrained by conservation of volume (by fixing λ and S), fixed cross-sectional area S , and both γ_s and γ_c fixed. Since we are no longer constraining our system purely geometrically, e has become a dependent variable rather than an independently prescribed parameter as in the rigid tube model. Along with λ , we have an additional driving ratio for this model in the nondimensional parameter $\Gamma = \gamma_s / \gamma_c$, the ratio of external to internal surface tension. In nondimensionalizing, we use a characteristic surface tension γ defined as $\gamma = \sqrt{\gamma_c \gamma_s}$ rather than using solely γ_c or γ_s . If we define $r_y = r_x \sqrt{1 - e^2}$, then Ω becomes a function of γ , Γ , S , r_x , λ , and e , and rather than S and r_x we can use cell volume v ; these changes are particularly helpful because Γ , λ , and e are dimensionless, so

$$\begin{aligned} [\Omega] &= [\gamma]^a [v]^b \\ &= M^a T^{-2a} L^{3b} \end{aligned} \quad (15)$$

Recalling that the units of Ω are $L^2 M T^{-2}$, we see that here $a = 1$ and $b = 2/3$. We therefore define our general dimensionless energy $\hat{\Omega}$ for the semi-flexible model as

$$\hat{\Omega} = \frac{\Omega}{v^{2/3} \gamma} \quad (16)$$

The constraints on this minimization are the same as for the rigid sheath model: a periodic boundary condition, conservation of volume, and a bounding elliptic cylinder. The key difference is that the ellipse described by $\frac{S}{\pi} = x^2 \sqrt{1 - e^2} + \frac{y^2}{\sqrt{1 - e^2}}$ is now also affected by the cells because the eccentricity e has become a dependent variable.

3.1.3. Flexible Sheath Model

Our final, and least constrained, model is one for a fully flexible sheath, depicted in Figure 3.5. We have $\Omega = \Omega(\gamma_c, \gamma_s, \lambda, v)$, but we can eliminate the dependence on γ_s and γ_c by using the previous definitions of $\Gamma = \gamma_s/\gamma_c$ and $\gamma = \sqrt{\gamma_s \gamma_c}$. Then $\Omega = \Omega(\Gamma, \gamma, v, \lambda)$; since λ and Γ are dimensionless, we obtain

$$\begin{aligned} [\Omega] &= [\gamma]^a [v]^b \\ &= M^a T^{-2a} L^{3b} \end{aligned} \quad (17)$$

Here we again have $a = 1$ and $b = 2/3$, resulting in the same nondimensional objective function $\hat{\Omega}$ as we used for the semi-flexible model,

$$\hat{\Omega} = \frac{\Omega}{\gamma v^{2/3}} \quad (18)$$

However, for this model our only constraints for the minimal energy surface are the volume conservation and the periodic boundary constraint common to all models.

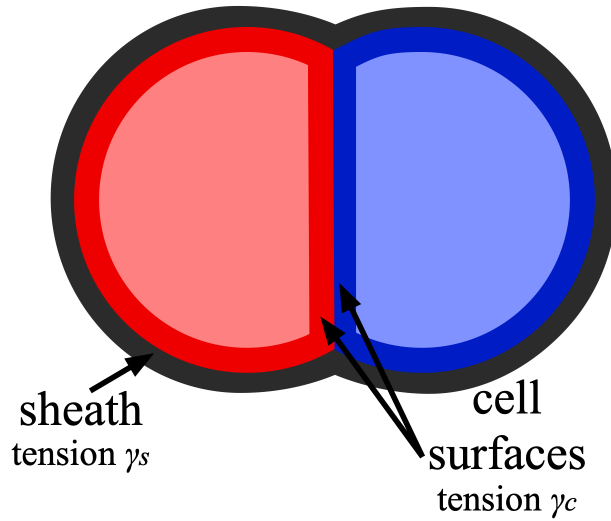


Figure 3.5: Sketch of the cross section used for the fully flexible model. Both sheath-cell and cell-cell surfaces contribute to energy and are being jointly minimized, but they are no longer constrained to have a surface on a bounding ellipse.

3.2. Discretization

While the described minimal surface problems initially appear to be relatively simple models, we run into complications when we consider the irregular shapes that the faces of our cells can potentially form. Rather than attempt to compute $\hat{\Omega}$ using geometric equations for area, we instead discretize the surfaces to find numerical solutions. Note that due to the properties of dry foams upon which this set of models is based, most importantly that there is no volume between bubbles and the foam is completely space-filling, volumes are bounded by multiple faces connected by edges, and these edges meet at individual vertices.

We will discretize faces F_i and edges into triangular facets and their associated shared edges and vertices. For all three models, the faces F_i of each cell b are approximated as a union of facets f_j with vertices v_0 , v_1 , and v_2 , connected by ordered edges s_0 , s_1 , and s_2 as shown in Figure 3.6. These vertices and edges will form the initial mesh for our models although the initial mesh will be coarse and require refinement. Solving the minimization problem then consists of iteratively moving vertices in a lower energy direction using the conjugate gradient method, modifying mesh through refinement and rebalancing, and calculating new energies.

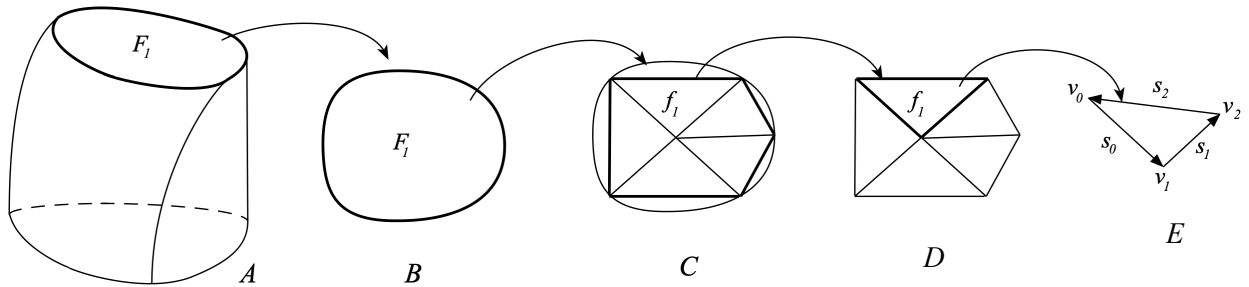


Figure 3.6: A) An arbitrary cell, B) arbitrary face F_i , C) F_i discretized into facets, D) discretization into individual facets, and E) facet f_i with vertices v_0 , v_1 , and v_2 , connected by edges s_0 , s_1 , and s_2 .

3.2.1. Rigid Sheath Model

From our continuous model described in Section 3.1.1 of this chapter, we see that our model must include the energies contributed from surface tension and from enforcing fixed cell and fundamental region volume. This is accomplished by modifying the energy using pressure as a Lagrange multiplier; since we are modeling the rigid tube wall as a bounding ellipse, we need not examine the surfaces on this boundary.

Since our discretization of a model of a curved surface on a curved boundary consists of flat facets fixed to a segmented boundary, there will be area and volume errors due to this curvature. To address this, we include an additional Lagrange multiplier in the form of gap energy, which is defined as an energy proportional to the cross-sectional area between a facet and a curved boundary; see Equation (28). Minimizing gap energy counteracts the clumping trend of vertices away from high curvature boundaries during iterative remeshing, where most edges of facets are shortened at the expense of some becoming extremely long. This uneven mesh can lead to highly inaccurate fit along the high curvature portion of the boundary. As eccentricity of the tube increases, the ratio of maximum to minimum edge curvature increases, as illustrated in Figure 3.7, so gap energy becomes vital to maintaining balance in mesh size for higher eccentricity simulations. Thus, the change to a discrete system requires us to modify our objective function from Equation (13). For a cell b with N faces, the i^{th} face F_i consists of n_i triangular facets denoted f_j . Each of these facets has three edge vectors, and we denote them as $\vec{s}_{0,j}$, $\vec{s}_{1,j}$, and $\vec{s}_{2,j}$ as shown in Figure 3.6.

Then, assuming a balanced discretization, the area of face F_i is

$$A_i = \lim_{n_i \rightarrow \infty} \sum_{f_j \in F_i} \text{area of } f_j = \lim_{n_i \rightarrow \infty} \sum_j^{n_i} \frac{1}{2} \|\vec{s}_{0,j} \times \vec{s}_{1,j}\| \quad (19)$$

We then apply a partial sum of this area equation as an approximation for surface area when we compute the energy contributed by surface tension.

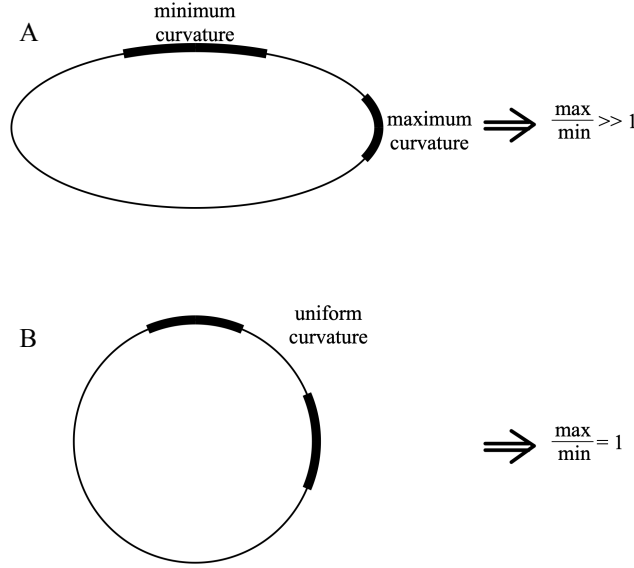


Figure 3.7: Difference in curvature ratio with A) eccentricity = 0.9 and B) eccentricity = 0.

Rather than an objective function of just surface area and tension, as in the objective function for the continuous rigid sheath model in Equation (10), we have

$$\Omega(b) = \Omega_p(b) + \sum_{f_j \in b} \left(\Omega_t(f_j) + \sum_{s_k \in f_j} \Omega_g(s_k) \right) \quad (20)$$

where $\Omega_p(b)$ is the energy from internal pressure affecting cell b , $\Omega_t(f_j)$ is the energy contributed by tension acting on facet f_j , and $\Omega_g(s_k)$ is the gap energy affecting edge s_k of facet f_j . The energies here are all dimensional, and nondimensionalization occurs at the end of the minimization process for analysis and comparison purposes. We shall now discuss the computation of these energies in further detail.

First, we can express the energy contributed from surface tension as

$$\Omega_t(f) = \frac{\gamma_c}{2} \|\vec{s}_0 \times \vec{s}_1\| \quad (21)$$

where γ_c is the surface tension affecting facet f and is assumed to be constant across the facet.

This means the force from surface tension on each vertex of f is

$$\begin{aligned} \vec{F}_t(v_0) &= \frac{\gamma_c}{2} \cdot \frac{\vec{s}_1 \times (\vec{s}_0 \times \vec{s}_1)}{\|\vec{s}_0 \times \vec{s}_1\|} \\ \vec{F}_t(v_1) &= \frac{\gamma_c}{2} \cdot \frac{\vec{s}_2 \times (\vec{s}_1 \times \vec{s}_2)}{\|\vec{s}_1 \times \vec{s}_2\|} \\ \vec{F}_t(v_2) &= \frac{\gamma_c}{2} \cdot \frac{\vec{s}_0 \times (\vec{s}_2 \times \vec{s}_0)}{\|\vec{s}_2 \times \vec{s}_0\|} \end{aligned} \quad (22)$$

Next, we consider the energy from a cell's internal pressure, which results from enforcing it as a Lagrange multiplier in the volume conservation equation

$$\nabla \Omega_p(\vec{v}) = p_c \nabla (V - V_0) \quad (23)$$

where V is the computed volume in Equation (25) and V_0 is the set volume of the cell.

For any cell b , we have

$$\Omega_p(b) = \int p_c dV = p_c V \quad (24)$$

where V is the prescribed volume of the cell, which we computed previously from λ and cross-sectional area, and p_c is the resulting internal pressure of the cell. To enforce conservation of volume, p_c is used as a Lagrange multiplier and adjusted with each application of forces to maintain the initial specified volume V_0 .

The volume of a body that has been defined as a collection of facets is computed as

$$V = \sum_{\text{facets}} \iint_{\text{facet}} z \vec{k} \cdot d\vec{A} = \sum_{\text{facets}} \frac{1}{6} (z_0 + z_1 + z_2) \vec{k} \cdot \vec{s}_0 \times \vec{s}_1 \quad (25)$$

where z_j is the z position of vertex v_j and \vec{k} is the basis vector $\langle 0, 0, 1 \rangle$. Since the volume

equation is a constraint on our system with pressure acting as a Lagrange multiplier, the force

contribution from pressure on a vertex v associated with cell b is

$$\vec{F}_p(v) = - \sum_b (p_b - p_{amb}) \vec{g}_b \quad (26)$$

where \vec{g}_b is the gradient of the volume of cell b as a function of the coordinates of the vertex v , p_{amb} is the ambient pressure, and the sum is over all cells that include vertex v in their surface.

Since we assume ambient pressure is zero, this simplifies to

$$\vec{F}_p(v) = - \sum_b p_b \vec{g}_b \quad (27)$$

The final contribution to energy is from gap energy, an energy proportional to the area between the boundary wall and the edges of a cell surface; see Figure 3.8. The gap energy for an edge s is given by

$$\Omega_g(s) = \frac{k}{6} \|\vec{s} \times \vec{q}_t\| \quad (28)$$

where \vec{s} is the edge vector and \vec{q}_t is the projection of \vec{s} onto the tangent plane of the constraining surface at the tail vertex of the edge s , as shown in Figure 3.9, and k is the gap constant; k functions like a spring constant and has units MT^{-2} . If an edge s is not part of an exterior facet, then $\Omega_g(s) = 0$.

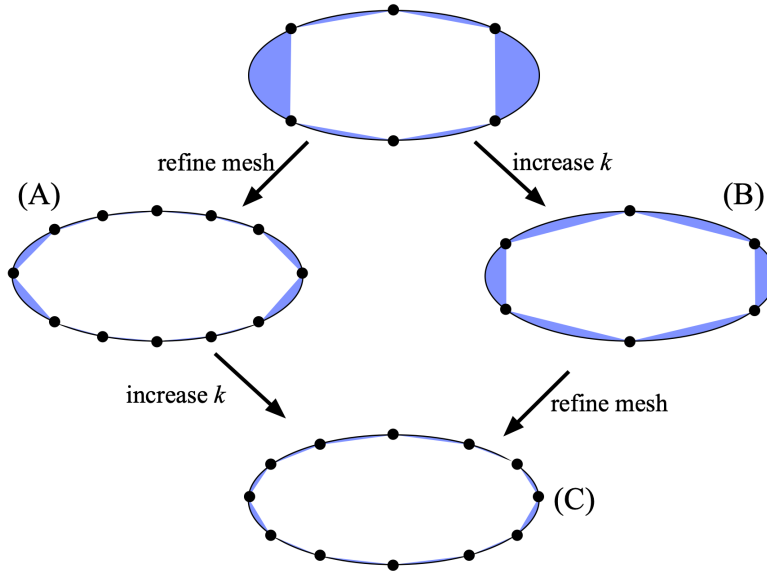


Figure 3.8: An ellipse is initially represented as six vertices connected by edges. The area between the approximation and actual ellipse is in blue. A) The mesh is refined, doubling the number of vertices used, but no position adjustments are made. B) The vertices are shifted by increasing k , but no new vertices are added. C) The mesh is refined and the vertices are shifted.

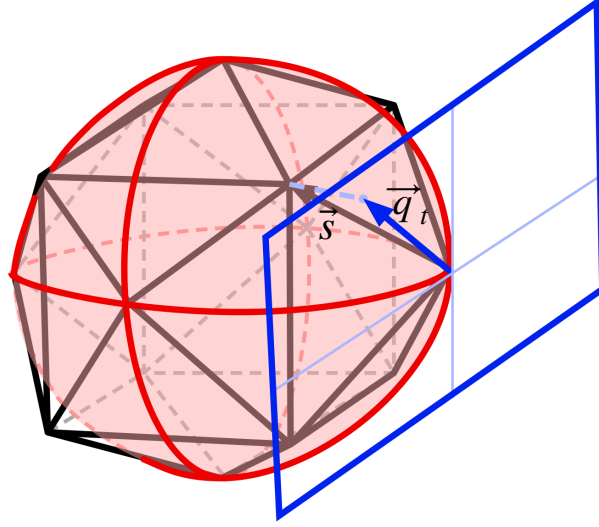


Figure 3.9: The curved volume, in red, is discretized into the black surface. The vector \vec{s} , in black, is projected onto the blue plane, which is tangent to the red surface at the tail of \vec{s} , creating the blue vector \vec{q}_t .

The closest approximation to the actual gap area is given by $k = 1$, and $k > 1$ has the effect of forcing vertices to distribute closer along high curvature sections of the boundary. It is also worth noting that the gap energy decreases quadratically as the total number of facets is increased, so gap energy does not contribute significantly to total energy for a sufficiently fine mesh.

Gap energy directly affects only the vertices at the head and tail of edges on the exterior facets. Let \vec{q}_h be the projection of \vec{s} onto the tangent plane of the constraint at the head vertex of s , as illustrated in Figure 3.8. For a vector \vec{s} with head vertex v_h and tail vertex v_t , we will write $\vec{w} \cdot \vec{w}$ as w^2 .

Thus,

$$\begin{aligned}\vec{F}_g(v_t) &= \frac{k\sqrt{(s^2 - q_t^2)} q_t^2}{2q_t^2} \vec{q}_t \\ \vec{F}_g(v_h) &= -\frac{k\sqrt{(s^2 - q_h^2)} q_h^2}{2q_h^2} \vec{q}_h\end{aligned}\tag{29}$$

and by combining the equations (21), (24), and (28) we obtain the discretized objective function

$$\Omega(b) = \sum_{i=1}^N p_c V + \sum_{j=1}^{n_i} \left(\frac{\gamma_c}{2} \|\vec{s}_{0,j} \times \vec{s}_{1,j}\| + \sum_{l=0}^2 \frac{k}{6} \|\vec{s}_l \times \vec{q}_l\| \right) \quad (30)$$

subject to $\frac{x^2}{r_x^2} + \frac{y^2}{r_y^2} = 1$ and the periodic boundary condition.

3.2.2. Semi-Flexible Sheath and Flexible Sheath Models

To apply a similar discretization to the semi-flexible sheath model, only a few changes to the rigid model are required. We now need to include the surface energy contributed by exterior facets, meaning our equation for energy from surface tension is now

$$\Omega(b) = \sum_{i=1}^N p_c V + \sum_{j=1}^{n_i} \left(T(f_j) \|\vec{s}_{0,j} \times \vec{s}_{1,j}\| + \sum_{l=0}^2 \frac{k}{6} \|\vec{s}_l \times \vec{q}_l\| \right) \quad (31)$$

Rather than carry the notation for a piecewise energy function through our objective function, we instead use

$$\Omega_t(f) = T(f) \|\vec{s}_l \times \vec{q}_l\| \quad (32)$$

where

$$T(f) = \begin{cases} 2\gamma_c & f \in \text{interior} \\ \gamma_c + \gamma_s & f \in \text{exterior} \end{cases} \quad (33)$$

Thus,

$$\Omega_t(f) = \begin{cases} \frac{2\gamma_c}{2} \|\vec{s}_0 \times \vec{s}_1\| & f \in \text{interior} \\ \frac{\gamma_s + \gamma_c}{2} \|\vec{s}_0 \times \vec{s}_1\| & f \in \text{exterior} \end{cases} \quad (34)$$

and we note that unlike in the rigid tube system, the geometric boundary constraint is dependent on cell configuration because r_x and r_y are dependent variables; volume remains constrained as before.

Only one change to the semi-flexible model is needed to create our flexible model. We have the same objective function as with the semi-flexible model and we continue to constrain

volume and require the periodic boundary condition. Unlike the semi-flexible model, those are the only constraints for this model.

3.3. Test Problems

We ran our simulations using Surface Evolver, a finite element program developed by Brakke [1] and used extensively in foam modeling [2-4, 13, 17, 18, 21, 24, 29, 35, 36]. To verify the accuracy of our Surface Evolver simulations, we created two test models for problems with analytical solutions. The first was designed to test the accuracy of the implementation of an infinitely long tube in Surface Evolver, and for simplicity this was done in two dimensions. The second test problem was created to verify the necessary mesh refinement for satisfactory energy convergence in three dimensions.

3.3.1. Two-Dimensional Analogue Problem

We begin by studying the analytical solution of a simpler version of the notochord problem with a rigid sheath. To translate our three-dimensional system to a two-dimensional system, our cell surfaces become curves or lines, and our volumes become areas; see Figure 3.10. The transition point between optimal patterns for this system can be found analytically.

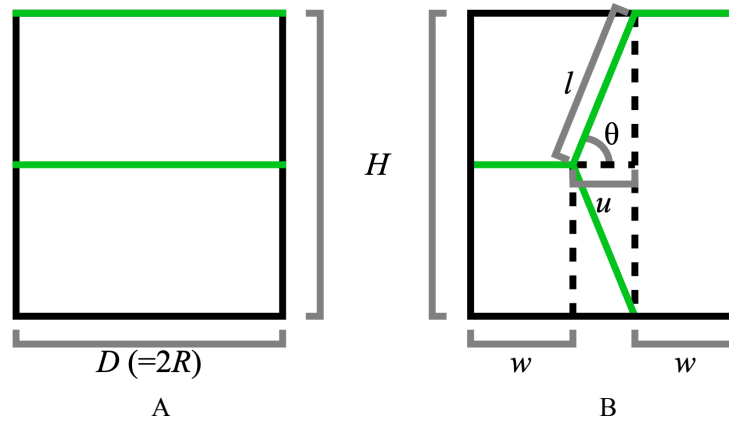


Figure 3.10: Two-dimensional potential fundamental regions in A) bamboo and B) staircase, which are each composed of two cells. The green edges are the ones that contribute to interfacial tension. The bottom edges are intentionally excluded to prevent counting edges twice when the pattern is repeated.

Consider two pairs of fundamental regions in the configurations shown in Figure 3.10 with the same cell-cell surface tension for each edge. Because the tension is identical, we see that the angles formed by the three green edges must be equal, so $\theta = \pi/3$, as first observed by Plateau [27].

If we let γ represent interfacial tension, then we can write the surface energy functions of bamboo and staircase patterns in the fundamental region, respectively, as

$$\begin{aligned}\Omega_b &= 2\gamma D \\ \Omega_s &= 2\gamma l + 2\gamma w\end{aligned}\tag{36}$$

Since the angle θ is part of a right triangle, we obtain

$$l = \sqrt{u^2 + (H/2)^2}\tag{37}$$

and we can further conclude that $D = u + 2w$, which implies that $u = 2w - 2R$ since our foam is completely space-filling. We are assuming that all cells have the same area, so from the bamboo pattern we can see that the area of a cell can be written as

$$a = DH/2 = RH\tag{38}$$

From the right triangle described by θ and l we have

$$\tan \theta = \frac{H/2}{u} = \frac{H/2}{2w - 2R}\tag{39}$$

and because $\theta = \pi/3$, solving this for w gives us $w = R - \frac{\sqrt{3}}{12}H$; solving the cell area equation

for H and substituting here yields $w = R - \frac{\sqrt{3}a}{12R}$ and our energy functions thus become

$$\begin{aligned}\Omega_b &= 4\gamma R \\ \Omega_s &= \frac{\gamma(4R^2 - \sqrt{3}a)}{2R}\end{aligned}\tag{40}$$

We now define λ in the two-dimensional context to be the ratio of tube diameter to diameter of a circle with area a ; i.e.,

$$\lambda = \frac{D}{d} = \frac{2R}{2\sqrt{a/\pi}} \quad (41)$$

By solving equation (41) for R and substituting the result into the energy functions from (36), we obtain

$$\begin{aligned} \Omega_b &= \gamma\sqrt{a} \frac{4\lambda}{\sqrt{\pi}} \\ \Omega_s &= \gamma\sqrt{a} \frac{\pi\sqrt{3} + 4\lambda^2}{2\lambda\sqrt{\pi}} \end{aligned} \quad (42)$$

Since λ is dimensionless and $\gamma\sqrt{a}$ has a fixed value, it is possible to create dimensionless objective functions

$$\begin{aligned} \hat{\Omega}_b &= \frac{\Omega_b}{\gamma\sqrt{a}} = \frac{4\lambda}{\sqrt{\pi}} \\ \hat{\Omega}_s &= \frac{\Omega_s}{\gamma\sqrt{a}} = \frac{\pi\sqrt{3} + 4\lambda^2}{2\lambda\sqrt{\pi}} \end{aligned} \quad (43)$$

To find the λ value at which the transition between optimal patterns occurs, we set $\hat{\Omega}_b = \hat{\Omega}_s$ and solve for λ , yielding

$$\lambda = \frac{1}{2}\sqrt{\pi\sqrt{3}} \approx 1.166 \quad (44)$$

Interestingly, if we solve $d\hat{\Omega}_s/d\lambda = 0$, we see that this is also the λ value for which Ω_s is minimized, and this λ value is also comparable to the λ value for the bamboo-staircase pattern transition observed in foam experiments; see Figure 3.2.

We now consider the simulated version of the above problem to test Surface Evolver's accuracy against a problem with a known analytical solution. We still need to examine an infinitely long “tube,” so we need to determine a fundamental region which we can then repeat

infinitely. This means we are using a periodic boundary condition $(x, 0) = (x, h)$, where h is the height of the fundamental region. We will refer to this boundary condition as the torus constraint.

In the interest of using Surface Evolver, we use the initial geometry shown in Figure 3.11, because it is easy to implement and has the maximum number of cells in contact with each other. If we create a graph using each cell as a vertex, and connecting adjacent cells with edges, then this geometry makes the valences of these vertices as large as possible, which allows patterns to transition into less complicated patterns.

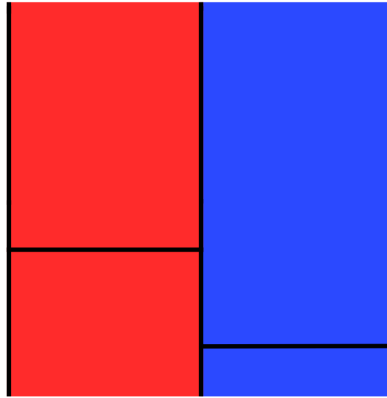


Figure 3.11: Initial fundamental region that is repeated infinitely in either direction. The red and blue each represent one cell.

First, we performed a mesh refinement study, and we found that the minimal energy solutions conformed to the analytical solution for all λ regardless of mesh. This happens because the bamboo and staircase solutions have only straight edges due to the boundary condition and required equal internal pressure for both cells.

We also wanted to verify that Surface Evolver accurately quantifies the transition point that is expected based on the previously discussed analytical solution. We found this to be the case, as shown in Figure 3.12, with our simulated points fitting precisely to the analytical solutions.

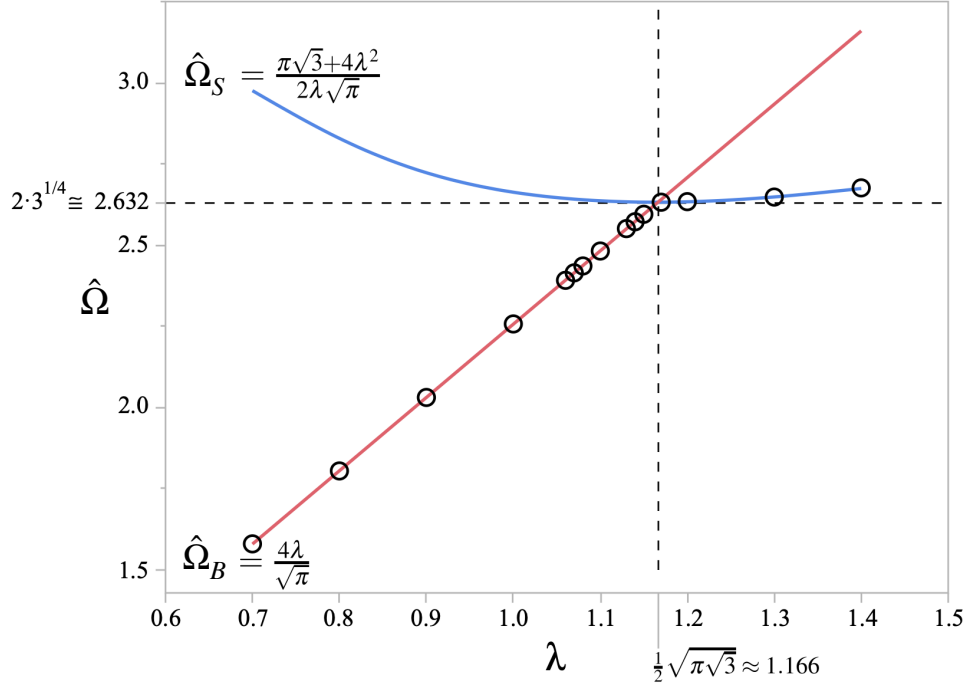


Figure 3.12: Nondimensional energy per unit volume in the bamboo configuration is shown in red, and the nondimensional energy per unit volume in the staircase configuration is shown in blue. The λ value where the computed staircase energy becomes lower than the projected bamboo configuration energy is approximately 1.17, which is comparable to the λ value from foam experiments, seen in Figure 3.1.

3.3.2. Two Bubbles

Our second test problem is designed primarily to test the 3-dimensional mesh capabilities and accuracy of Surface Evolver. We consider two bubbles with identical prescribed volume and surface tension, a problem which again has a known analytical solution. The initial geometry uses two cubes as approximations to spheres, as depicted in Figure 3.13. Because this is obviously a highly inaccurate representation of spheres, it provides a good way to study the effect of mesh coarseness on computed volume.

To assess the accuracy of the stable energy solution supplied by Surface Evolver, we compare our results to the analytical solution, which we derive as a consequence of the Laplace-Young equation [16, 39]

$$\Delta p = -\gamma \nabla \cdot \vec{n} \quad (45)$$

to describe the pressure difference across the interface between two static fluids, where γ is the surface tension, \vec{n} is the unit normal directed outward from the surface of the foam, and Δp is the Laplace pressure, defined as the pressure difference between internal foam pressure and, in our case, ambient pressure [37].

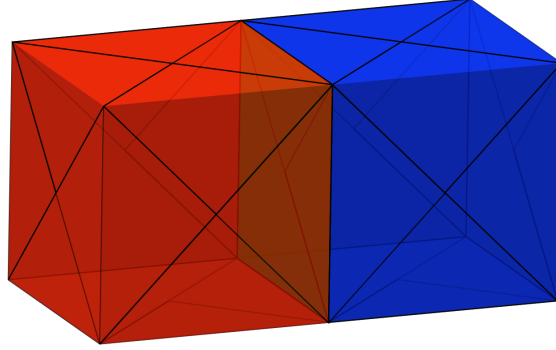


Figure 3.13: Initial geometry used to simulate the mechanics of two bubbles of equal volume.

It has been well-established, as in [14] for example, that the solution to the Laplace-Young equation is

$$p = 2\gamma H = \gamma \left(\frac{1}{R_1} + \frac{1}{R_2} \right) \quad (46)$$

where H is the mean curvature of the surface with radii of curvature R_1 and R_2 . In this case, the curvature is homogeneous on each individual surface, so this simplifies to

$$p = \frac{2\gamma}{r} \quad (47)$$

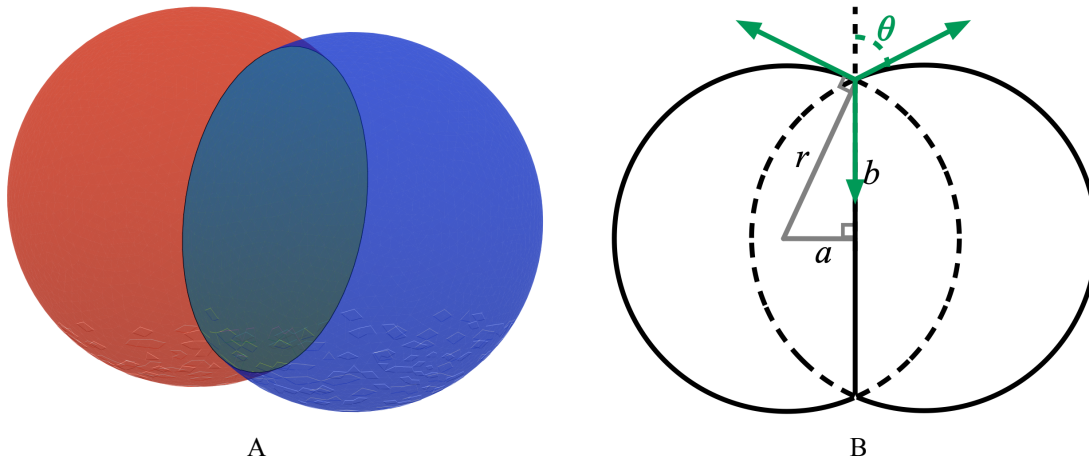
where r is the radius of curvature of the surface in question.

Since the two bubbles have equal internal pressure, the curvature of the interface between the two bubbles is

$$\kappa = \frac{2\gamma}{r_1} - \frac{2\gamma}{r_2} = \frac{2\gamma}{r} - \frac{2\gamma}{r} = 0 \quad (48)$$

and the shared interface is therefore flat.

Next we consider the system as a whole. Since we assume our configuration is stable, we know that the forces where the two bubbles meet and form the interface must be balanced. Because the two spheres are identical in volume and surface tension, together they have circular symmetry about the line perpendicular to the exterior and interior surfaces of both bubbles. Therefore, this problem can be simplified to balancing the forces of any cross section that contains a similar line of symmetry, as illustrated in 3.14. Because the bubbles are of equal volume, the angles formed by where they meet the interfacial foam must be equal. The surface tension is also the same for all surfaces, so the tangent vectors to each surface must be of equal magnitude. Thus, the angles of intersection are $2\pi/3$, and this is confirmed by the first of Plateau's laws [27].



3.14: Two bubbles of A) equal volume and surface tension, and B) an arbitrary intersection of the surfaces of two bubbles and the plane perpendicular to all bubble surfaces (right).

We can now simplify this problem as a model for two intersecting circles with a segment joining their points of intersection. Because the line from the center of a circle to its perimeter is perpendicular to the perimeter at the point where they intersect, we can further reason that the angle between this line and the interface must be $\pi/6$. Now, by examining only one bubble, we

can thus compute the radius of the interfacial side, denoted b and equivalent to half the intersecting segment in our two dimensional simplification, as

$$b = r \cos \frac{\pi}{6} = \frac{r\sqrt{3}}{2} \quad (49)$$

and this is confirmed by the Young-Dupré equation [8].

Note that, if we let a be the line from the center of the circle that is perpendicular to the chord b , we see that

$$a = r \cos \frac{\pi}{3} = \frac{r}{2} \quad (50)$$

We now can compute the area of the shared surface as

$$A_{shared} = \pi b^2 = \frac{3r^2\pi}{4} \quad (51)$$

Let us now examine the spherical cap created by the intersection of this interfacial surface and a sphere. The area and volume for the cap using our notation is

$$\begin{aligned} A_{cap} &= 2\pi r(r - a) = \pi r^2 \\ V_{cap} &= \frac{\pi(r - a)^2}{3}(2r + a) = \frac{5\pi r^3}{24} \end{aligned} \quad (52)$$

Therefore, recalling that the area and volume of a sphere are $4\pi r^2$ and $4\pi r^3/3$, we conclude that the surface area and volume of the two bubbles are

$$\begin{aligned} A &= 2A_{sphere} - 2A_{cap} + A_{shared} & V &= 2V_{sphere} - 2V_{cap} \\ &= \frac{27\pi r^2}{4} & &= \frac{9\pi r^3}{4} \end{aligned} \quad (53)$$

Since cell volume is fixed, we denote the volume of an individual cell as $v = V/2$ because the above equations are for the system of two cells. Then we can solve for r using the volume equation, resulting in

$$r = \sqrt[3]{\frac{8v}{9\pi}} \quad (54)$$

Substituting this into equation (53) yields the equation for surface area of two bubbles,

$$A = 3\sqrt[3]{9\pi v^2} \quad (55)$$

and thus we conclude that the total surface energy for the two bubble system is

$$\Omega = \gamma 3\sqrt[3]{9\pi v^2} \quad (56)$$

The nondimensional energy is therefore

$$\hat{\Omega} = \frac{\Omega}{\gamma v^{2/3}} = 3\sqrt[3]{9\pi} \approx 9.1394 \quad (57)$$

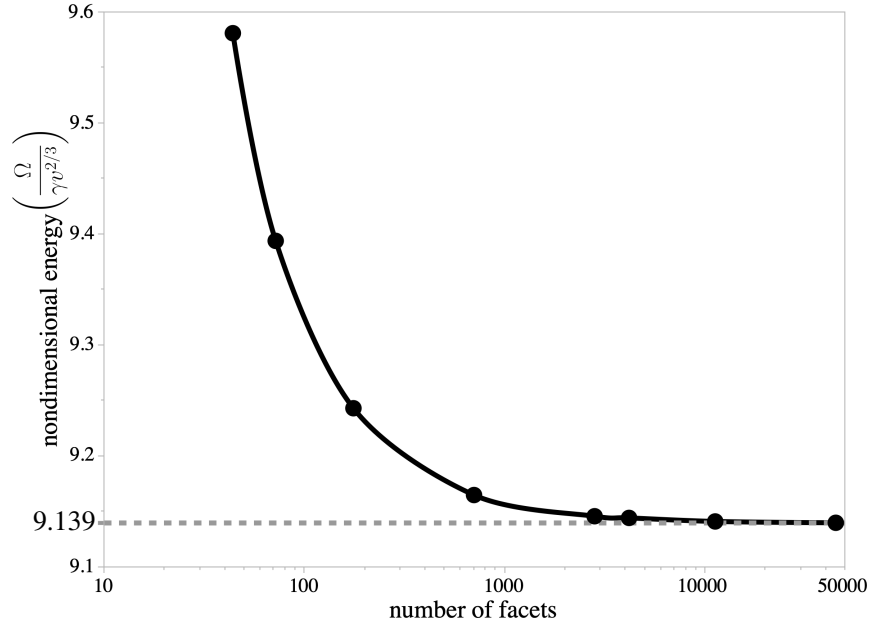


Figure 3.15: Simulated nondimensional energy, shown in black, is measured as a function of mesh fineness, as determined by number of facets used in the mesh; the cell volume is set to $v = 1$. After approximately 10,000 facets, the energy has converged to within 0.1 % of the analytical solution to this problem, which is $3\sqrt[3]{9\pi}$ and is indicated by the grey dashed line.

We performed a mesh refinement study, with the mesh rebalanced using equiangularization at each iteration. The rebalancing process is discussed in further detail in Section 3.4.3 of this chapter. We determined that for 3-dimensional simulations, using 11,000 facets converges to the analytical solution with relative error below 0.02 % , while 45,000 facets yields a relative error

below 0.005 % , as seen in Figure 3.15. When the increase in computing time between 11,000 and 45,000 facets is taken into account, we considered this decrease in computed energy to be insignificant. Since surface tension is fixed and equal across all surfaces, this is equivalent to showing that the increase has no effect on computed surface area. These results led us to our typical mesh of approximately 15,000 facets.

3.4. Model Implementation in Surface Evolver

A Surface Evolver datafile comprises three sections: definitions and options, geometry (further split into vertices, edges, faces, and bodies), and commands. The definitions and options section is where parameters, boundary constraints, and torus periodicity are defined.

Surface Evolver geometries are formed using a list of vertices in standard Cartesian coordinates by default, although it is possible to use other common systems or define one. The directed edges are then written as a list of pairs of vertices, where the tail is the first vertex of the pair. From this list of edges, we define faces; these are lists of edges in the order they connect. Because an edge e will not always point in the direction needed for specifying a face, we use $-e$ to indicate that this edge must be traversed in the opposite direction to make the appropriate connection. The direction of the edges around the face indicates the direction of the outward unit normal vector. Faces can also be assigned various physical properties, like surface tension, and visual properties, such as color or opacity. Lastly, the bodies are defined as a list of faces, where order is irrelevant. Surface Evolver bodies are the three-dimensional cells or bubbles to be modeled. When initializing a body, if a face f has a normal that points toward the interior of the body instead of the exterior, we use $-f$ instead.

The final section of a Surface Evolver datafile is the commands section. This section is optional, but can be used, for example, to prepare bodies for simulation or to create commands to be used later. It is also where the method for optimization is set; we have used the conjugate gradient method and incorporated simulated annealing. An example of a Surface Evolver datafile is presented in Appendix B.

3.4.1. Initial Geometry

Both the rigid and flexible tubes have the same initial geometry. Two triangular prisms are generated within a bounding elliptical tube of set eccentricity, as shown in Figure 3.15. All exterior faces of the prisms in Figure 3.16 are constrained to be on the bounding elliptical cylinder. Additionally, any edges of cell-cell surfaces that are shared with exterior faces are constrained to the bounding ellipse, and cell-cell surfaces themselves are constrained to be within the bounding elliptical cylinder.

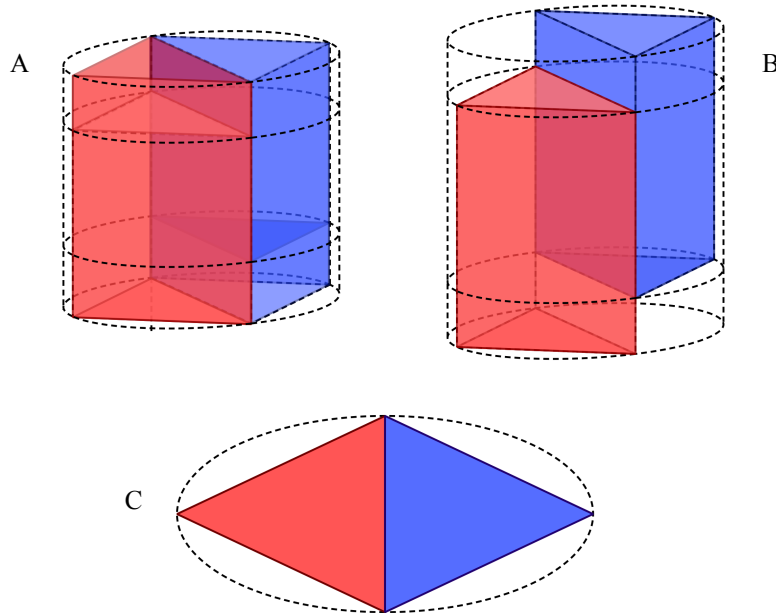


Figure 3.16: A) Initial fundamental region in three dimensions, B) Two full cells represented by the fundamental region, C) the fundamental region cross section; the shared edge of the triangles is also the minor axis of the bounding elliptical cylinder.

This allows interfacial surfaces to remain interior surfaces while keeping their connection to the sheath surfaces, preventing object inversion. The three-dimensional fundamental region has edges that wrap from above to underneath, equivalent to an infinite periodic tube of pairs of cells, as illustrated in Figure 3.16.

3.4.2. Boundary Conditions

We used the ellipse described by the equation

$$\frac{((x - \text{centerx})\cos\theta + (y - \text{centery})\sin\theta)^2}{(\text{radiusx}^2)} + \frac{((x - \text{centerx})\sin\theta - (y - \text{centery})\cos\theta)^2}{(\text{radiusy}^2)} = 1 \quad (58)$$

as our geometric boundary equation. The eccentricity and cross-sectional area parameters are used to compute the required `radiusx` and `radiusy`. The parameter θ rotates the bounding ellipse so its minor axis is correctly oriented in relation to the initial geometry. It is defined as

$$\theta = \arctan\left(\frac{\text{radiusy}}{\text{radiusx}}\right) + \frac{\pi}{2} \quad (59)$$

because Surface Evolver requires that a fundamental region with a periodic boundary constraint be contained completely in the first octant. We also define `centerx` and `centery` as $3/2 \text{ radiusx}$ and $3/2 \text{ radiusy}$ to ensure that the torus periodic vectors

$$\begin{aligned} &\langle 2\text{centerx}, 0, 0 \rangle \\ &\langle 0, 2\text{centery}, 0 \rangle \\ &\langle 0, 0, \text{initial_height} \rangle \end{aligned} \quad (60)$$

where `initial_height` is computed from λ and cross-sectional area, are large enough to prevent any surfaces from overflowing the boundaries of the fundamental region.

For the semi-flexible model, we use the same ellipse from equation (58) as that used for the rigid boundary, except we initially set eccentricity at zero. This choice for initial eccentricity contributes the least amount of bias from the sheath toward staircase pattern. Furthermore, rather than have `radiusx` and `radiusy` as fixed parameters, they are dependent variables. Since cross-sectional area remains a fixed parameter, this is equivalent to allowing eccentricity become a variable. We choose this method over simply freeing the eccentricity parameter because `radiusx` and `radiusy` are used directly in the boundary equation, so this saves us from needing to recompute them using eccentricity at each iteration step.

3.4.3. Iteration

We use a modified iteration step, which consists of equiangularization - edges of neighboring facets are swapped to minimize the deviation of facet angles from equiangular - followed by vertex position averaging to even out facet size, and then the application of one step of computed forces to each vertex using the conjugate gradient method. This is repeated until energy, defined as the sum of facet surface areas weighted by their associated tension, begins to oscillate, at which point we refine the mesh and return to repeating the iteration process; we stop this modified iteration once the mesh is sufficiently fine to prevent oscillation. During this process, if the cells have not shifted to the bamboo pattern by the time our mesh has approximately 5,000 facets, we introduce a modified version of the simulated annealing option included within Surface Evolver. The standard included simulated annealing method moves each vertex before the actual optimization step by

$$\Delta \vec{x} = g t L \tag{61}$$

where t is the annealing “temperature”, g is a random value from the standard Gaussian distribution, and L is a characteristic length. The combination of this vertex movement with a step of the conjugate gradient method allows Surface Evolver to determine whether the movement of the vertex resulted in a lower energy state. Our modification allows the user to specify an amount by which to increase the initial t if no transition between patterns occurs after a user-specified number of iterations, making the method closer to the traditional simulated annealing algorithm.

3.4.4. Convergence

Once energy has converged to $\Delta\hat{\Omega} \leq 10^{-3}$ using the above method, we repeatedly halve edges above a length determined at the beginning of the convergence phase by the distribution of all edge lengths, denoted l ; this length is slowly decreased until all edges are approximately the same length. This value for l is then used for the remainder of the convergence process. Once l is set, we begin a further modified iteration step, where the vertex positions are shifted by the computed forces 100 times, followed by equiangularization until no edges are swapped, and then halving the edges longer than l . This modified iteration step is repeated until energy has converged to $\Delta\hat{\Omega} \leq 10^{-5}$, at which point the Hessian for the energy is computed and solved for the minimum energy; the threshold for considering a value to be equivalent to zero is set to 10^{-7} . This provides additional accuracy with the energy computation.

3.5. Results

3.5.1. Rigid Sheath

Since the only analytical solution we are able to find in three dimensions is for the bamboo configuration, we will derive this solution and compare it to our simulation results.

First, recalling that the cross-sectional area is S and interfacial tension is γ_c , we note that the total minimizable surface energy of a cell in the bamboo pattern is $\Omega_B = 2S\gamma_c$. The nondimensional energy equation for the bamboo pattern is then

$$\hat{\Omega}_B = 2 \frac{S\gamma_c}{2v^{2/3}\gamma_c} = \frac{S}{v^{2/3}} \quad (62)$$

where v is the volume of a cell.

To reformulate this equation in terms of λ , the substitutions

$$v = \frac{4\pi}{3} \left(\frac{d}{2} \right)^3 \quad d = \frac{D}{\lambda} \quad D = 2\sqrt{\frac{S}{\pi}} \quad (63)$$

are applied to yield the solution for nondimensional bamboo energy per cell with respect to λ :

$$\hat{\Omega}_B(\lambda) = \lambda^2 \frac{\sqrt[3]{36\pi}}{4} \quad (64)$$

We highlight that this equation does not depend on any other parameters, notably eccentricity e .

We plotted the results of our bamboo simulations in Figure 3.17 along with the analytical solution $\hat{\Omega}_B(\lambda)$, fit the curve for the analytical solution as expected. There is an error margin of $< 1\%$, which can be explained by mesh coarseness. We considered this error to be small enough that the benefit of increased accuracy from further mesh refinement was outweighed by the increased computational cost; the computational time a simulation with this mesh is roughly fifteen minutes, while a simulation with one additional refinement of the mesh resulted in a run time of several hours.

Our remaining discussion in this subsection focuses on the results of simulations in staircase pattern. We fit quadratic curves $p_e(\lambda)$ to the simulated staircase energies for each eccentricity e we tested, and found these fits to be sufficient for interpolating the bamboo-staircase intersection. A summary of our fit analysis is available in Appendix A.

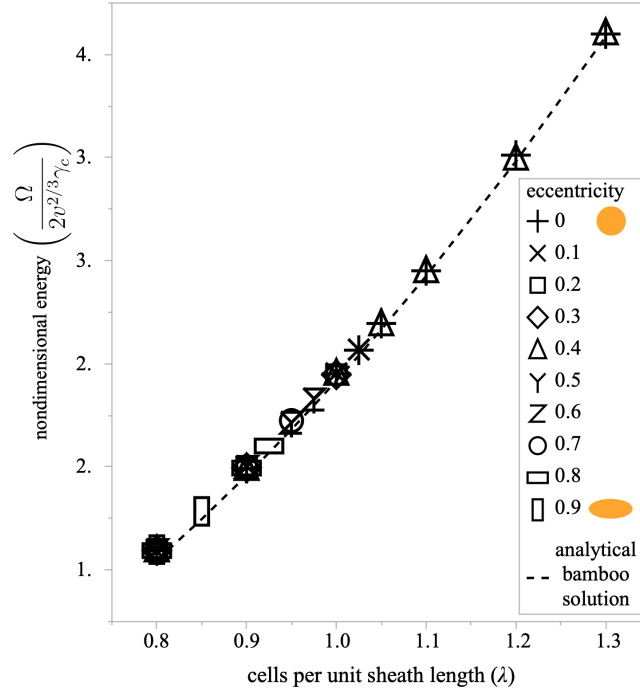


Figure 3.17: Simulated energy of a cell in bamboo pattern for the rigid sheath model. The simulated energy agreed with the analytical solution for the system. Like the analytical solution, the simulated nondimensional energy is independent of eccentricity and varies solely with λ .

We now define $\lambda_{BS}(e)$ as the λ value where the analytical bamboo solution intersects our interpolated staircase energy, and it is dependent on cylinder eccentricity; $\lambda_{BS}(e)$ is then computed by solving $p_e(\lambda) = \hat{\Omega}_B(\lambda)$ for each eccentricity.

Our minimal energy simulations allowed cells to transition from staircase to bamboo pattern, and we observed the λ values where this transition occurred. Due the topology change required to move from a pattern characterized by a cell-cell connection graph with low valence vertices to a more complex one, we are unable to simulate cells transitioning from bamboo to staircase.

We hypothesized that the bamboo pattern would be the pattern to which cells converged for $\lambda < \lambda_{BS}(e)$. However, we found that in simulations cells continue to converge to the staircase pattern for a range of λ below $\lambda_{BS}(e)$, as shown in Figure 3.18, and this range is dependent on

eccentricity. This overlap of ranges where patterns can be observed agrees with results from foam experiments on circular cylinders, like those in [26].

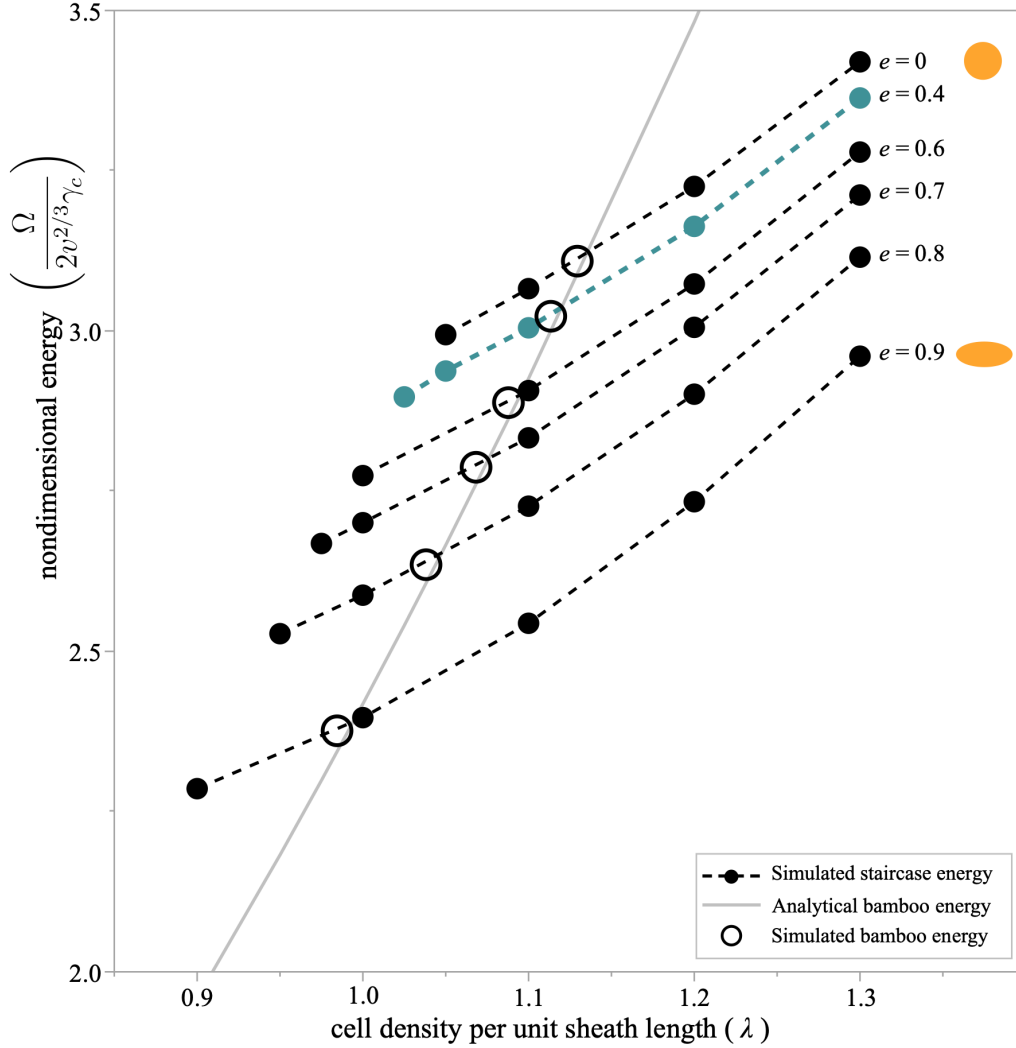


Figure 3.18: Minimized energy for staircase simulations (dashed lines), by λ and e , compared with analytical energy for bamboo (grey solid line). The simulations with eccentricity of relevance to the notochord are colored in teal. There is overlap between where staircase pattern is observed and where bamboo pattern is optimal. Nondimensional energy for cells in the staircase pattern decreases for fixed λ when eccentricity is increased, and this relationship between eccentricity and energy is nonlinear as particularly evidenced by the spacing between $e = 0.6$ through $e = 0.9$.

Therefore we denote the lowest observed lowest λ where staircase appears as $\lambda_{min}(e)$.

Increasing eccentricity increases both $\lambda_{min}(e)$ and $\lambda_{BS}(e)$, but $\lambda_{BS}(e) - \lambda_{min}(e)$ remains

approximately the same regardless of eccentricity. The effect of varying eccentricity on λ_{BS} is illustrated in Figure 3.19. From these simulations, we conclude that for the rigid tube, increasing eccentricity of the bounding tube biases its cells toward the staircase pattern.

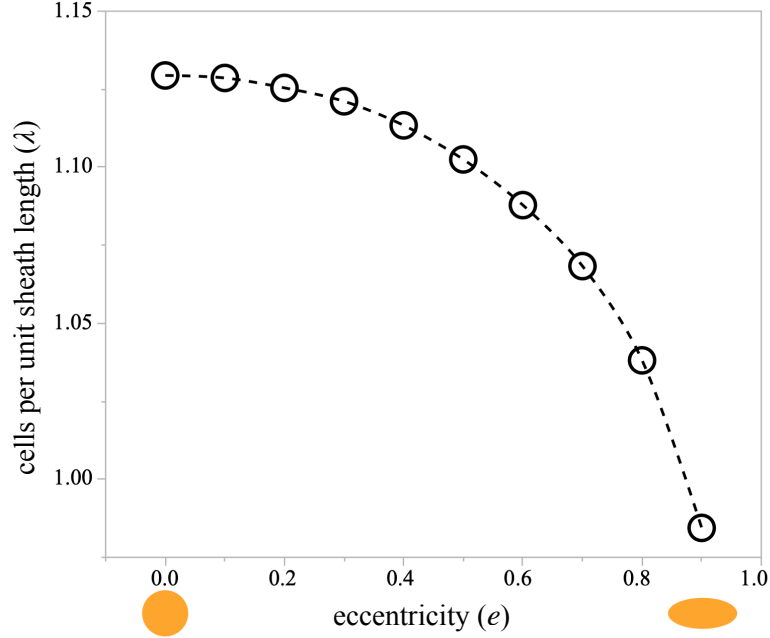


Figure 3.19: Circles represent λ_{BS} values for varying eccentricity. There is a strong relationship between tube eccentricity and the λ value at which the minimal energy pattern changes from bamboo to staircase.

3.5.2. Semi-flexible Sheath

Like the rigid tube, the cell arrangements of the semi-flexible tube depend on initial geometry; unlike the rigid tube where the geometry of the bounding cylinder is fixed, the semi-flexible tube has bounding geometry that is a result of the energy minimization. This results from the additional parameter in the semi-flexible model, the ratio of sheath surface tension to interfacial tension, which we previously defined as $\Gamma = \gamma_s/\gamma_c$.

We first observed that there were some values of λ for which a change in Γ has no effect on pattern. For $\lambda < 1$, all simulations converged to the bamboo pattern regardless of Γ value; conversely, for $\lambda > 1.1$ all simulations converged to the staircase pattern; see Figure 3.20. In the $1 \leq \lambda \leq 1.1$ range, Γ determines the observed pattern.

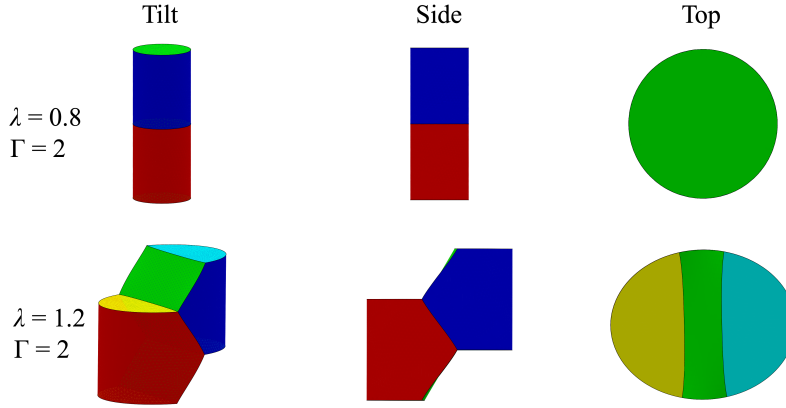


Figure 3.20: Example of simulated bamboo pattern (top) and staircase pattern (bottom). The Γ values are the same for both, but the different λ values result in different patterns.

For bamboo, observed eccentricity was not distinguishable from zero. For staircase, higher Γ decreased the eccentricity of the semi-flexible tube, as seen in Figure 3.21 (a). Our results indicate that increasing λ controls the bifurcation between the low eccentricity bamboo pattern and the higher eccentricity staircase pattern, but increasing Γ determines what values “low” and “high” eccentricity actually take; see Figure 3.21 (b).

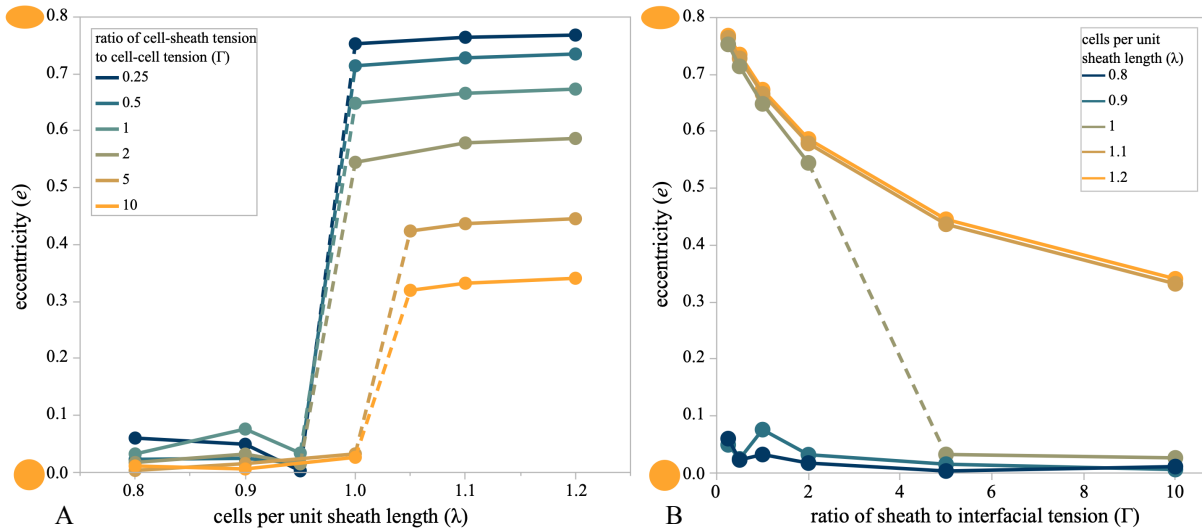


Figure 3.21: A) Effect of λ on eccentricity $e(\lambda, \Gamma)$ for different Γ values in the semi-flexible sheath model. For all Γ values tested, higher eccentricity is associated with higher λ and lower eccentricity is associated with lower λ . B) Effect of Γ on eccentricity $e(\lambda, \Gamma)$ for different λ values in the semi-flexible sheath model. For higher λ , decreasing Γ decreases the difference between high and low eccentricity. For $\lambda = 1$, varying Γ causes eccentricity to jump from high to low (as a result of pattern change).

3.5.3. Fully Flexible Sheath

The fully flexible sheath model is the least constrained of the three models, and it is also the richest in novel results. Our first observation is that Γ changes the shape of cells in all patterns. Simulations with low Γ showed much higher curvature than those with high Γ . These variations in cell shape can be observed for bamboo and staircase patterns in Figure 3.22.

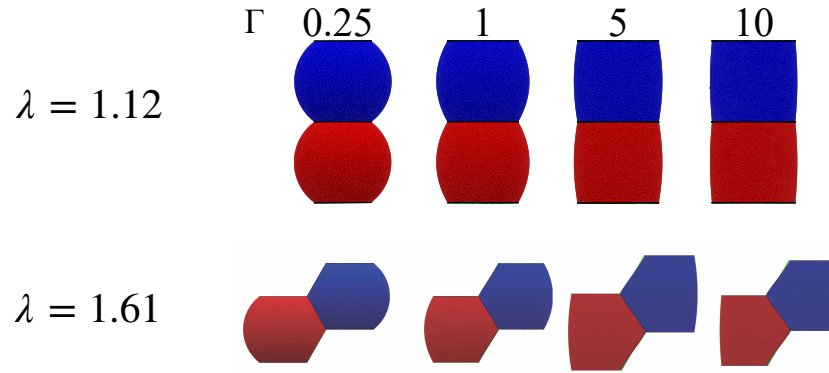


Figure 3.22: Optimal packing in the fundamental region for different Γ with $\lambda = 1.12$ and $\lambda = 1.61$. Increasing Γ causes the curvature of the sheath to decrease.

An alternative interpretation is that Γ controls the angle between cells, which we define as the angle created by the intersection of the sheath surfaces of two cells with a plane perpendicular to both surfaces; see Figure 3.23. This definition is effectively a localization of the angle measurement used for the two bubble test problem in Section 3.3.2 of this chapter, and it too can be expressed analytically. Of note, this definition allows us to examine the angle between cells in patterns other than ones where the cell-cell interface is flat.

To find the angle between two exterior cell surfaces, we again examine a cross section on the plane perpendicular to both surfaces, as we did in our two bubble test problem. However, in this case, the tension on all surfaces is not equal, as illustrated in Figure 3.23, and our force-balance changes accordingly.

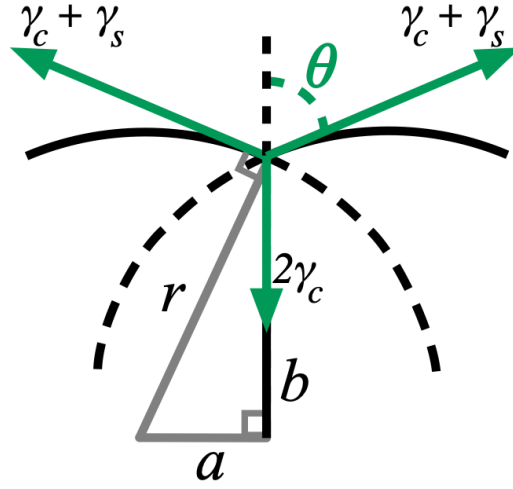


Figure 3.23: Generalization of 3.14, with surface tensions allowed to be unequal. The solution is an extension of Plateau's laws, the Young-Dupré equation [7].

We now require

$$\cos \theta = \frac{\gamma_c}{\gamma_c + \gamma_s} \quad (65)$$

for the forces acting on the intersection of the cell-cell surface and the cell-sheath surfaces from each cell on the plane perpendicular to all three surfaces at that point. We see that

$$\lim_{\gamma_s \rightarrow \infty} \arccos \frac{\gamma_c}{\gamma_c + \gamma_s} = \frac{\pi}{2} \quad (66)$$

so as γ_s approaches infinity, meaning that Γ approaches infinity, we have cell-sheath surfaces that are perpendicular to the cell-cell surface and parallel to each other. At this limit, we would see a sheath surface that is differentiable everywhere, and this is similar to the semi-flexible boundary condition.

Because the flexible sheath is not geometrically constrained, there is no way to discuss the precise eccentricity of the equilibrium solutions. Instead, we define the eccentricity \tilde{e} of a configuration as the eccentricity of the best fit ellipse for the perimeter of the projection of all vertices onto the xy plane. The eccentricity \tilde{e} is computed in MATLAB from the ellipse with

major and minor axes that have the same normalized central moments as the region formed by the projection perimeter. Note that for the rigid and semi-rigid models with eccentricity e , $\tilde{e} = e$.

There are similar behaviors between the semi-flexible sheath eccentricity e and flexible sheath eccentricity \tilde{e} . The curves in Figure 3.24 (a) have the same overall shape as the curves in Figure 3.21 (a), although the λ ranges are different. The fully flexible sheath model is much less constrained than the semi-flexible sheath models, and the properties of the flexible sheath result in a smoother transition between high and low eccentricity, as compared to the sharp transition seen for the semi-flexible model.

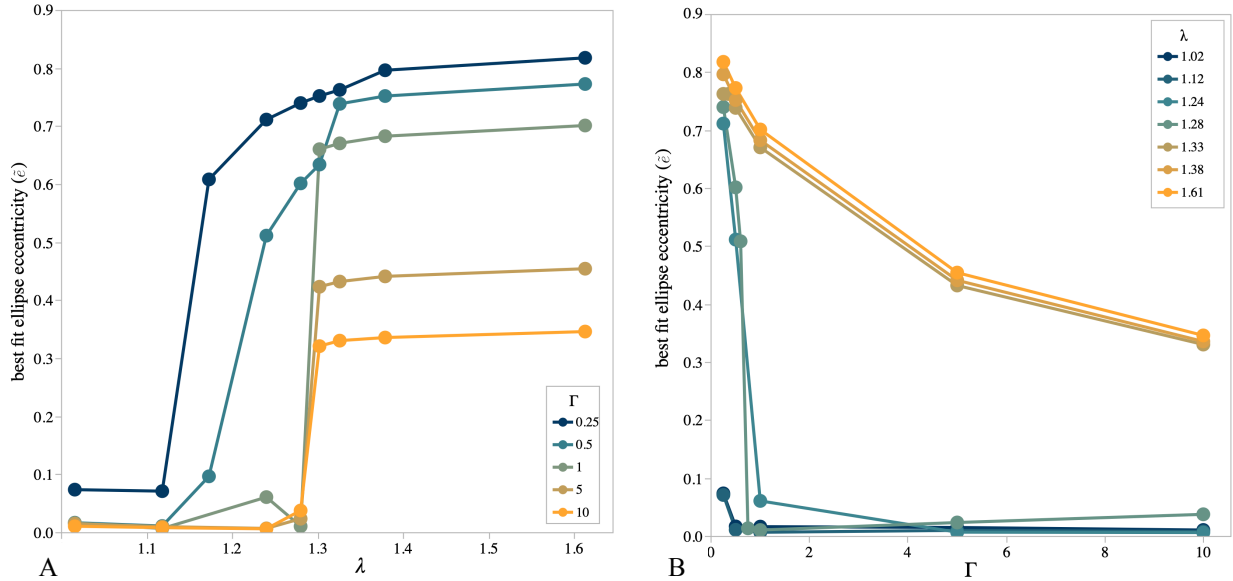


Figure 3.24: A) The relationship between λ and eccentricity \tilde{e} for different Γ values. Increasing λ generally causes an increase in \tilde{e} , but this is especially noticeable once $\tilde{e} > 0.1$. B) The relationship between Γ and eccentricity \tilde{e} for different λ values. Compared to the results of the semi-flexible sheath, there are more values of λ that exhibit high \tilde{e} for low Γ , and they do not follow the curve formed by the simulations of the lowest λ values.

There is a notable similarity between Figure 3.21 (b) and Figure 3.24 (b); however, the drop between high and low eccentricity is much sharper for the flexible sheath. This is due to the higher number of simulations run near the bifurcation point for this model. As with λ , the Γ

values differ between the semi-flexible and flexible models, but the overall trend in the relationships between λ and eccentricity and between Γ and eccentricity are remarkably similar. The difference between the semi-flexible sheath results and the flexible sheath results likely stems from a unique phenomenon exhibited by the flexible sheath model.

Our surprising discovery with the flexible sheath model is the existence of a unique pattern not seen in either the rigid or semi-flexible models, which we have named the serpentine pattern; it is shown in the boxed portion of Figure 3.25. This pattern shares properties with both

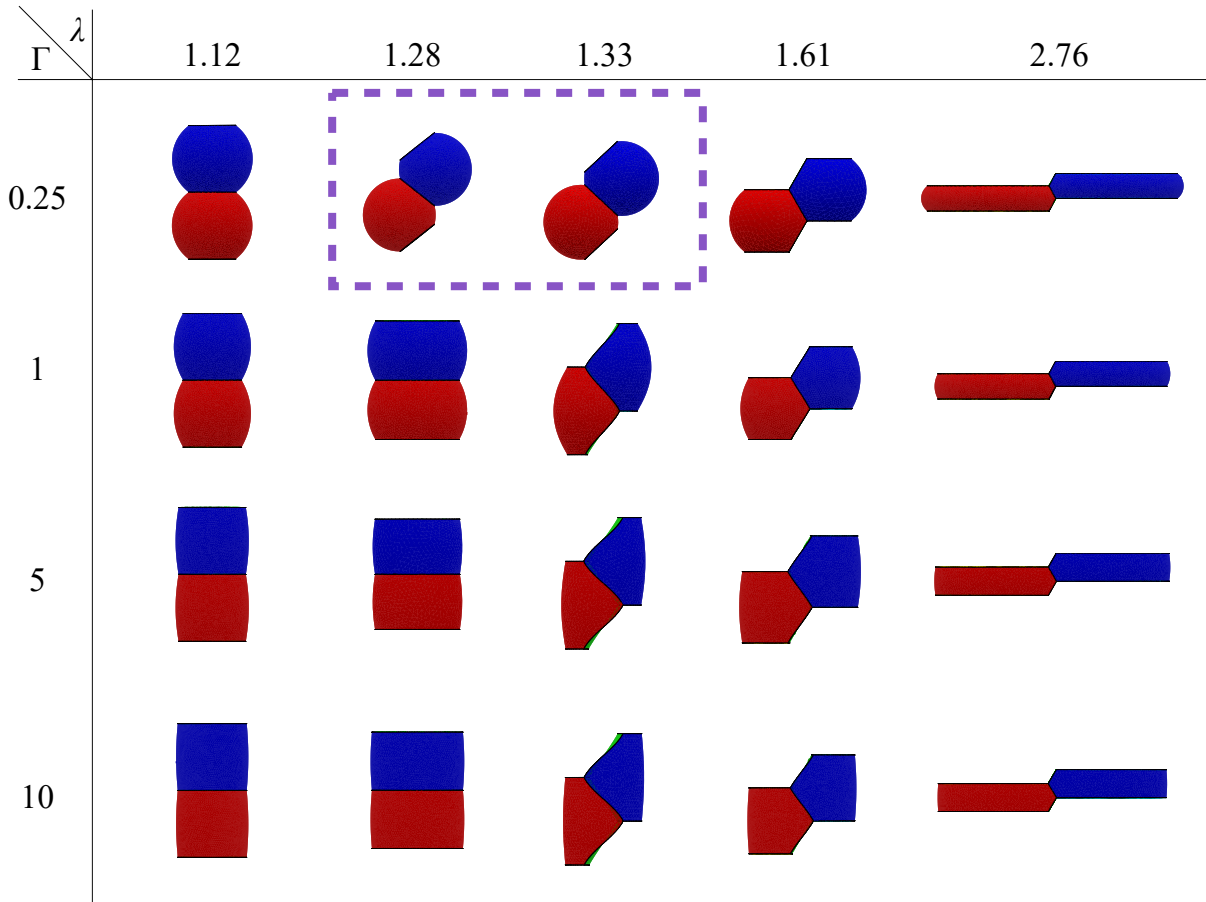


Figure 3.25: Optimal packing in the fundamental region for combinations of λ and Γ . Increasing Γ causes the curvature of the sheath to decrease, while varying λ causes the pattern of the cells to change.

the bamboo and staircase patterns, but cannot be completely described by either of the previously observed patterns.

The serpentine pattern is characterized by a cell connection graph with vertices of valence ≤ 2 , like the connection graph for the bamboo pattern. Although cells in the serpentine pattern have the same connection graph as bamboo, their centroid positions are staggered like those of cells in the staircase pattern. We detect serpentine pattern by a disagreement between the result of connection sorting and that of the sorting algorithm described in Chapter 2.

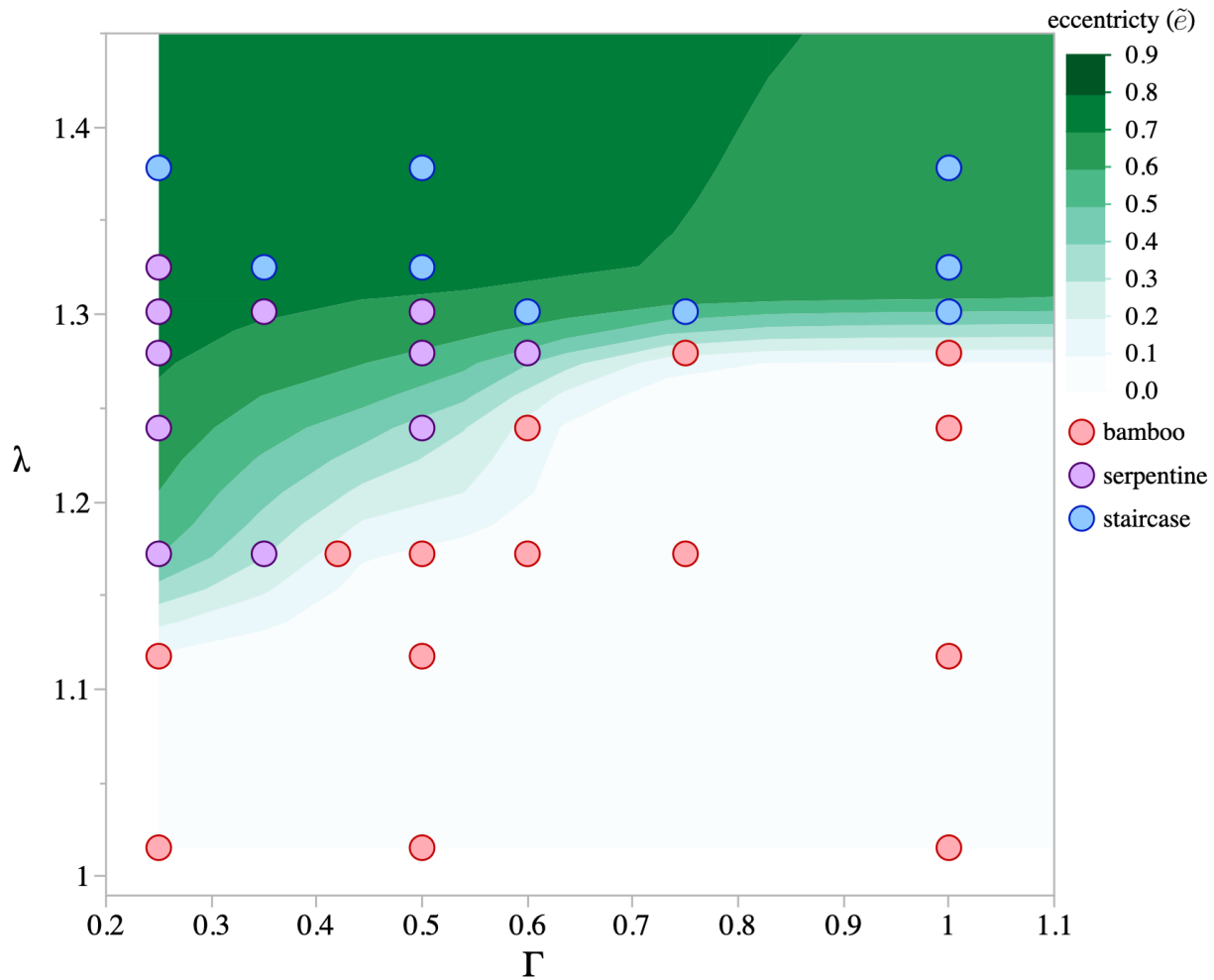


Figure 3.25: Relationship between eccentricity, pattern, λ , and Γ . Bamboo consistently has eccentricity near zero, and both serpentine and staircase present with high eccentricity. There is an additional bifurcation in patterns associated with $\Gamma < 0.6$ and $1.17 < \lambda < 1.33$ that does not appear for the rigid or semi-flexible models, which do not exhibit the serpentine pattern.

We only observed the existence of the serpentine pattern for a particular range of Γ and λ , where $\Gamma < 0.6$ and $1.17 < \lambda < 1.33$, as shown in Figure 3.26. Further simulations will be required to determine this range with more accuracy. However, we determined that there is a bifurcation for minimal energy pattern outside of the potential serpentine range. For $\Gamma \geq 0.75$, bamboo is always the only observed pattern if $\lambda < 1.12$ and staircase is always the only observed pattern for $\lambda > 1.61$. Although there is no correlation between Γ and pattern for Γ outside of the serpentine range, the curvature of the cell surface in contact with the sheath is controlled primarily by Γ ; this is clear from a visual examination of surfaces, as presented in Figure 3.25.

Chapter 4

Conclusion

4.1. Discussion

The experiments with zebrafish notochords and the associated physical gel bead model suggest that the arrangement of interior vacuolated notochord cells does behave like a packing problem. The diameter of the notochord of WT zebrafish relative to size of vacuolated cells limits the potential stable patterns to the bamboo, staircase, first chiral, and hopscotch patterns. We were able to create a pattern sorting algorithm based solely on centroid position, and it has been shown to be effective for categorizing the irregular cells of the WT zebrafish notochord into phyllotactic patterns. No such algorithm has been implemented in the previous study of foams.

We developed two complementary pattern-detection algorithms, one based on centroid radial position and one based on the vectors between nearby centroids. Although it could be effective for ordered monodisperse foams, a pattern detection algorithm based on centroid radial distance is insufficient to fully categorize all cells in the notochord; an algorithm that captures relative position between centroids shows greatly improved accuracy. This is because, unlike ordered monodisperse foams, the notochord has irregular patterns and transitions between patterns frequently, and a radial distance-based algorithm is unable to detect these.

We also created three models of constrained monodisperse foams. These models, one of a rigid elliptical sheath, one of an elliptical sheath with varying eccentricity, and one with a sheath constrained only by surface tension rather than geometry, were used to study foam packing in tubes.

The rigid sheath model, although not directly related to the mechanics of the notochord, could be applied in the relatively new field of discrete microfluidics to further expand the known interaction between tube geometry and foam structures, since this interaction is used in discrete microfluidics to efficiently process very small amounts of gases and liquids [7]. The results of the rigid sheath model show that sheath eccentricity affects equilibrium cell pattern. Tubes with nonzero eccentricity bifurcate to the staircase pattern at lower cell densities, and this shift becomes stronger as eccentricity is increased.

The semi-flexible sheath model provides a potential metric to measure the tension of the notochord sheath relative to the tension of the inner vacuolated cells. We have found a strong relationship between cell volume relative to tube volume, cell-sheath surface tension relative to cell-cell surface tension, and sheath eccentricity. Because sheath volume, number of cells (and therefore cell volume), and sheath eccentricity are computable from easily obtained and minimally invasive notochord measurements, this gives the semi-flexible sheath metric additional value for *in vivo* notochord experiments. Furthermore, the results from the semi-flexible sheath model combined with the results from the rigid model confirm that sheath eccentricity and equilibrium pattern are interdependent, as we observed in the physical model and zebrafish notochord in [23]. Although the notochord sheath is not constrained to form an elliptical cross section, the semi-flexible model provides a reasonable approximation to the true sheath geometry. It is possible that the notochord evolution specifically took advantage of the mechanical interaction between cell packing and tube shape, since the notochord's mechanics are thus far not observed in other biological systems.

Like the rigid model, the fully flexible model is not entirely relevant to the behavior of the notochord. The flexible sheath model's behavior for low Γ does not resemble that of the notochord at all, although for high Γ , the observed equilibrium configurations resemble that of the notochord. The physiological control of the physical properties of the notochord, such as whether cell size or cell pressure is being controlled, are unknown, and the curvatures and rigidity of the sheath are difficult to measure precisely in zebrafish experiments, so the accuracy of the flexible sheath model as an effective model for the notochord is uncertain. Despite the difficulty in assessing its viability as a mechanical notochord model, the unique mechanics of the flexible sheath model yield unexpected physical results in the form of the previously unobserved serpentine pattern.

What makes serpentine a particularly interesting and unique pattern is that not only has it been observed only in the flexible sheath model, it is actually impossible for it to appear in either the rigid or semi-flexible models. The cell-sheath surface topology of the serpentine pattern requires that the graph formed by cell-cell connections have vertices with valence ≤ 2 . Because the rigid and semi-flexible models both require the cells to be completely space filling, the two cell-cell surfaces would have to be perpendicular to the sheath, and therefore parallel to each other, as a consequence of Plateau's laws; serpentine pattern requires the interfacial surfaces between cells to be non-parallel to achieve its staggered centroid positioning.

4.2. Future Work

We have shown that the complex process of notochord morphogenesis can be reasonably approximated by a purely mechanical model based on those of foams in tubes. We suggest further exploration of the semi-flexible and fully flexible models in particular.

The extension of the semi-flexible model, constrained cross sectionally by an ellipse with variable eccentricity, to a model constrained by only fixed perimeter of the cross section will allow an in-depth exploration of the potential geometry of the notochord sheath formed by inner vacuolated cell packing. These results could be used to create an even closer mechanical model approximation to the actual physics of the notochord. Aside from potential applications for biological system analysis, this model could additionally be used in the energy minimization problem of optimal tube geometry for constrained foams, a problem which has yet to be explored.

Additional application of the projection algorithm to foam pattern categorization will allow its accuracy to be quantified, and additional modifications to the algorithm could be made to increase the variety of patterns identified. This would involve a detailed study of the periodicities of more complex constrained foam patterns based on their centroid positioning, rather than the current periodicity assessment based on the pattern of the bubbles formed by their contact with the bounding tube, which could be achieved with further study of our mechanical foam models.

The packings that appear in the flexible model strongly resemble those of other biological systems, such as the arrangement formed by cells during oogenesis in *Drosophila*. Further analysis of the fully flexible scheme has the potential to yield a physical model for this process as well, although that is beyond the scope of this work.

References

1. Brakke, K.A., The Surface Evolver. *Experiment. Math.*, 1992. 1(2): p. 141-165.
2. Brakke, K.A., The Surface Evolver and the Stability of Liquid Surfaces. *Philosophical Transactions of the Royal Society of London. Series A: Mathematical, Physical and Engineering Sciences*, 1996. 354(1715): p. 2143-2157.
3. Brakke, K.A. and Sullivan, J.M., Using Symmetry Features of the Surface Evolver to Study Foams, *Visualization and Mathematics: Experiments, Simulations and Environments*, H.-C. Hege and K. Polthier, Editors. 1997, Springer Berlin Heidelberg: Berlin, Heidelberg. p. 95-117.
4. Collicott, S.H. and Weislogel, M.M., Computing Existence and Stability of Capillary Surfaces Using Surface Evolver. *AIAA Journal*, 2004. 42(2): p. 289-295.
5. Costes, S.V., Daelemans, D., Cho, E.H., Dobbin, Z., Pavlakis, G., and Lockett, S., Automatic and Quantitative Measurement of Protein-Protein Colocalization in Live Cells. *Biophysical Journal*, 2004. 86(6): p. 3993-4003.
6. Drenckhan, W., Cox, S.J., Delaney, G., Holste, H., Weaire, D., and Kern, N., Rheology of Ordered Foams—on the Way to Discrete Microfluidics. *Colloids and Surfaces A: Physicochemical and Engineering Aspects*, 2005. 263(1): p. 52-64.
7. Dupré, A. and Dupré, P., Théorie Mécanique De La Chaleur. *Landmarks of Science*. Monographs. 1869: Gauthier-Villars.
8. Ellis, K., Bagwell, J., and Bagnat, M., Notochord Vacuoles Are Lysosome-Related Organelles That Function in Axis and Spine Morphogenesis. *The Journal of Cell Biology*, 2013. 200(5): p. 667-679.

9. Ellis, K., Hoffman, B.D., and Bagnat, M., The Vacuole Within: How Cellular Organization Dictates Notochord Function. *Bioarchitecture*, 2013. 3(3): p. 64-68.
10. Hutzler, S., Barry, J., Grasland-Mongrain, P., Smyth, D., and Weaire, D., Ordered Packings of Bubbles in Columns of Square Cross-Section. *Colloids and Surfaces A: Physicochemical and Engineering Aspects*, 2009. 344(1): p. 37-41.
11. Hutzler, S., Barry, J., Grasland-Mongrain, P., Smyth, D., and Weaire, D., Ordered Packings of Bubbles in Columns of Square Cross-Section. *Colloids and Surfaces A: Physicochemical and Engineering Aspects*, 2009. 344(1-3): p. 37-41.
12. Hutzler, S., Weaire, D., and Crawford, R., Moving Boundaries in Ordered Cylindrical Foam Structures. *Philosophical Magazine B*, 1997. 75(6): p. 845-857.
13. Isenberg, C., *The Science of Soap Films and Soap Bubbles*. Dover Books Explaining Science. 1992: Dover Publications.
14. Koehl, M.A.R., Quillin, K.J., and Pell, C.A., Mechanical Design of Fiber-Wound Hydraulic Skeletons: The Stiffening and Straightening of Embryonic Notochords. *American Zoologist*, 2000. 40(1): p. 28-041.
15. de Laplace, P.S., Supplément Au Dixième Livre Du Traité De Mécanique Céleste. *Traité De Mécanique Céleste. Vol. 1*. 1805: Chez J.B.M. Duprat.
16. Li, F., Zhang, C., Brakke, K.A., and Lei, Z., Computation of Equilibrium Bilayer Monodisperse Foam Structures Using the Surface Evolver. *Scientific Reports*, 2017. 7(1): p. 6131.
17. Mancini, M., Guène, E.M., Lambert, J., and Delannay, R., Using Surface Evolver to Measure Pressures and Energies of Real 2d Foams Submitted to Quasi-Static

- Deformations. *Colloids and Surfaces A: Physicochemical and Engineering Aspects*, 2015. 468: p. 193-200.
18. Mughal, A., Chan, H.K., and Weaire, D., Phyllotactic Description of Hard Sphere Packing in Cylindrical Channels. *Phys Rev Lett*, 2011. 106(11): p. 115704.
 19. Mughal, A., Chan, H.K., Weaire, D., and Hutzler, S., Dense Packings of Spheres in Cylinders: Simulations. *Phys Rev E Stat Nonlin Soft Matter Phys*, 2012. 85(5 Pt 1): p. 051305.
 20. Mughal, A., Libertiny, T., and Schröder-Turk, G.E., How Bees and Foams Respond to Curved Confinement: Level Set Boundary Representations in the Surface Evolver. *Colloids and Surfaces A: Physicochemical and Engineering Aspects*, 2017. 534: p. 94-104.
 21. Munro, E.M. and Odell, G.M., Polarized Basolateral Cell Motility Underlies Invagination and Convergent Extension of the Ascidian Notochord. *Development*, 2002. 129(1): p. 13.
 22. Norman, J., Sorrell, E.L., Hu, Y., Siripurapu, V., Garcia, J., Bagwell, J., Charbonneau, P., Lubkin, S.R., and Bagnat, M., Tissue Self-Organization Underlies Morphogenesis of the Notochord. *Philos Trans R Soc Lond B Biol Sci*, 2018. 373(1759).
 23. Phelan, R., Weaire, D., and Brakke, K., Computation of Equilibrium Foam Structures Using the Surface Evolver. *Experimental Mathematics*, 1995. 4(3): p. 181-192.
 24. Pittet, N., Boltenhagen, P., Rivier, N., and Weaire, D., Structural Transitions in Ordered, Cylindrical Foams. *Europhysics Letters (EPL)*, 1996. 35(7): p. 547-552.
 25. Pittet, N., Rivier, N., and Weaire, D., Cylindrical Packing of Foam Cells. *Forma*, 1995. 10(1): p. 65-73.

26. Plateau, J.A.F., Statique Expérimentale Et Théorique Des Liquides Soumis Aux Seules Forces Moléculaires. *Nature*. 1873, Paris: Gauthier-Villars.
27. Prusinkiewicz, P., Hanan, J.S., Fracchia, F.D., Lindenmayer, A., Fowler, D.R., de Boer, M.J.M., and Mercer, L., *The Algorithmic Beauty of Plants*. The Virtual Laboratory. 2012: Springer New York.
28. Reinelt, D., Boltenhagen, P., and Rivier, N., Deformed Foam Structure and Transitions in a Tube. *The European Physical Journal E*, 2001. 4(3): p. 299-304.
29. Saadatfar, M., Barry, J., Weaire, D., and Hutzler, S., Ordered Cylindrical Foam Structures with Internal Bubbles. *Philosophical Magazine Letters*, 2008. 88(9-10): p. 661-668.
30. Satoh, N., *Chordate Origins and Evolution: The Molecular Evolutionary Road to Vertebrates*. 2016: Elsevier Science.
31. Stemple, D.L., Structure and Function of the Notochord: An Essential Organ for Chordate Development. *Development*, 2005. 132(11): p. 2503-2512.
32. Thompson, D.A.W., *On Growth and Form*. 1917, Cambridge England: University Press.
33. Tobin, S.T., Barry, J.D., Meagher, A.J., Bulfin, B., O'Rathaille, C.E., and Hutzler, S., Ordered Polyhedral Foams in Tubes with Circular, Triangular and Square Cross-Section. *Colloids and Surfaces A: Physicochemical and Engineering Aspects*, 2011. 382(1): p. 24-31.
34. Tobin, S.T., Barry, J.D., Meagher, A.J., Bulfin, B., O'Rathaille, C.E., and Hutzler, S., Ordered Polyhedral Foams in Tubes with Circular, Triangular and Square Cross-Section. *Colloids and Surfaces A: Physicochemical and Engineering Aspects*, 2011. 382(1-3): p. 24-31.

35. Weaire, D. and Hutzler, S., *Foams and Analogous Cellular Systems*. 2019.
36. Weaire, D. and Hutzler, S., *The Physics of Foams*. 1999: Oxford : Clarendon Press ; New York : Oxford University Press.
37. Weaire, D., Hutzler, S., and Pittet, N., Cylindrical Packings of Foam Cells. *Forma*, 1992. 7(3): p. 259-263.
38. Young, T., An Essay on the Cohesion of Fluids. *Philosophical Transactions of the Royal Society of London*. Vol. 95. 1804: W. Bowyer and J. Nichols for Lockyer Davis, printer to the Royal Society.

APPENDICES

Appendix A: Example Surface Evolver File

```
//3D model for foam in infinite rigid elliptical tube. Tube wall does not
contribute to energy.

parameter tensC = 1
parameter tens = 0
parameter cell_opacity = .5
parameter cross_sectional_area = 50
parameter eccentricity = 0
parameter lambda = 1

//computed parameters
parameter radiusx = sqrt(cross_sectional_area/(pi*sqrt(1-eccentricity^2)))
parameter radiusy = sqrt((1-eccentricity^2)*radiusx^2)
parameter centerx = radiusx+10
parameter centery = radiusy+10
parameter tubeD = 2*sqrt(cross_sectional_area/pi)
parameter cellD = tubeD/lambda
parameter cell_volume = (4*pi*(cellD/2)^3)/3
parameter initial_height = 2*cell_volume/cross_sectional_area
parameter theta = atan(radiused/radiusx)+pi/2

torus_filled

periods
(2*centerx) 0 0
0 (2*centery) 0
0 0 (initial_height)

constraint 1 convex
formula: ((x-centerx)*cos(theta)+(y-centery)*sin(theta))^2/(radiusx^2) + ((x-
centerx)*sin(theta)-(y-centery)*cos(theta))^2/(radiusy^2)=1

constraint 2 nonpositive
formula: ((x-centerx)*cos(theta)+(y-centery)*sin(theta))^2/(radiusx^2) + ((x-
centerx)*sin(theta)-(y-centery)*cos(theta))^2/(radiusy^2)=1

vertices
1 centerx-radiusx centery-radiusy 0 constraint 1
2 centerx+radiusx centery-radiusy 0 constraint 1
3 centerx+radiusx centery+radiusy 0 constraint 1
4 centerx-radiusx centery+radiusy 0 constraint 1
5 centerx-radiusx centery-radiusy 1*initial_height/4 constraint 1
6 centerx+radiusx centery+radiusy 1*initial_height/4 constraint 1
7 centerx-radiusx centery+radiusy 1*initial_height/4 constraint 1
8 centerx-radiusx centery-radiusy 3*initial_height/4 constraint 1
9 centerx+radiusx centery-radiusy 3*initial_height/4 constraint 1
10 centerx+radiusx centery+radiusy 3*initial_height/4 constraint 1
11 centerx-radiusx centery-radiusy 4*initial_height/4 constraint 1
12 centerx+radiusx centery-radiusy 4*initial_height/4 constraint 1
13 centerx+radiusx centery+radiusy 4*initial_height/4 constraint 1
14 centerx-radiusx centery+radiusy 4*initial_height/4 constraint 1

edges
1 1 5 * * * constraint 1
2 3 6 * * * constraint 1
```

```

3    4  7  * * * constraint 1
4    2  9  * * * constraint 1
5    5  8  * * * constraint 1
6    6 10  * * * constraint 1
7    7 14  * * * constraint 1
8    8 11  * * * constraint 1
9    9 12  * * * constraint 1
10   10 13  * * * constraint 1
11   5  6  * * * constraint 2 //not fixed to wall
12   6  7  * * * constraint 1
13   7  5  * * * constraint 1
14   8  9  * * * constraint 1
15   9 10  * * * constraint 1
16  10  8  * * * constraint 2 //not fixed to wall
17  12  2  * * + constraint 1
18  11  1  * * + constraint 1
19  13  3  * * + constraint 1
20  14  4  * * + constraint 1

faces
1    14 15 16          tension 2*tensC  constraint 2  color
yellow //red-red surf.
2    11 12 13          tension 2*tensC  constraint 2  color
cyan //blue-blue surf.
3   -15 -4 -17 -9 15 10 19 2 6  tension tens  density 0  constraint 1
color red //red ext.
4   -14 -5 -1 -18 -8 14 9 17 4  tension tens  density 0  constraint 1
color red //red ext
5    5 -16 -6 -11      tension 2*tensC  constraint 2  color
green //shared middle
6    8 18 1 11 -2 -19 -10 16  tension 2*tensC  constraint 2  color
green //shared wrap
7    7 20 3 -12 -2 -19 -10 -6 12 tension tens  density 0  constraint 1
color blue //blue ext
8    5 8 18 1 -13 -3 -20 -7 13  tension tens  density 0  constraint 1
color blue //blue ext

bodies
1    2 -5 -6 7 8 -2    volume cell_volume //blue cell
2   -1 3 4 5 6 1      volume cell_volume //red cell

read
connected          //view two complete cells
U                  //conjugate gradient method ON
G 0                //no gravity, probably not necessary for torus space
but to be safe
delete facets where area=0 //delete superfluous facets, cuts down on error
messages
set facet.opacity cell_opacity //see through cells
calc_ecc:={print sqrt(1-(radiusy/radiusx)^2)} //compute equilibrium
eccentricity once reached

```


Appendix B: Fit Analysis

Table 5.1: Summary of fit analysis for each quadratic $p_e(\lambda)$ used to interpolate the staircase pattern for the rigid sheath model.

e	RSquare	RMSE	ANOVA	$p_e(\lambda)$	Number of points used for fit
0	0.999961	0.002051	F<0.0063	$1.23 + 1.66\lambda + 1.55(\lambda - 1.16)^2$	4
0.1	0.999997	0.000559	F<0.0017	$1.24 + 1.65\lambda + 1.58(\lambda - 1.16)^2$	4
0.2	0.999833	0.003514	F<0.0002	$1.27 + 1.61\lambda + 1.38(\lambda - 1.14)^2$	5
0.3	0.999881	0.002938	F<0.0001	$1.29 + 1.59\lambda + 1.49(\lambda - 1.14)^2$	5
0.4	0.99964	0.005135	F<0.0004	$1.25 + 1.59\lambda + 1.61(\lambda - 1.14)^2$	5
0.5	0.999999	0.000417	F<0.0011	$1.11 + 1.68\lambda + 1.52(\lambda - 1.15)^2$	4
0.6	0.999989	0.001224	F<0.0032	$1.05 + 1.68\lambda + 1.83(\lambda - 1.15)^2$	4
0.7	0.999954	0.002166	F<0.0001	$1.09 + 1.59\lambda + 1.77(\lambda - 1.12)^2$	5
0.8	0.999968	0.001912	F<0.0001	$0.94 + 1.62\lambda + 1.78(\lambda - 1.11)^2$	5
0.9	0.999994	0.000964	F<0.0001	$0.69 + 1.69\lambda + 1.96(\lambda - 1.10)^2$	5

Appendix C: Table of Symbols

Name	Type	Definition	Units
x, y, z	Independent variable	Coordinates	L
γ_c	Parameter	Interfacial tension between cells	M/T^2
γ_s	Parameter	Interfacial tension between cell and sheath	M/T^2
Γ	Parameter	Pressure ratio γ_s/γ_c	-
p	Parameter	Cell pressure	$M/(LT^2)$
S	Parameter	Tube cross-sectional area	L^2
v	Parameter	Cell volume	L^3
h	Parameter	Initial cell height	L
d	Parameter	Diameter of sphere with volume v	L
D	Parameter	Diameter of circle with area S	L
λ	Parameter	Diameter ratio D/d	-
A	Dependent variable	Cell surface area	L^2
Ω	Dependent variable	Energy	$L^2 M/T^2$

Table 5.2: Common parameters and variables used in the three foam models.

Appendix D: MATLAB Orthogonality Algorithm

```
function [ pattern ] = OrthPatternFinder(data)
%Orthogonal Pattern Finder
%Creates vectors between 3D data points and calls transitions based on
%periodicity. Transitions returned as strings with relevant index.

%Used in conjunction with PatternInterpreter

data=xlsread(data);

xpoints=data(:,1);
ypoints=data(:,2);
zpoints=data(:,3);
numelems=length(xpoints);

%Step 0: Preallocate vectors
xvec=zeros(numelems-1, 1);
cosangle1=xvec;
cosangle2=xvec;
cosangle3=xvec;
pattern1=strings(2, numelems-1);
pattern2=strings(2, numelems-1);
pattern3=strings(2, numelems-1);
pattern=strings(numelems-1,1);

hightol=.9;
lowtol=.1;

%Step 1: Check for bamboo and potential hopscotch
p=1;
for i=1:numelems-1
    xvec = xpoints(i+1)-xpoints(i);
    yvec = ypoints(i+1)-ypoints(i);
    zvec = zpoints(i+1)-zpoints(i);
    normxyzv = sqrt(xvec^2+yvec^2+zvec^2);
    dot1 = xvec*1;
    cosangle1(i)=dot1/normxyzv;
    if cosangle1(i)>hightol
        pattern1(1,p)=i;
        pattern1(2,p)= "H";
        p=p+1;
        pattern(i)="H";
    elseif cosangle1(i)<lowtol
        pattern1(1,p)=i;
        pattern1(2,p)="V";
        p=p+1;
        pattern(i)="V";
    end
    pattern1=pattern1(:,1:p-1);
end

%Step 2: Check for staircase
p=1;
for j=1:numelems-2
    xvec = xpoints(j+2)-xpoints(j);
    yvec = ypoints(j+2)-ypoints(j);
    zvec = zpoints(j+2)-zpoints(j);
```

```

    normxyzv =sqrt(xvec^2+yvec^2+zvec^2);
    dot2 = xvec*1;
    cosangle2(j)=dot2/normxyzv;
    if (cosangle2(j)>=hightol) && cosangle1(j)<hightol
        pattern2(2,p)= "P2";
        pattern2(1,p)=j;
        p=p+1;
    end
    pattern2=pattern2(:,1:p-1);
end

%Step 3: Check for chiral
p=1;
for k=1:numelems-3
    xvec = xpoints(k+3)-xpoints(k);
    yvec = ypoints(k+3)-ypoints(k);
    zvec = zpoints(k+3)-zpoints(k);
    normxyzv =sqrt(xvec^2+yvec^2+zvec^2);
    dot2 = xvec*1;
    cosangle3(k)=dot2/normxyzv;
    if (cosangle3(k)>=hightol) && cosangle1(k)<hightol &&
cosangle2(k)<hightol
        pattern3(2,p)= "P3";
        pattern3(1,p)=k;
        p=p+1;
        pattern(k)="P3";
    end
    pattern3=pattern3(:,1:p-1);
end

```

Appendix E: Tissue self-organization underlies morphogenesis of the notochord

The following paper was published in Philosophical Transactions of the Royal Society B in September 2018.

Research



Cite this article: Norman J, Sorrell EL, Hu Y, Siripurapu V, Garcia J, Bagwell J, Charbonneau P, Lubkin SR, Bagnat M. 2018 Tissue self-organization underlies morphogenesis of the notochord. *Phil. Trans. R. Soc. B* **373**: 20170320.
<http://dx.doi.org/10.1098/rstb.2017.0320>

Accepted: 3 August 2018

One contribution of 14 to a Theo Murphy meeting issue 'Mechanics of development'.

Subject Areas:

developmental biology

Keywords:

zebrafish, notochord, vacuolated cells, packing, self-organization

Author for correspondence:

Michel Bagnat
e-mail: m.bagnat@cellbio.duke.edu

Electronic supplementary material is available online at <http://dx.doi.org/10.6084/m9.figshare.c.4195415>.

Tissue self-organization underlies morphogenesis of the notochord

James Norman¹, Emma L. Sorrell^{1,3}, Yi Hu², Vaishnavi Siripurapu^{1,4}, Jamie Garcia¹, Jennifer Bagwell¹, Patrick Charbonneau², Sharon R. Lubkin³ and Michel Bagnat¹

¹Department of Cell Biology, and ²Department of Chemistry, Duke University, Durham, NC 27710, USA

³Department of Mathematics, North Carolina State University, Raleigh, NC 27695-8205, USA

⁴North Carolina School of Science and Mathematics, Durham, NC 27705, USA

id SRL, 0000-0003-2521-0699; MB, 0000-0002-3829-0168

The notochord is a conserved axial structure that in vertebrates serves as a hydrostatic scaffold for embryonic axis elongation and, later on, for proper spine assembly. It consists of a core of large fluid-filled vacuolated cells surrounded by an epithelial sheath that is encased in extracellular matrix. During morphogenesis, the vacuolated cells inflate their vacuole and arrange in a stereotypical staircase pattern. We investigated the origin of this pattern and found that it can be achieved purely by simple physical principles. We are able to model the arrangement of vacuolated cells within the zebrafish notochord using a physical model composed of silicone tubes and water-absorbing polymer beads. The biological structure and the physical model can be accurately described by the theory developed for the packing of spheres and foams in cylinders. Our experiments with physical models and numerical simulations generated several predictions on key features of notochord organization that we documented and tested experimentally in zebrafish. Altogether, our data reveal that the organization of the vertebrate notochord is governed by the density of the osmotically swelling vacuolated cells and the aspect ratio of the notochord rod. We therefore conclude that self-organization underlies morphogenesis of the vertebrate notochord.

This article is part of the Theo Murphy meeting issue on 'Mechanics of development'.

1. Introduction

In essence, all morphogenetic processes are the result of one or more self-organized events governed by physical principles. This is illustrated by the fact that a properly proportioned and physiologically active embryo, with all its organs, can be generated from an externally fertilized egg. Identifying the key features and understanding the underlying principles that guide specific morphogenetic processes constitutes one of the major challenges in biology. The discovery of oscillations in simple chemical systems and the formal description of reaction–diffusion processes paved the way for the understanding of the physical principles governing many sub-cellular processes (reviewed in [1]). The celebrated and highly influential theoretical work of Turing [2], who predicted the emergence of stable patterns via reaction–diffusion mechanisms, has been the conceptual basis of much of the work on biological modelling. This has been applied initially to describe signalling and patterning cues [3–5], and more recently to the emergence of tissue and organ level structures [6–8]. However, it is clear that other conceptual frameworks can also reach similar conclusions [9]. The main difficulties for modelling morphogenetic processes lie in the identification of the key components and the most relevant physical parameters. One successful approach to these problems has been to take the perspective of the engineer, using geometric [10] and continuum

mechanical modelling [11], as well as macroscopic physical models [12]. These studies have inspired us to build a physical model to capture key elements controlling the organization of the zebrafish notochord.

The zebrafish notochord is a rod that spans most of the antero-posterior (AP) axis and serves as a hydrostatic scaffold for embryonic axis elongation and later on for spine assembly [13]. It is composed of a core of large vacuolated cells surrounded by an epithelial sheath that is encased in a thick extracellular matrix [14,15]. Both cell types differentiate from a common precursor via a Notch-dependent mechanism [16]. Each vacuolated cell nucleates a single fluid-filled vacuole, which is a lysosome-related organelle, that occupies most of the cellular volume [13]. As the vacuoles inflate by accumulating water, the vacuolated cells expand within the confinement created by the cylindrical notochord sheath, resulting in an expansion of the AP axis [13,17]. Loss of vacuolated cells or fragmentation of vacuoles leads to shortening of the AP axis and kinking of the spine [13]. The sheath also plays important structural roles [18–20] and forms a template for patterning the segmented vertebrae [21–23]. Sheath cells are also able to regenerate vacuolated cells following collapse or injury [24,25].

Once notochord morphogenesis is completed, the vacuolated cells are arranged in a stereotypical staircase pattern [15]. While such arrangement could result from interactions with other tissues such as the bilateral paraxial mesoderm, we reasoned that being surrounded by another cell layer and a thick matrix would make that scenario unlikely. Instead, we hypothesized that vacuolated cells are arranged via a self-organized process. Here, we identify key physical and geometric parameters to build a simple physical model whose main predictions we tested *in vivo* in zebrafish. Our results indicate that vacuolated cells are organized by simple packing rules that are governed by cell density and the aspect ratio of the notochord rod.

2. Material and methods

(a) Animals

Zebrafish: *Danio rerio* stocks were maintained at 28°C and bred as previously described [26]. Zebrafish stocks were healthy and of normal immune status, not involved in previous procedures, and were drug test naive. Male and female breeders from three to nine months of age were used to generate fish for all experiments. In total, zebrafish larvae from Ekkwill background at 1–8 days post-fertilization were used in this study. The *Tg(rcn3:QF2)*^{pd1190} strain was generated for this study using a Tol2 construct [27] in which the *rcn3* promoter [13] drives expression of QF2 [28]. Previously published strains were as follows: *cavin1b*^{bms110} [24], *Tg(col9a2:mcherry)*^{pd1150} [24], *Tg(col8a1a:GFPcax)*^{pd1152} [24], *Tg(rcn3:GFPPrab32a)*^{pd1153} [24], *Tg(QUAS:nlsVenus-V2a-notch1-alcD)*^{pd1164} [21], *Tg(QUAS:nVenus-V2a-SuHDN)*^{pd1165} [21].

Xenopus: *Xenopus laevis* tadpoles (stages 33–34) fixed in para-formaldehyde were kindly provided by the laboratory of Nanette Nascone-Yoder.

(b) Physical models

Silicone tube models were made with clear silicone tubing (OCSparts.com) and sodium polyacrylate gel beads (JBs) (Jelly BeadZ, jellybeads.com). The silicone tubes had a length of either 29 cm (figures 1 and 2) or 30.48 cm (figure 5) with

an inner diameter of 12.7 mm, an outer diameter of 15.9 mm and a wall thickness of 3.2 mm. Circular tube models were made using clear polycarbonate tubing and elliptical tube models were made using clear vinyl tubing (OCSparts). Polypropylene tube caps, punctured to allow water flow, were placed on one end of the silicone tube and then sealed with parafilm. Dry JBs were placed inside empty and dry silicone tubes, which were then capped and sealed with parafilm. Tubes were then submerged in a distilled water bath and allowed to completely fill with water. Then, JBs were given at least 3.5 h to grow and distribute throughout the tube before being scored for patterns. For sectioning, silicone tubes were frozen and cut into cross sections using a hacksaw. Images of the tubes and the patterns generated were taken using a cell phone camera. Time-lapse videos of the JBs growing and arranging in the tubes were taken using a Go Pro HERO 3 camera.

Aspect ratio was measured for all tubes using a digital calliper (Fine Science Tools, Foster City, CA, USA) at 11 points, equally spaced 2.54 cm apart, along the length of the tube. For the silicone tube deformation experiment (figure 5e), the aspect ratio was measured before and after JB swelling.

(c) Simulations

For circular cylinders, sphere centres are confined within a cylinder of radius $w = (D - d)/2$, where D is the inner diameter and d is the sphere diameter. In other words, sphere centres must lie no further than $r \leq w$ from the central axis of the cylinder. For elliptic cylinders, the corresponding boundary condition does not have a simple analytical form, but for sufficiently small D ($D/d \leq 2.71486$ for circular cylinders [29]) all spheres are in contact with the cylindrical wall at close packing. We can thus reformulate the problem as identifying the densest packing of sphere centres set on the surface of an elliptic cylinder. This approximation is valid in the limit of small eccentricity. The semi-major axis and semi-minor axis are such that $ad > bd$. In order to more easily compare our results with experiments, we define two diameters, $D_a/d = 1 + 2a$ and $D_b/d = 1 + 2b$, and hence the aspect ratio $\alpha = D_a/D_b$.

We follow the sequential linear programming (SLP) scheme described before [30–32] to identify the densest sphere packing for a fixed cylinder geometry. At each optimization step, N particles on the surface of the elliptic cylinder move with small angular and axial displacements ($\Delta\theta_i, \Delta z_i$), and the unit cell height, h_z , changes by a relative shrinkage factor, ε_z . The coordinates of the sphere i before and after the movement are thus

$$(x_i, y_i, z_i) = (a \cos(\theta_i), b \sin(\theta_i), z_i)$$

$$\text{and } (x'_i, y'_i, z'_i) = (a \cos(\theta_i + \Delta\theta_i), b \sin(\theta_i + \Delta\theta_i), (1 - \varepsilon_z)(z_i + \Delta z_i))$$

where $0 \leq \theta_i < 2\pi$ and $0 \leq z_i < h_z$. Finding the maximum packing density is then equivalent to minimizing h_z , subject to

$$r'_{ij} \geq d, \quad \forall ij \text{ neighbour pairs,}$$

$$|\Delta\theta_i| \leq \Delta\theta_{\theta}^{\text{upper}} \quad \forall i,$$

$$|\Delta z_i| \leq \Delta z_z^{\text{upper}} \quad \forall i,$$

$$|\varepsilon_z| \leq \varepsilon_z^{\text{upper}},$$

where r_{ij} denotes the distance between neighbouring pairs, which can be linearized by Taylor expansion if the upper bound (denoted by the superscript ‘upper’) for a single step is sufficiently small. Here we set $r_{\theta}^{\text{upper}} = r_z^{\text{upper}} = 0.002d$ and $\varepsilon_z^{\text{upper}} = 0.002$ and sequentially conduct optimization steps until convergence, i.e. $\varepsilon_z < 10^{-6}$. Because the number of spheres in the unit cell (N) for dense packing is not known, we scan N from 6 to 50 and repeat 100 times with different initial structure to identify potential densest structure for each pair of D_a/d and D_b/d considered.

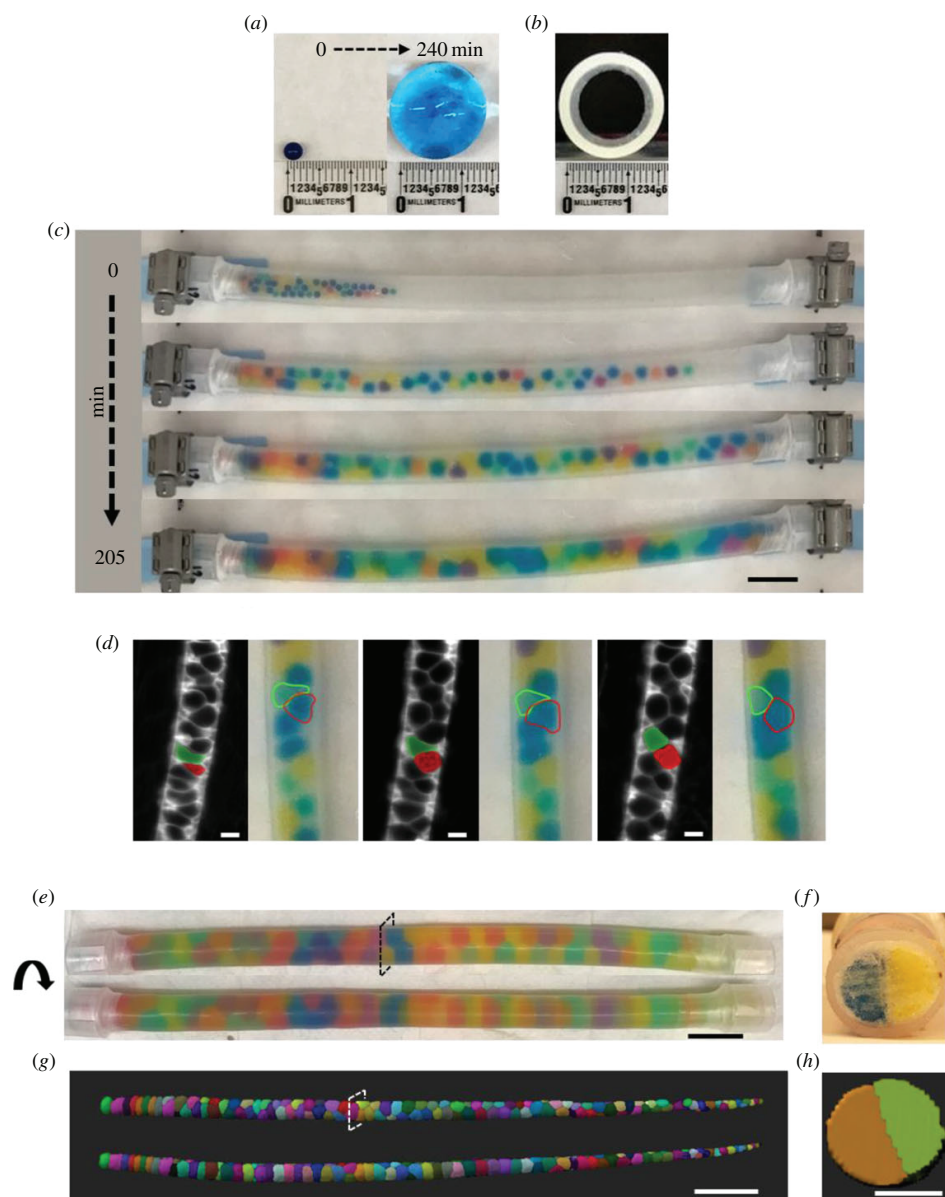


Figure 1. A physical model recapitulates the organization and key behaviours of the zebrafish notochord. (a) A single JB before (left panel) and after (right panel) being placed in a water bath to grow unrestricted. (b) Cross-section image of an empty circular silicone tube (inner diameter, 12.7 mm). (c) Time-lapse images of JBs swelling in a capped silicone tube. Scale bar, 2.5 cm. (d) Still images from time-lapse movies of vacuolated cells in the notochord of a zebrafish embryo starting at the 20-somite stage and JBs as they settle in their final arrangement. Two cells wedging into a staircase arrangement are pseudo-coloured in green and red. A similar behaviour is highlighted for JBs traced with dotted lines. Scale bar, 20 μm . (e) Rotating views of a silicone tube filled with 80 JBs. (f) Cross section of the tube shown in (e) taken at the indicated level. Scale bar, 2.5 cm. (g) Dorsal (top) and lateral (bottom) views of a three-dimensional rendering of a 48 h post-fertilization (hpf) wild-type (WT) zebrafish expressing plasma-membrane-targeted green fluorescent protein (GFP) in vacuolated cells of the notochord. Note similarities between the arrangement of vacuolated cells, mainly in a 'staircase' pattern, and the JB tube shown in (e). (h) Orthogonal view of the notochord shown in (g). Scale bars, (g) 200 μm , (h) 50 μm .

(d) Microscopy

Three-dimensional renderings were generated from whole-mount confocal live images obtained on a Fluoview FV3000 (Olympus) confocal microscope equipped with 30 \times /1.05 silicone oil objective (Olympus) and Fluoview software (Olympus). Fish were mounted onto glass-bottom dishes in a 3% methylcellulose mixture of egg water and 1 \times tricane. Digital stitching of confocal images used for Imaris renderings was done in the FLUOVIEW software. Time-lapse movies of notochord morphogenesis were

recorded on a Lightsheet Z.1 microscope (Carl Zeiss) as previously described [24].

(e) Image processing

Notochord renderings were created using the IMARIS v. 9.0.0 and 9.1.2 software (Bitplane USA, Concord, MA). Notochord renderings were created using both the *surface* and *cells* features (IMARIS software, v. 9.0.0 and 9.1.2, respectively). Centroids, volumes

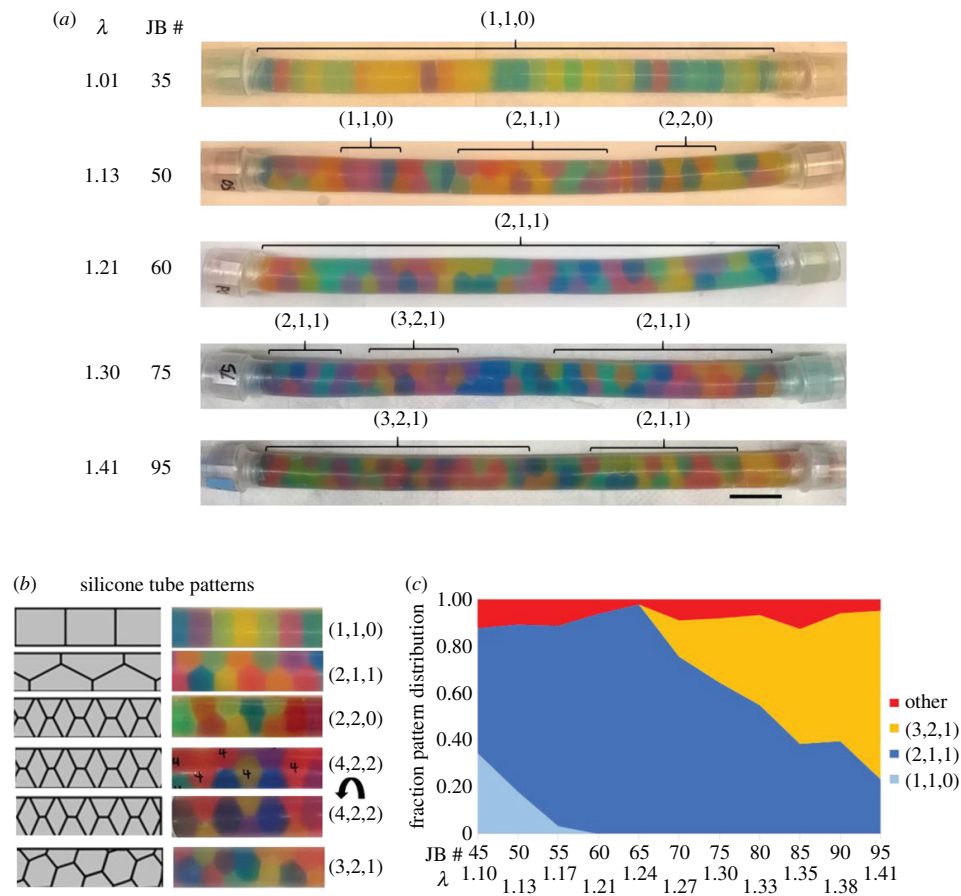


Figure 2. JB arrangement in capped silicone tubes depends on bead density. (a) Images of capped silicone tubes filled with a range of JB numbers (30–95) that swelled to fill the available space. JB numbers and their respective calculated λ values are indicated on the left. Brackets mark regions of specific patterns. Scale bar, 2.5 cm. (b) Schematic (left) and images (right) of JB patterns observed in capped silicone tubes. (c) Quantification of the fraction of JB pattern observed for various JB densities ($n = 3$). Corresponding λ values and JB numbers are shown at the bottom.

and diameters were obtained for each vacuolated cell using the *detailed statistical analysis* function for the reconstructed notochords in the IMARIS software v. 9.0.0 and 9.1.2.

(f) Morphometric analyses

(i) Notochords

Centroid locations were obtained from image processing software (IMARIS) in (x, y, z) coordinates corresponding roughly to (AP, DV and LR) axes, in micrometre units. Notochord tube diameter was determined by two methods. (a) Creating a running sum of cell volumes $V(x)$ from head to tail, such that the local cross-sectional area $A(x)$ is dV/dx . Diameters in the LR and DV directions $D_{LR}(x)$ and $D_{DV}(x)$ were determined either on the assumption that the cross section was circular, or on the assumption that it was elliptical, with the same aspect ratio measured by method (b). (b) Measuring major and minor axes in Fiji 1.50a from cross sections every 100 μm . Methods (a) and (b) were verified to measure statistically equal area values for wild-type (WT) zebrafish. Aspect ratio was defined for notochords as $D_{LR}(x)/D_{DV}(x)$.

Diameter ratios $\lambda(x) = D(x)/d(x)$ were determined from smoothed tube diameters and smoothed cell volumes, using the diameters of equivalent spheres of the same volume as the cells. For each fish, we created a local coordinate system (X, Y, Z) , normalizing cell centroid positions so that (1) the head was at $X = 0$; (2) the centreline was at $(Y, Z) = (0, 0)$; (3) each cross section had

radius 1. Patterns were classified on the basis of the vector defined by connecting two adjacent centroids, and this vector's angle relative to the XY and XZ axes in the normalized coordinate system (X, Y, Z) . For each centroid, vectors were created between them and the following centroids, and the angle between each of these vectors and the X axis was calculated sequentially until a vector was found to be parallel to the X axis. The periodicity of a centroid C was then defined as the number of centroids examined in this process, and all centroids examined were assigned the same periodicity as C . Cell arrangement patterns were classified for each centroid by categorizing sub-sequences within the sequence of periodicities in Matlab using the code *PatternInterpreter.m*. Cells in transitional patterns were flagged in this program and then assessed manually based on the surrounding cell patterns. Transitional cells were counted as half a cell in each pattern. Sphere figures were created for each fish by plotting a sphere with the same volume as each cell at each cell's normalized position. These were then colorized using the pattern classifications previously determined, using Maple 2017.

(ii) JB tubes

JB patterns were classified visually. In order for a JB to count towards a pattern, we required there be at least three sequential JBs in this pattern. We counted JB transitions between patterns,

where a JB could be considered in either pattern, as half a JB for each pattern. Regular hopscotch was defined to be two JBs in staircase alternating with one in bamboo. Any pattern that was a mixture of staircase and bamboo, but did not have a sequence of three JBs in the same pattern, was classified as irregular hopscotch.

To calculate λ , the volume of the tube, calculated as the volume of a cylinder with height and diameter equal to the measured height and interior diameter of the tube, was divided by the number of JBs to obtain the volume of each JB. From this, the diameter of a JB was calculated as the diameter of a sphere with equivalent volume. Because the tubes lack a distinguished orientation, aspect ratios for tubes were defined as $D_M(x)/D_m(x)$ where $D_M(x)$ is the largest diameter at location x and $D_m(x)$ is the smallest.

(g) Statistical analyses

Statistical analysis was performed in JMP® PRO v. 13.0.0 (SAS Corp., Cary, NC, USA) and GRAPHPAD PRISM v. 7.0c for Mac (GraphPad Software, La Jolla, CA, USA).

3. Results

(a) A physical model of the zebrafish notochord

In the zebrafish, notochord vacuolated cells are organized in a consistent staircase pattern [15]. To investigate the mechanism that controls the arrangement of vacuolated cells during morphogenesis, we built a physical model. We conceptualized the notochord as a cylinder containing liquid-filled spheroids. This is reminiscent of the arrangement of hard spheres or detergent foam cells (soap bubbles) in cylinders, which have both been extensively studied using theory and experimental approaches in soft matter physics. In those systems, spheres or foam cells arrange in progressively more complex patterns as the ratio ($\lambda = D/d$) of the diameter of the cylinder (D) over that of the spheres or cells (d) increases [33–35]. The range of patterns observed as λ increases follows a progression from a row of single units, called ‘bamboo’ and noted as (1,1,0) using the nomenclature derived from phyllotaxis [35,36], to a ‘staircase’ or ‘zigzag’ (2,1,1), and then to more complex helical and chiral patterns such as (3,2,1) [35,36]. For a given λ value different patterns have been observed to coexist, separated by transitional arrangements (‘defects’ in the terminology of crystallography). While these patterns are generally reminiscent of the arrangement of vacuolated cells in the notochord there are important differences that limit the applicability of the established models. First, unlike the existing physical models, vacuolated cells do not have a constant nor uniform size and shape. Second, unlike hard sphere models, vacuolated cells completely fill their available space. While this property is also present in cylindrical foams, these resemble epithelia and their interaction is completely driven by surface tension. By contrast, vacuolated cells are not epithelial and do not, at least during morphogenesis, establish junctions between neighbouring vacuolated cells or with sheath cells. Third, in cylindrical foams and hard sphere packing templating effects can bias pattern formation [36,37]. Therefore, we wanted to generate a physical model that resembles the properties of notochord vacuolated cells more closely.

Because the arrangement of vacuolated cells in the notochord during morphogenesis occurs as the cells inflate by drawing in fluid [13], we initially tried to emulate

vacuolated cells using starch beads (tapioca pearls) and the notochord sheath using collagen sausage casing or silicone tubes. Alas, the high softness of the starch beads and their relatively rapid disintegration made this set-up unsuitable to analysis. After a brief survey of other common materials, we found sodium polyacrylate beads (a.k.a. JBs) to be suitable. These beads are deformable hydrogels, comprising a polymer network that absorbs a significant amount of water to swell in aqueous solutions. Thus, these beads mimic the polymeric nature of the cytoskeleton and exhibit large shape changes through swelling like the vacuolated cells.

When placed in water, dry JBs swell from approximately 1.5 mm to approximately 15 mm in a span of 4 h at room temperature and assume a spherical shape (figure 1a), similar to vacuolated cells isolated from the zebrafish notochord [24]. When placed at one end of a capped silicone tube JBs swelled and distributed throughout the tube in about 3.5 h (figure 1c), mimicking the expansion of the embryonic axis driven by notochord vacuolated cell expansion [13]. If one cap is removed from the tube the expanding JBs extrude from the open end, similar to what occurs with vacuolated cells when the tail of a 24 h post-fertilization (hpf) embryo is cut (electronic supplementary material, video S1). Interestingly, when compared with the behaviour of vacuolated cells during morphogenesis (electronic supplementary material, video S2) we observed that JBs exhibited similar movements as they locked into their final arrangement (figure 1c). We then tested different types of tubes of varying diameters and a range of JB numbers. We found that placing an appropriate number (see next section) of JBs in a capped 12.7 mm-wide silicone tube (a diameter slightly smaller than that of a fully swollen JB) results in a staircase arrangement that closely resembles that of vacuolated cells in the notochord of a 48hpf WT zebrafish (figure 1d).

Next, we explored JB arrangement at increasing λ values in capped tubes of constant length in which JBs swell to fill the available space. In this simple set-up, the final size each JB acquires is progressively reduced as the number of JBs per tube increases, thereby increasing λ . To calculate λ values, we simply divided the internal volume of the tubes by the number of JBs to obtain an equivalent sphere volume that we used to calculate the average JB diameter. As λ increased from 1 to 1.41, we observed bamboo (1,1,0), staircase (2,1,1), ‘hopscotch’ (2,2,0) and helical patterns (e.g. 3,2,1) appearing (figure 2a). Of note, the arrangement observed for each λ value was independent of the speed at which the JBs swelled and the initial distribution of the dry JBs (data not shown). The order of transitions from one pattern to the next and the λ values at which they occurred were consistent with those reported for hard spheres and cylindrical foams [30,35]. Similar to other packing models, we also observed the coexistence of different patterns within a tube (marked with brackets, figure 2a). However, unlike what has been reported for cylindrical foams [36], in our JB tubes the different patterns were intermixed and not sharply separated in large domains. We also observed the generation of mixed ‘hopscotch’ irregular arrangements (figure 2b) at the transitions between patterns. This may be comparable to the ‘line slip’ structures identified in the packing of wet foams, a model of soft sphere packing [38].

Together, these data show that a simple physical model composed of JBs swelling inside capped silicone tubes can

reproduce the arrangement and even some of the behaviours of zebrafish notochord vacuolated cells. These results also generate testable quantitative and qualitative predictions about the arrangement of vacuolated cells in the notochord.

(b) Vacuolated cell arrangement in the zebrafish

notochord is influenced by the aspect ratio of the rod

We next used confocal microscopy to image the entire notochord of 48hpf WT embryos expressing a plasma membrane marker in vacuolated cells and generated three-dimensional renderings. Using quantitative analyses, we obtained the position of each cell's centroid and plotted them in dorsal view and in cross section. As expected, the centroids were clustered along two areas that were consistent with a staircase pattern (figure 3a). However, a fraction of cells seemed to deviate from that pattern. To visualize arrangements, we generated three-dimensional renderings in which we placed a sphere of volume proportional to that of each vacuolated cell at the position of the respective centroid. We found that while most of the notochord length corresponds to the staircase pattern (2,1,1), some areas contain helical patterns, particularly (3,2,1) (figure 3b). Other patterns including (4,2,2), bamboo (1,1,0), which was often found at the rostral and caudal ends of the notochord, and hopscotch (2,2,0) were also present (electronic supplementary material, figure S1).

To compare the type and frequency of pattern occurrence between notochord vacuolated cells and JB's in silicone tubes, we first determined the λ value along the notochord of six 48hpf embryos. To do this, we took the local average volume of each cell and calculated the diameter based on a sphere of the same volume. We found that the λ value was on average 1.33 ± 0.14 , and that it varied along the length of the AP axis, tapering towards the caudal region (figure 3c). As expected, the λ value was significantly higher in areas of staircase and complex arrangements compared with the linear bamboo pattern (figure 3d). Overall, the frequency of each pattern observed *in vivo* in 48hpf embryos closely followed the distribution of JB tubes of the same λ value (figure 3e). However, we observed a significantly higher proportion of bamboo (1,1,0) and staircase (2,1,1) arrangements *in vivo* compared with the JB tubes (figure 3e). To identify what might explain this discrepancy, we first analysed the transverse aspect ratio (α) of the notochord in 48hpf embryos and found it is significantly elliptical with an average value of 1.07 ± 0.03 . Interestingly, when we analysed α values during notochord morphogenesis we found that the notochord rod is highly elliptical at the 'stack of coins' (chordamesoderm) stage and that it becomes more circular as the vacuolated cells inflate (electronic supplementary material, figure S2). These data suggest that the aspect ratio of the notochord rod influences the arrangement of the vacuolated cells.

(c) Elliptical cylinders favour staircase arrangement of hard spheres in simulations

To test whether the discrepancy between the notochord and the physical model can be explained by the geometry of the notochord rod, we conducted numerical simulations of

hard sphere packing in cylinders with a variable aspect ratio between 1 and 2. Specifically, we wanted to determine whether elliptical cylinders favour the (2,1,1) staircase arrangements. To this end, we used the SLP method, previously used to simulate hard sphere packing in circular cylinders up to a λ value of 4 [30], and adapted it to the case of elliptic cylinders.

Figure 4 shows the densest structures identified by SLP for different $\lambda = D_a/d$ up to 2.15 and $\alpha = D_a/D_b$. For $\lambda < 1.866$, next-nearest-neighbour contacts are impossible, hence the densest packings have a staircase morphology. A twisted staircase regime appears at $\lambda < 1.866$, and persists for a relatively small ellipticity, i.e. $\lambda < 1.05$. For larger α , hard spheres form a crossing staircase structure. Specifically, two staircase structures intersect every other sphere. The angle between the two planes of these two staircase structures increases with α . This helical regime diminishes upon approaching $\lambda = 2$, which in circular cylinders is achiral. For $\lambda > 2.039$, a triple helical structure, (3,2,1), appears. This helical structure also transforms into the crossing staircase structure as α increases. Similarly, between these two regimes complex intermediate structures with both discontinuous helical strands and bend crossing staircases appear. The crossing staircase structures generally become preferred as α increases.

(d) Reciprocal control of tube aspect ratio and local cell arrangement in physical models

The analysis of vacuolated cell arrangement suggested that the aspect ratio (α) of the notochord rod strongly influences the pattern these cells achieve. This notion was supported by numerical simulations indicating that elliptical cylinders strongly favour the (2,1,1) staircase arrangement. Because hard spheres impose constraints that limit their possible arrangements, we decided to test in physical models the effect of tube aspect ratio on JB arrangement. To this end, we procured relatively inflexible vinyl tubes of elliptical section ($\alpha = 1.25$) and hard polycarbonate tubes of circular section ($\alpha = 1.00$) and filled them with dry JB's which were allowed to swell as before. We tested a range of λ values close to those of the WT notochord and found that in the circular tubes the helical and chiral patterns were the most prominent, particularly at higher λ values (figure 5a,b). By contrast, in elliptical tubes JB's were arranged almost completely in a staircase (2,1,1) pattern (figure 5c,d).

Next, we re-visited the silicone tube model and took into account their aspect ratio and the material properties. We first measured the aspect ratio before the addition of JB's and found $\alpha = 1.02$ throughout its length. Then, we added 80 JB's and allowed them to swell as before, reaching a λ value of 1.31, before scoring JB arrangement and the local aspect ratio. Interestingly, we found that the tubes deformed locally from $\alpha = 1.00$ up to 1.17 and that the areas with (2,1,1) staircase pattern were significantly more elliptical than those presenting the chiral pattern (3,2,1) (figure 5f). We then compared the fraction of staircase (2,1,1) arrangement present in silicone and hard polycarbonate tubes at a λ value of 1.33 and found it is significantly higher in the deformable silicone tube (figure 5g).

Together, these data indicate that the aspect ratio of the cylinder strongly influences the local arrangement of JB's

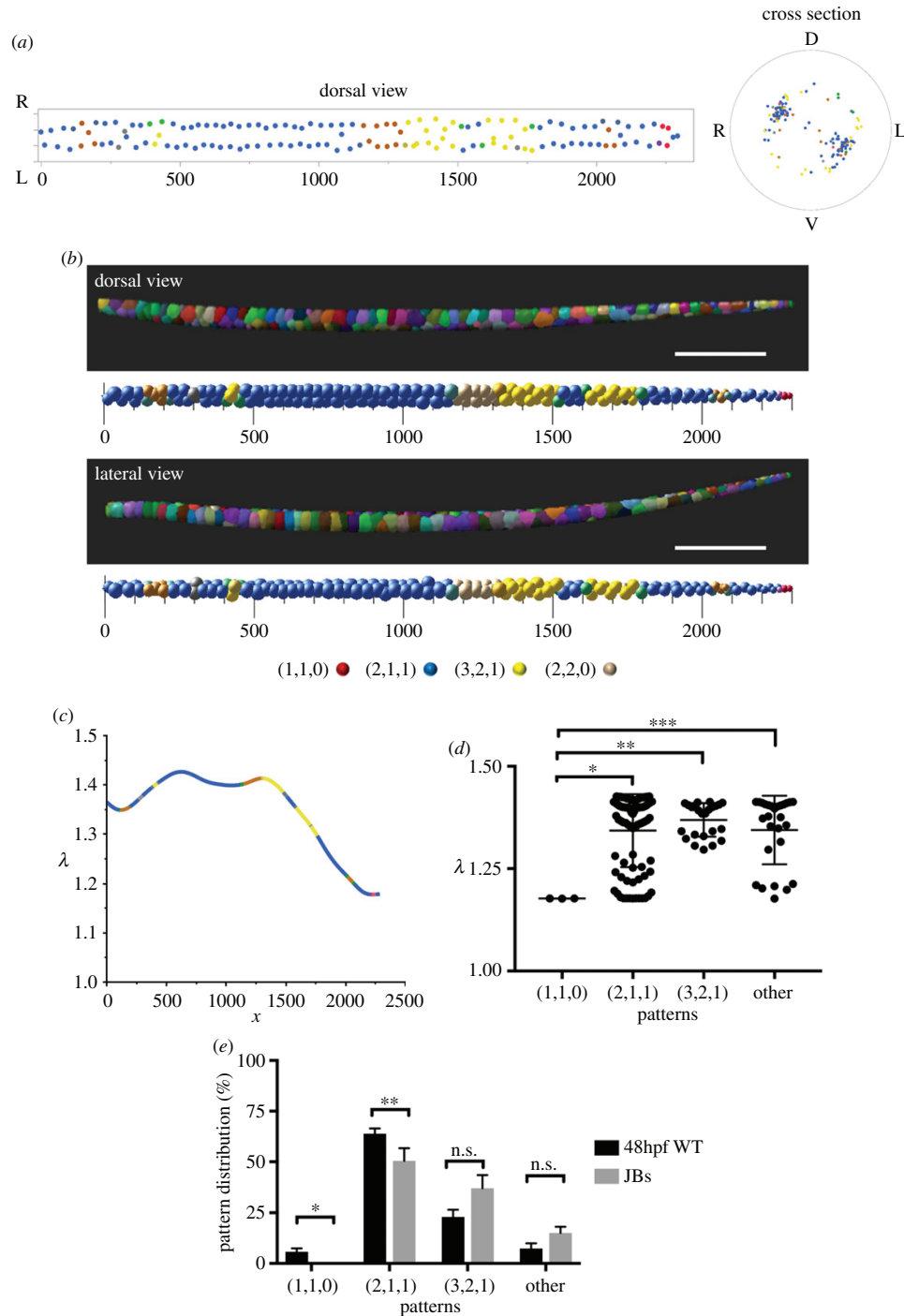


Figure 3. The organization of vacuolated cells in the zebrafish notochord and the aspect ratio of the notochord rod are interrelated. (a) Dorsal (left) and cross-sectional (right) centroid plots of notochord vacuolated cells for a 48hpf WT zebrafish embryo. Orientation labels D (dorsal), V (ventral), L (left) and R (right). Units are in micrometres. (b) Lateral and dorsal views of three-dimensional renderings (top) and corresponding sphere plots (bottom) depicting the morphology and arrangement of vacuolated cells in a 48hpf WT zebrafish embryo. Colours in the sphere plots indicate patterns observed: blue (2,1,1), yellow (3,2,1), red (1,1,0), orange (4,2,2), tan (2,2,0), grey (uncertain), green (transition between 2,1,1 and 3,2,1). Scale bars, 300 μm (c) λ values of vacuolated cells along the length of the notochord of a 48hpf WT embryo. Line colours reflect patterns as in (b). (d) λ values for different patterns in the notochord of a 48hpf WT embryo. One-way ANOVA, Tukey's test, * $p = 0.0037$; ** $p = 0.001$; *** $p = 0.005$. (e) Distribution of patterns in 48hpf WT embryos ($n = 6$) and JB tubes ($n = 3$, $\lambda = 1.33$). Paired t -test, * $p = 0.047$; ** $p = 0.045$.

in our physical model. Conversely, the local arrangement of JB tubes also modifies the aspect ratio of the tube, indicating these two key variables are interdependent. These data also

explain why in the largely elliptical WT zebrafish notochord rod vacuolated cells are arranged mostly in a staircase pattern while λ values are relatively high.

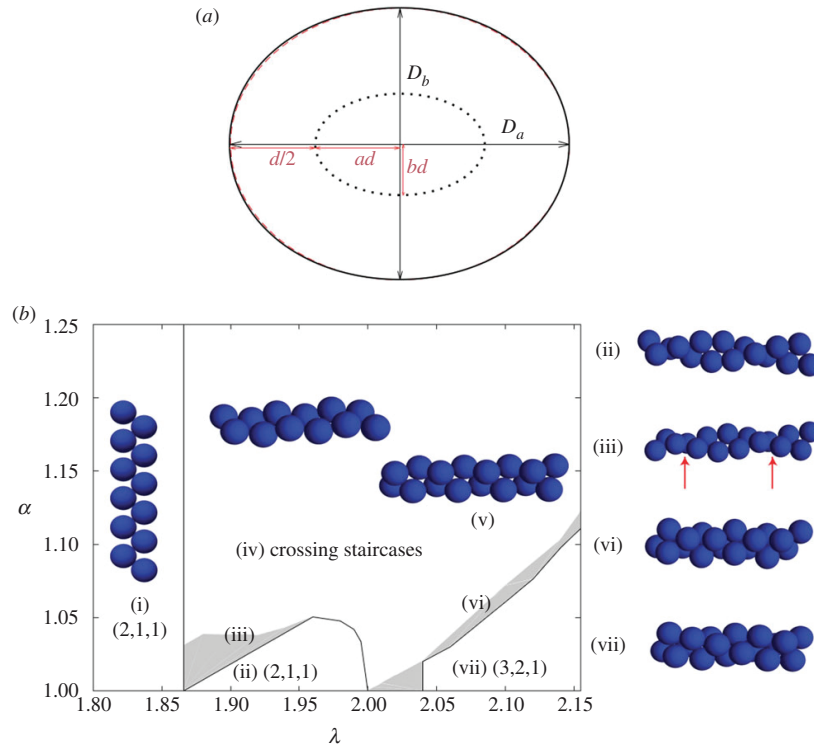


Figure 4. Elliptical cylinders favour the staircase arrangement of hard spheres in simulations. (a) Cross section of elliptical cylinder model. During the SLP optimization, hard sphere centres of diameter d evolve on the surface of an elliptical cylinder (dotted curve) with semi-major axis ad and semi-minor axis bd . The resulting boundary confinement (black solid curve) is approximately elliptical (red dashed curve) with major and minor diameters D_a and D_b , respectively, when $\alpha = D_a/D_b$ is small. The case $\alpha = 1.25$ is depicted here. (b) Diagram of the densest packings of hard spheres in cylinders of width up to $\lambda = 2.15$ and an elliptical aspect ratio α . Sharp transitions (solid lines) are observed between certain structures. Because of the competition between packing helicity and cylinder ellipticity, however, helicity is lost in two steps. It becomes discontinuous (solid line), before slowly vanishing (grey zones). Sample structures of (i) staircase (2,1,1) and (ii) twisted staircase (2,1,1); (iii) transitional defective (red arrows) structure between staircase and twisted staircase; (iv) and (v) crossing staircase (see text); (vi) triple helix (3,2,1); and (vii) transitional structure between (3,2,1) and crossing staircase regimes. The regime of staircase and twisted staircase is markedly enlarged for $\alpha > 1$. Note, however, that in this model the bamboo structure is only stable at $\lambda = 1$, and the hopscotch structure is always unstable. (Online version in colour.)

(e) The density of vacuolated cells determines their organization and influences the aspect ratio of the notochord rod

The experiments with our physical model of the notochord and our theoretical model generated two important predictions: (1) the arrangement of vacuolated cells within the notochord is dictated by cell density, which in turn defines the λ value as cells swell to occupy the available space; (2) vacuolated cell arrangement and the aspect ratio of the notochord rod are mutually regulated. To test these predictions *in vivo*, we first took a genetic approach to alter vacuolated cell density in the zebrafish notochord. Previous work in zebrafish has shown that differentiation of chordamesoderm cells, the notochord primordium, into vacuolated and sheath cells is controlled by the Notch pathway [16]. Activation of the Notch pathway in the early notochord leads to the generation of more sheath cells at the expense of the vacuolated cells. Conversely, Notch inhibition leads to more vacuolated cells (figure 6a). To manipulate Notch activation specifically in the zebrafish notochord, we generated a new driver line, Tg(*rcn3:QF2*), to drive expression of either constitutively active Notch intracellular domain

(NICD) or a dominant negative form of suppressor of hairless (SuH-DN) from QUAS lines we previously established [21].

When we expressed NICD the number of vacuolated cells was sharply reduced (69%, $n = 4$). This produced a significantly lower λ value and drastically different arrangement of vacuolated cells respect to WT controls, producing a bamboo (1,1,0) pattern throughout most of the notochord, which was readily recognized in centroid plots that collapsed at the centre of the notochord (figure 6c). In three-dimensional renderings, vacuolated cells clearly arranged in a linear arrangement that was completely composed of the bamboo (1,1,0) pattern (figure 6d). Interestingly, the aspect ratio of the notochord rod was also significantly more elliptical in NICD when compared to WT (figure 6e). This is similar to what we observed during morphogenesis (electronic supplementary material, figure S2). We also observed an increase in notochord aspect ratio after a tail cut (electronic supplementary material, figure S3), resulting in a local increase in the formation of staircase and transitional patterns at the expense of the chiral (3,2,1) pattern close to the posterior end of the notochord (proximal to the cut), suggesting that the shape of notochord rod is kept by the internal pressure of the structure and opposed by surrounding tissues.

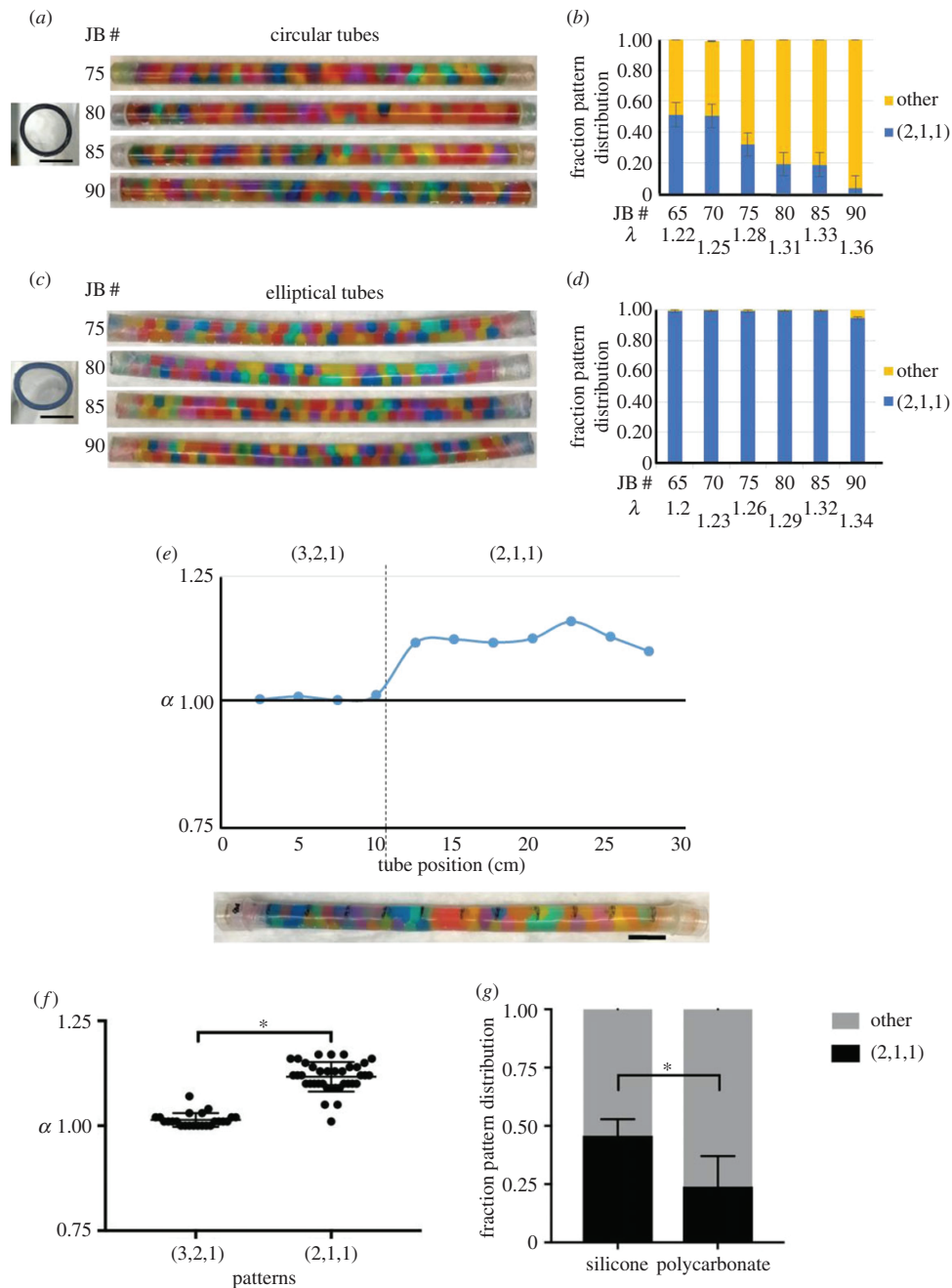


Figure 5. Bead arrangement and tube aspect ratio are interrelated. (a) Cross section of an empty hard polycarbonate circular tube, aspect ratio 1.00 (left). Images of a range of JB#s (75–90) swollen in capped polycarbonate tubes (right). (b) Quantification of the fraction pattern distribution in the polycarbonate tubes shown in (a). The *other* category includes the (3,2,1), (2,2,0) and (4,2,2) patterns. (c) Cross-sectional image of an empty hard vinyl elliptical tube, aspect ratio 1.25 (left). Images of a range of JB#s (75–90) swollen in capped vinyl tubes (right). (d) Quantification of the fraction pattern distribution in the vinyl tubes shown in (c) as in (b). Note that almost all JB#s are arranged in the (2,1,1) staircase pattern. (b,d) λ values differ for equal JB number owing to unequal cross-sectional areas of round polycarbonate and elliptical vinyl tubes. Error bars correspond to s.e. (e) Correlation between the JB pattern and the local aspect ratio (α) measured at 11 points along the length of a silicone tube after 80 JB#s ($\lambda = 1.31$) have swollen. Scale bar, 2.5 cm. (f) Quantitation of α in areas of silicone tubes with the (2,1,1) or (3,2,1) pattern of JB arrangement after 80 JB#s have swollen ($n = 6$ tubes, $*p < 0.0001$, Welch's t -test). Note the deformation into a more elliptical shape associated with the (2,1,1) pattern. Scale bars, 1 mm for circular and elliptical tube cross sections. (g) Staircase (2,1,1) pattern fraction in silicone versus polycarbonate tubes at ($\lambda = 1.33$). Unpaired t -test, $*p = 0.011$ ($n = 5$).

By contrast, when we inhibited Notch in the early notochord we generated an average of 25% ($n = 5$) more vacuolated cells of smaller size, with λ values raising with

respect to WT controls to about 1.60 (figure 6b). The increased λ value was accompanied by a change in vacuolated cell arrangement as visualized by three-dimensional renderings

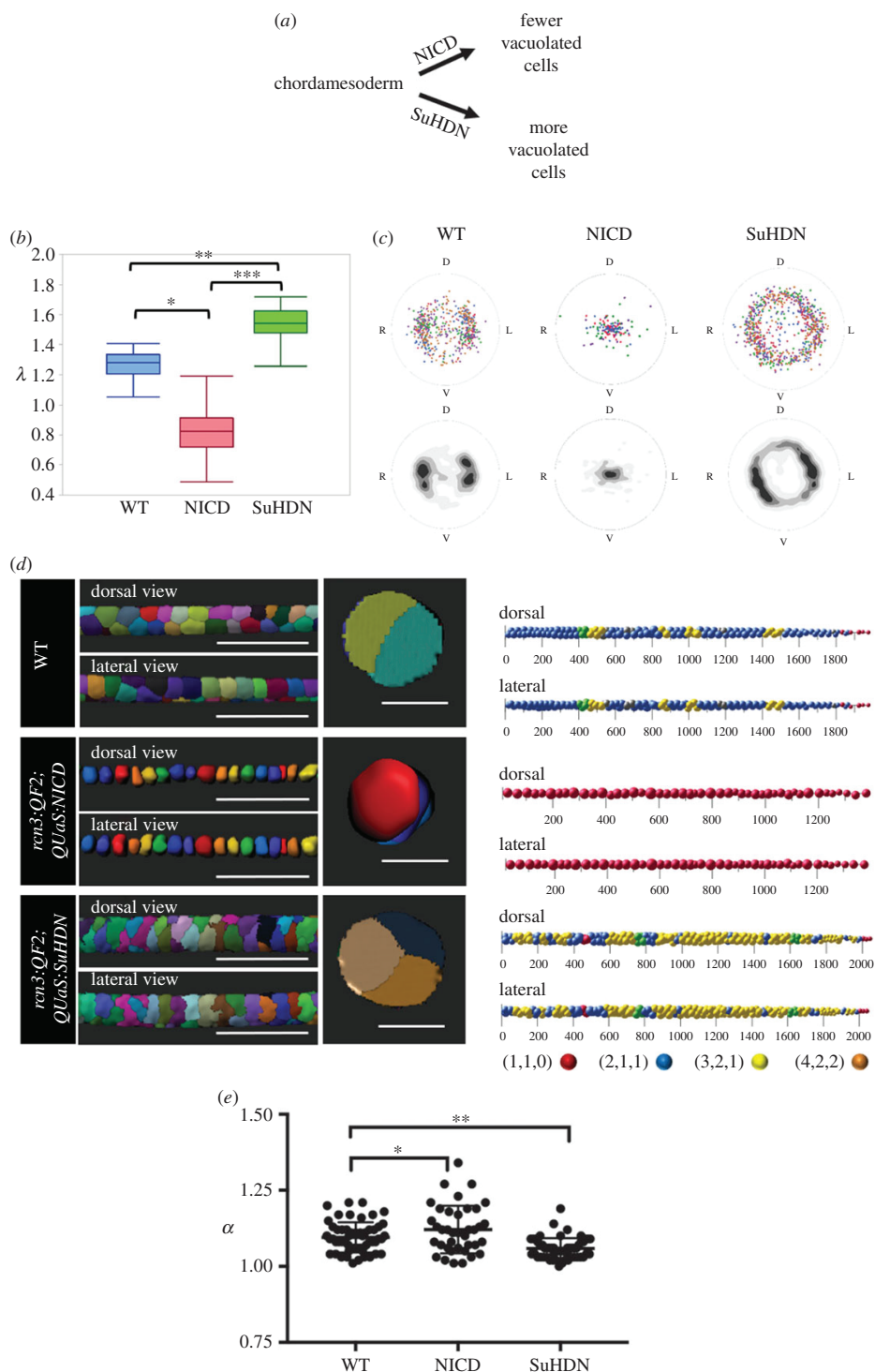


Figure 6. Vacuolated cell density determines their arrangement in the zebrafish notochord. (a) Schematic showing the effect of expressing NICD or SuH-DN in the early notochord (chordamesoderm). (b) Average λ values obtained from three-dimensional reconstructions of notochords in 48hpf WT, NICD and SuHDN embryos ($n = 4$, $p < 0.0001$, one-way ANOVA). (c) Centroid plots and heat maps of vacuolated cells from 48hpf WT (left), NICD (middle) and SuHDN (right) ($n = 4$). Orientation labels D (dorsal), V (ventral), L (left) and R (right). (d) Left panel, three-dimensional renderings of vacuolated cells showing dorsal, lateral and orthogonal (right panels) views of an approximate 500 μm segment of notochord from 48hpf WT (top), NICD (middle) and SuHDN (bottom) zebrafish. Right panel, Sphere plots of notochord vacuolated cells of the 48hpf WT (top), NICD (middle) and SuHDN (bottom) zebrafish embryos shown in (b). Patterns of vacuolated cell arrangement are colour coded as follows: blue (2,1,1), yellow (3,2,1), red (1,1,0), orange (4,2,2), green (transition between 2,1,1 and 3,2,1) and grey (uncertain). (e) Aspect ratio (α) of 500 μm regions, same as in (d), of the notochord rod in 48hpf WT ($n = 5$), NICD ($n = 4$) and SuHDN ($n = 5$) embryos ($*p = 0.043$, $**p = 0.001$, Dunnett's multiple comparisons test). Scale bars are 200 μm for three-dimensional rendering lateral and dorsal views and 50 μm for cross-sectional views.

and centroid plots, which showed a fairly even distribution around the whole periphery of the notochord (figure 6c,d). Remarkably, and similar to our physical models (figure 5), the dramatic shift towards the (3,2,1) chiral pattern was also associated with a significant increase in circularity (reduced aspect ratio) in comparison to WT controls (figure 6f). Together, these data demonstrate that vacuolated cell arrangement in the zebrafish notochord is determined by cell density, which in turn defines λ . Our data also reveal that the local aspect ratio of the rod and the arrangement of vacuolated cells are interdependent.

Next, we wanted to examine a regeneration response that also alters the number and size of notochord vacuolated cells. Recently, we and others showed that in *cavin1b* mutants lacking functional caveolae, vacuolated cells collapse in specific areas under the mechanical stress of locomotion [24,39]. Then, sheath cells invade the inner notochord and trans-differentiate into new vacuolated cells [24]. If the extent of the lesion is large many sheath cells invade, eventually generating more, but smaller, new vacuolated cells [24]. To determine whether the arrangement of vacuolated cells changes during this injury and regeneration response, we placed WT and *cavin1b* mutant embryos in methylcellulose to increase the incidence of large notochord lesions and tracked fish over time during the regeneration response. Interestingly, we found that upon collapse of several vacuolated cells, the remaining nearby vacuolated cells occupied part of the vacant space and adopted locally a bamboo (1,1,0) arrangement (electronic supplementary material, figure S4). Then, over the course of 7 days the invading sheath cells trans-differentiated and expanded to fill the available space. However, these newly generated vacuolated cells were more numerous and smaller compared with the primary vacuolated cells (larger local λ) and were arranged in a complex pattern (electronic supplementary material, figure S4c) similar to that found for fish expressing SuH-DN in the notochord (figure 6d). These data reveal that the arrangement of vacuolated cells is not fixed and is able to re-settle according to the prevailing tissue constraints during injury and regeneration.

4. Discussion

Altogether, our data show that the organization of vacuolated cells within the zebrafish notochord follows packing rules that can be recapitulated in a simple physical model. This model is also able to recapitulate the path vacuolated cells follow as they settle into their final arrangement within the zebrafish notochord. Thus, the morphogenesis of the zebrafish notochord can be considered a self-organizing process [1] in which the osmotic swelling of vacuolated cells, an energy consuming process [13], within the boundaries of a semi-flexible notochord sheath leads to a stereotypical arrangement.

Using water swelling JBs to emulate notochord vacuolated cells provided two important advantages over cylindrical foams and hard sphere packing models. First, the JBs settle into their position as they swell and thus are not influenced by a pre-existing pattern as is the case with cylindrical foams and hard spheres. Second, because the volume JBs reach is variable, within the range covered by our experiments, it is easy to change λ continuously simply by changing bead number for any given length of tube,

which can also be of variable geometry. If we add to these features the possibility of replacing JBs by highly customizable hydrogels, it would be possible to address the effect of the material properties of the packing beads. This may allow for easier physical modelling of soft spheres and other related problems. However, further development of the theoretical framework will be needed to incorporate variables of biological relevance such as tube wall elasticity and geometry, medium viscosity, bead properties (i.e. soft spheres) and combinations of these variables.

Our data demonstrate that the particular arrangement vacuolated cells achieve and the aspect ratio of the notochord rod are largely determined by cell density (figure 6), which defines λ . Therefore, it is basically a geometry-driven process. With a notochord rod aspect ratio that is initially highly elliptical (electronic supplementary material, figure S2), probably because of the effect of surrounding tissues, vacuolated cells are prone to arrange in a staircase pattern. However, osmotic swelling of the vacuolated cells tends to counter this effect, making the structure more circular. This effect is also patent in the mirroring changes that α and λ exhibit along the length of the notochord, i.e. as λ increases α diminishes (electronic supplementary material, figure S5), suggesting a mechanical buffering mechanism. The final α value the notochord eventually reaches (approx. 1.07) is at the boundary where the staircase pattern is strongly favoured in hard sphere-simulations, but close to what allows chiral patterns to exist, thus explaining the bias in vacuolated cell arrangement observed in the notochord with respect to what is seen in circular tubes, as well as the presence of chiral patterns which are basically not found in hard elliptical tubes. However, establishing exact boundary points is challenging because the λ values for vacuolated cells are low estimates that do not take into account the role cell shapes irregularities (e.g. $\lambda < 1$ for NICD in figure 6). Conversely, it is also expected that a soft sphere theoretical model would be closer quantitatively to the JB and *in vivo* models with a lower effective λ value. Nevertheless, the trends and responses to variations in tube geometry are all in good agreement.

One way to establish a closer quantitative comparison between the hard sphere models and the notochord vacuolated cell is to obtain effective λ values using the longitudinal centroid plots by calculating each cell's diameter as twice the distance from the perimeter to the centroid. This approximation is valid for the notochord because all vacuolated cells are in contact the surrounding sheath. Using this method, we obtained average $\lambda \approx 1.85$ for WT, which is close the boundary where helical patterns are generated for a hard tube with an $\lambda \sim 1.866$ in simulations.

Clearly, the material properties of the sheath and the mechanical coupling of surrounding tissues [40] also influence the local aspect ratio (α) of the notochord rod, thereby modulating the local arrangement of vacuolated cells. In this context, the initial allocation of vacuolated cells and the starting morphology of the notochord rod, which are defined during gastrulation [41], probably determine the internal organization of the notochord. These notions may also help explain the variability in size and arrangement that are seen across vertebrates. For example, the large notochord rod of *Xenopus laevis* is filled with more vacuolated cells, but of roughly the same size compared with zebrafish. As a result, their organization is more complex, with internal cells that are not in contact with the sheath, yet still similar to that

achieved by silicone/JB tubes of similar proportions (electronic supplementary material, figure S6). It will be interesting to explore whether the mammalian notochord also follows the same organizational principles.

During morphogenesis, vacuolated cells are able to slide past each other as they settle into their final arrangement (figure 1), which later (around 96 hpf) is stabilized by the formation of desmosomes between vacuolated cells [24,42]. However, this arrangement is not fixed, as illustrated by the dynamic changes that occur following vacuolated cell collapse and regeneration (electronic supplementary material, figure S2). This provides a robust mechanism ensuring the mechanical integrity of the axis and safeguarding normal spine development when more vacuolated cells are generated [24]. However, it remains unclear whether the production of more but smaller vacuolated cells impacts the mechanical properties of the spine, particularly the intervertebral discs, later in life. By contrast, when fewer vacuolated cells are produced (e.g. NICD expression) the axis kinks during spine formation [13], suggesting that the allocation of a minimum number of vacuolated cells during embryogenesis is crucial.

Ethics. Experiments were performed at Duke University. Research using zebrafish was conducted adhering to protocols approved by the Duke University Institutional Animal Care Use Committee.

Data accessibility. The datasets supporting this article have been uploaded as part of the electronic supplementary material. Original scripts used for data analysis and the data have been archived; they can be accessed at our website <https://sites.duke.edu/bagnat/tools/>.

Authors' contributions. M.B. designed the study; J.N., J.B., V.S. and J.G. performed experiments with physical and *in vivo* models; J.N., J.G. and M.B. interpreted experimental data; E.L.S. and S.R.L. developed quantitative methods and analysed data; Y.H. and P.C. developed the theory and performed the numerical simulations for hard spheres; M.B. wrote the manuscript with input from the other authors.

Competing interests. We declare we have no competing interests.

Funding. This work was supported by National Institutes of Health (NIH) grant no. AR065439 and a Howard Hughes Medical Institute Faculty Research Scholar grant to M.B.; by Simons Foundation grant no. 524764 to S.R.L.; J.G. was supported by NIH fellowship F31GM122422. P.C. and Y.H. were supported by National Science Foundation grant no. DMR-1749374. Our light sheet microscopy was supported by NIH Shared Instrumentation grant no. 1S10OD020010-01A1.

Acknowledgements. We thank Deniz Ertaş for useful suggestions about modelling, Nanette Nascone-Yoder for proving *Xenopus* tadpoles, and Brenton Hoffman, Stefano Di Talia, Deniz Ertaş and the Bagnat laboratory for critically reading the manuscript.

References

- Karsenti E. 2008 Self-organization in cell biology: a brief history. *Nat. Rev. Mol. Cell Biol.* **9**, 255–262. (doi:10.1038/nrm2357)
- Turing AM. 1990 The chemical basis of morphogenesis. *Bull. Math. Biol.* **52**, 153–197; discussion 19–52. (doi:10.1007/BF02459572)
- Kauffman SA. 1981 Pattern formation in the *Drosophila* embryo. *Phil. Trans. R. Soc. Lond. B* **295**, 567–594. (doi:10.1098/rstb.1981.0161)
- Pate E. 1984 The organizer region and pattern regulation in amphibian embryos. *J. Theor. Biol.* **111**, 387–396. (doi:10.1016/S0022-5193(84)80217-9)
- Muller P, Rogers KW, Jordan BM, Lee JS, Robson D, Ramanathan S, Schier AF. 2012 Differential diffusivity of Nodal and Lefty underlies a reaction-diffusion patterning system. *Science* **336**, 721–724. (doi:10.1126/science.1221920)
- Jacobo A, Hudspeth AJ. 2014 Reaction-diffusion model of hair-bundle morphogenesis. *Proc. Natl Acad. Sci. USA* **111**, 15 444–15 449. (doi:10.1073/pnas.1417420111)
- Manukyan L, Montandon SA, Fofonjka A, Smirnov S, Milinkovitch MC. 2017 A living mesoscopic cellular automaton made of skin scales. *Nature* **544**, 173–179. (doi:10.1038/nature22031)
- Tewary M, Ostblom J, Prochazka L, Zulueta-Coarasa T, Shakiba N, Fernandez-Gonzalez R, Zandstra Peter W. 2017 A stepwise model of reaction-diffusion and positional information governs self-organized human peri-gastrulation-like patterning. *Development* **144**, 4298–4312. (doi:10.1242/dev.149658)
- Hiscock TW, Megason SG. 2015 Mathematically guided approaches to distinguish models of periodic patterning. *Development* **142**, 409–419. (doi:10.1242/dev.107441)
- Thompson DAW. 1917 *On growth and form*, 793 pp. Cambridge, UK: Cambridge University Press.
- Varner VD, Gleghorn JP, Miller E, Radisky DC, Nelson CM. 2015 Mechanically patterning the embryonic airway epithelium. *Proc. Natl Acad. Sci. USA* **112**, 9230–9235. (doi:10.1073/pnas.1504102112)
- Shyer AE, Tallinen T, Nerurkar NL, Wei Z, Gil ES, Kaplan DL, Tabin CJ, Mahadevan L. 2013 Villification: how the gut gets its villi. *Science* **342**, 212–218. (doi:10.1126/science.1238842)
- Ellis K, Bagwell J, Bagnat M. 2013 Notochord vacuoles are lysosome-related organelles that function in axis and spine morphogenesis. *J. Cell Biol.* **200**, 667–679. (doi:10.1083/jcb.201212095)
- Stemple DL. 2005 Structure and function of the notochord: an essential organ for chordate development. *Development* **132**, 2503–2512. (doi:10.1242/dev.01812)
- Ellis K, Hoffman BD, Bagnat M. 2013 The vacuole within: how cellular organization dictates notochord function. *Bioarchitecture* **3**, 64–68. (doi:10.4161/bioa.25503)
- Yamamoto M *et al.* 2010 Mib-Jag1-Notch signalling regulates patterning and structural roles of the notochord by controlling cell-fate decisions. *Development* **137**, 2527–2537. (doi:10.1242/dev.051011)
- Adams DS, Keller R, Koehl MA. 1990 The mechanics of notochord elongation, straightening and stiffening in the embryo of *Xenopus laevis*. *Development* **110**, 115–130.
- Parsons MJ *et al.* 2002 Zebrafish mutants identify an essential role for laminins in notochord formation. *Development* **129**, 3137–3146.
- Gray RS, Wilm TP, Smith J, Bagnat M, Dale RM, Topczewski J, Johnson SL, Solnica-Krezel L. 2014 Loss of col8a1a function during zebrafish embryogenesis results in congenital vertebral malformations. *Dev. Biol.* **386**, 72–85. (doi:10.1016/j.ydbio.2013.11.028)
- Corallo D, Schiavinato A, Trapani V, Moro E, Argenton F, Bonaldo P. 2013 Emilin3 is required for notochord sheath integrity and interacts with Scube2 to regulate notochord-derived Hedgehog signals. *Development* **140**, 4594–4601. (doi:10.1242/dev.094078)
- Wopat S *et al.* 2018 Spine patterning is guided by segmentation of the notochord sheath. *Cell Rep.* **22**, 2026–2038. (doi:10.1016/j.celrep.2018.01.084)
- Lleras Forero L *et al.* 2018 Segmentation of the zebrafish axial skeleton relies on notochord sheath cells and not on the segmentation clock. *eLife* **7**, e33843. (doi:10.7554/eLife.33843)
- Pogoda HM, Riedl-Quinkertz I, Lohr H, Waxman JS, Dale RM, Topczewski J, Schulte-Merker S, Hammerschmidt M. 2018 Direct activation of chordoblasts by retinoic acid is required for segmented centra mineralization during zebrafish spine development. *Development* **145**, dev159418. (doi:10.1242/dev.159418)
- Garcia J *et al.* 2017 Sheath cell invasion and trans-differentiation repair mechanical damage caused by loss of caveolae in the zebrafish notochord. *Curr. Biol.* **27**, 1982–1989.e3. (doi:10.1016/j.cub.2017.05.035)
- Lopez-Baez JC *et al.* 2018 *Wilms Tumor 1b* defines a wound-specific sheath cell subpopulation associated with notochord repair. *eLife* **7**, e30657. (doi:10.7554/eLife.30657)
- Westerfield M. 2000 *The zebrafish book. A guide for the laboratory use of zebrafish (Danio rerio)*. Eugene, OR: University of Oregon Press.

27. Kawakami K. 2004 Transgenesis and gene trap methods in zebrafish by using the Tol2 transposable element. *Methods Cell Biol.* **77**, 201–222. (doi:10.1016/S0091-679X(04)77011-9)
28. Ghosh A, Halpern ME. 2016 Transcriptional regulation using the Q system in transgenic zebrafish. *Methods Cell Biol.* **135**, 205–218. (doi:10.1016/bs.mcb.2016.05.001)
29. Mughal A, Chan H, Weaire D, Hutzler S. 2012 Dense packings of spheres in cylinders: simulations. *Phys. Rev. E* **85**, 051305. (doi:10.1103/PhysRevE.85.051305)
30. Fu L, Steinhardt W, Zhao H, Socolar JE, Charbonneau P. 2016 Hard sphere packings within cylinders. *Soft Matter* **12**, 2505–2514. (doi:10.1039/C5SM02875B)
31. Atkinson S. 2017 Implementation of the Torquato-Jiao Sequential Linear Programming Algorithm. [Internet] [cited viewed Apr. 2017]. (<https://github.com/sdatkinson/TJ>)
32. Torquato S, Jiao Y. 2010 Robust algorithm to generate a diverse class of dense disordered and ordered sphere packings via linear programming. *Physical Review E* **82**, 061302. (doi:10.1103/PhysRevE.82.061302)
33. Weaire D, Hutzler S, Pittet N. 1992 Cylindrical packings of foam cells. *Forma* **7**, 259–263.
34. Pittet N, Rivier N, Weaire D. 1995 Cylindrical packing of foam cells. *Forma* **10**, 65–73.
35. Mughal A, Chan HK, Weaire D. 2011 Phyllotactic description of hard sphere packing in cylindrical channels. *Phys. Rev. Lett.* **106**, 115704. (doi:10.1103/PhysRevLett.106.115704)
36. Pittet N, Boltzenhagen P, Rivier N, Weaire D. 1996 Structural transitions in ordered, cylindrical foams. *Europhys. Lett.* **35**, 7. (doi:10.1209/epl/1996-00102-1)
37. Hutzler S, Weaire D, Crawford R. 1997 Moving boundaries in ordered cylindrical foam structures. *Philos. Mag. B* **75**, 845–857. (doi:10.1080/13642819708205711)
38. Winkelmann J, Haffner B, Weaire D, Mughal A, Hutzler S. 2017 Simulation and observation of line-slip structures in columnar structures of soft spheres. *Phys. Rev. E* **96**, 012610. (doi:10.1103/PhysRevE.96.012610)
39. Lim YW *et al.* 2017 Caveolae protect notochord cells against catastrophic mechanical failure during development. *Curr. Biol.* **27**, 1968. (doi:10.1016/j.cub.2017.05.067)
40. Williams MLK, Sawada A, Budine T, Yin C, Gontarz P, Solnica-Krezel L. 2018 Gon4 I regulates notochord boundary formation and cell polarity underlying axis extension by repressing adhesion genes. *Nat. Commun.* **9**, 1319. (doi:10.1038/s41467-018-03715-w)
41. Glickman NS, Kimmel CB, Jones MA, Adams RJ. 2003 Shaping the zebrafish notochord. *Development* **130**, 873–887. (doi:10.1242/dev.00314)
42. Nixon SJ *et al.* 2007 Caveolin-1 is required for lateral line neuromast and notochord development. *J. Cell Sci.* **120**, 2151–2161. (doi:10.1242/jcs.003830)